UNIVERSITAT ROVIRA I VIRGILI

HEXAALUIMINATE-TYPE CATALYSTS FOR N2O ABATEMENT

Marta Santiago Redondo

ISBN: 978-84-693-8864-8
Dipòsit Legal: T.1943-2010

UNIVERSITAT ROVIRA I VIRGILI
HEXAALUIMINATE-TYPE CATALYSTS FOR N2O ABATEMENT
Marta Santiago Redondo
ISBN:978-84-693-8864-8/DL:T.1943-2010

UNIVERSITAT ROVIRA I VIRGILI
HEXAALUIMINATE-TYPE CATALYSTS FOR N2O ABATEMENT
Marta Santiago Redondo
ISBN:978-84-693-8864-8/DL:T.1943-2010

UNIVERSITAT ROVIRA I VIRGILI
HEXAALUIMINATE-TYPE CATALYSTS FOR N2O ABATEMENT
Marta Santiago Redondo
ISBN:978-84-693-8864-8/DL:T.1943-2010

DOCTORAL THESIS

HEXAALUMINATE-TYPE CATALYSTS FOR N_2O ABATEMENT

MARTA SANTIAGO REDONDO

SUPERVISED BY
PROF. DR. JAVIER PÉREZ-RAMÍREZ

ICIQ-URV

TARRAGONA
2010

UNIVERSITAT ROVIRA I VIRGILI
HEXAALUIMINATE-TYPE CATALYSTS FOR N2O ABATEMENT
Marta Santiago Redondo
ISBN:978-84-693-8864-8/DL:T.1943-2010

UNIVERSITAT ROVIRA I VIRGILI
HEXAALUIMINATE-TYPE CATALYSTS FOR N2O ABATEMENT
Marta Santiago Redondo
ISBN:978-84-693-8864-8/DL:T.1943-2010

Javier Pérez-Ramírez, Full Professor and Chair of Catalysis Engineering at the Institute for Chemical and Bioengineering, ETH Zürich, Switzerland.

CERTIFIES:

That the present research study, entitled 'Hexaaluminate-type catalysts for N_2O decomposition', presented by **Marta Santiago Redondo** for the award of the degree of Doctor, has been carried out under my supervision at The Institute of Chemical Research of Catalonia (ICIQ), Tarragona, Spain.

Zürich, September 2010

Prof. Dr. Javier Pérez-Ramírez

ICIQ
Institut Català d'Investigació Química

UNIVERSITAT ROVIRA I VIRGILI

UNIVERSITAT ROVIRA I VIRGILI
HEXAALUIMINATE-TYPE CATALYSTS FOR N2O ABATEMENT
Marta Santiago Redondo
ISBN:978-84-693-8864-8/DL:T.1943-2010

UNIVERSITAT ROVIRA I VIRGILI
HEXAALUIMINATE-TYPE CATALYSTS FOR N2O ABATEMENT
Marta Santiago Redondo
ISBN:978-84-693-8864-8/DL:T.1943-2010

Acknowledgments

En primer lugar, me gustaría agradecer a mi supervisor el Prof. Dr. Javier Pérez-Ramírez la oportunidad que me ha brindado al permitirme compaginar mi trabajo en el ICIQ con la elaboración de esta tesis y al tiempo dedicado para que yo creciera científicamente. También, por la confianza demostrada al contar conmigo para tu nuevo proyecto en el ETH en Zürich.

A cada uno de los miembros del tribunal por aceptar formar parte del mismo.

Al director de l'Institut Català d'Investigació Química, Prof. Dr. Miquel Pericàs per deixar-me fer la defensa de la meva tesi fins la que fa poc era també casa meva and also to Prof. Dr. Evgenii Kondratenko and Dr. Johan Groen for all the nice collaborations we had during the last years.

Durante estos años en la URV y en el ICIQ, he conocido muchas personas que me han ayudado en el día a día muchísimo y a las que no quisiera dejar de agradecer: En especial a Anton, Esther, Eduardo, Simona, Enrique, Susana (Merci chic@s! por hacerme la vida más fácil!) Al los chicos de compras, a los informáticos, mantenimiento, a Maria y su bon día y a las "secres", en especial a Beatriz porque siempre está dispuesta a hacer lo que le pidas con una sonrisa! Y eso no tiene precio!

També a Mercé Moncusí i a la Rita de microscopia, sempre ajudant-me a fer aquestes fotos tant maques!

A todos los compañer@s y amig@s que he tenido en el laboratorio de los heterogéneos en todos estos años; chic@s hemos sido una gran familia!

A Sònia y Yolandita! Por ser además de grandes compañeras, grandes amigas!!! Gracias por todas las risas, conversaciones, confidencias y por estar ahí siempre apoyando, ya sabéis que os valoro mucho tanto científicamente como personalmente! Mucha suerte! A Miguel, el asturiano serio del piso de abajo! Gracias por tu ayuda y tus consejos! Tú sí que eres un FIERA!

A Georgiana por haber compartido después de Tarragona conmigo los primeros meses en Zurich, por tu amistad, por tu ayuda en el día a día y por no dejarme sin mi rosa de San Jordi. No lo voy a olvidar!

Blaise, Ceci, Maria, Sharon, Amol and Danny.: Thanks for the good moments!

UNIVERSITAT ROVIRA I VIRGILI
HEXAALUIMINATE-TYPE CATALYSTS FOR N2O ABATEMENT
Marta Santiago Redondo
ISBN:978-84-693-8864-8/DL:T.1943-2010

A mis amigos de siempre y para siempre: Esther, tet no sabes cómo te echo de menos bandarra! Eva, Meritxell, Raquel, Jorgina, Nuria y Xavi. Chic@s sois estupendos!

Por último sólo dedicar mi tesis a mi familia entera, a los que están y a los que ya se fueron… en especial a mis padres, a mi hermano, a chimo y a ti porque tú me completas.

The Spanish MICINN (CTQ2006-01562/PPQ, AP2005-5147, and Consolider-Ingenio 2010, grant CSD2006-0003) and the ICIQ Foundation are acknowledged for the financial support of this research.

Marta Santiago

Zürich, September 2010

UNIVERSITAT ROVIRA I VIRGILI
HEXAALUIMINATE-TYPE CATALYSTS FOR N2O ABATEMENT
Marta Santiago Redondo
ISBN:978-84-693-8864-8/DL:T.1943-2010

Contents

UNIVERSITAT ROVIRA I VIRGILI
HEXAALUIMINATE-TYPE CATALYSTS FOR N2O ABATEMENT
Marta Santiago Redondo
ISBN:978-84-693-8864-8/DL:T.1943-2010

UNIVERSITAT ROVIRA I VIRGILI
HEXAALUIMINATE-TYPE CATALYSTS FOR N2O ABATEMENT
Marta Santiago Redondo
ISBN:978-84-693-8864-8/DL:T.1943-2010

Chapter 1

Introduction

A brief introduction of the state-of-the-art N_2O abatement in the chemical industry is presented. The chemical industry and energy processes represent 39% of all the anthropogenic nitrous oxide emissions and only emissions from these sources can be reduced in the short term. Catalytic decomposition is the most widely used N_2O abatement method. Several catalysts based on bulk, supported and unsupported metals, pure and mixed oxides, and metal-loaded zeolites have been studied, however, only a few of them showed reasonable performance under realistic conditions. The research described in this thesis focuses on the development of a new family of catalysts based on metal-substituted hexaaluminates, showing excellent qualities for high-temperature N_2O abatement under simulated conditions. This chapter describes the objectives and structure of this doctoral work.

UNIVERSITAT ROVIRA I VIRGILI
HEXAALUIMINATE-TYPE CATALYSTS FOR N2O ABATEMENT
Marta Santiago Redondo
ISBN:978-84-693-8864-8/DL:T.1943-2010

1. Nitrous oxide

Nitrous oxide (N_2O), often referred to as laughing gas, is recognized as a harmful gas causing adverse effects on our environment. In recent decades, atmospheric concentration of this gas has been increasing at roughly 0.25% per year [1], and unfortunately it appears that this trend will not be changed easily. Scientists (and politicians) widely accept that N_2O contributes to the enhanced greenhouse effect, a natural phenomenon caused by absorption of infrared radiation in the atmosphere reflected from the surface of the earth [2]. Figure 1 shows the distribution of global anthropogenic greenhouse gas emissions in 2004.

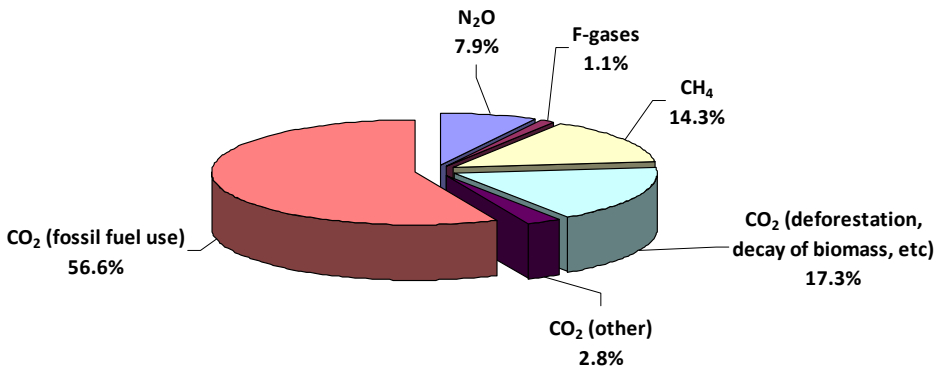

Figure 1. Share of different anthropogenic greenhouse gases in total global emissions in 2004. Source: IPCC 4th Assessment Report: Climate Change 2007: Synthesis Report.

Although nitrous oxide does not seem to be a major contributor to global warming (7.9%) [3], its presence in the atmosphere is much more dangerous and worrying than the other two common anthropogenic greenhouse gases, CO_2 and CH_4. Primarily, because of its higher Global Warming Potential (GWP) (310 and 21 times more potent than CO_2 and CH_4, respectively) and atmospheric lifetime of 150 years; and additionally for being the single most important ozone-depleting emission agent during 21st century [4].

Atmospheric N_2O emissions are produced by both natural and anthropogenic sources. About 70% is emitted by bacterial breakdown of nitrogen in soils and oceans while the remaining 30% is due to the human activities [1]. Within the anthropogenic

sources, agricultural practices and activities contributes to 61%, chemical industry represents 29%, and combustion, including human sewage and burning of biomass and biofuels, the residual 10%. Since control of N_2O emissions from agriculture is difficult to assess, only emissions from chemical industry and energy processes can be reduced in the short term [5].

2. Overview of present technologies

N_2O abatement strategies differ depending on the stringency of emission regulations, and on the complexity of developing an effective technology for each process. One of the most suitable methodologies is the catalytic decomposition where a solid surface facilitates the cleavage of the N-O bond in the nitrous oxide molecule leading to harmless N_2 and O_2. However, several aspects should be taken into account when designing de-N_2O catalysts *i.e.* the N_2O content, location in the plant, temperature, gas flow, pressure and feed composition. NO_x, O_2, SO_2, and H_2O are commonly present in waste streams in addition to nitrous oxide, acting typically as inhibitors or poisons, thus reducing the activity of catalysts or suppressing it completely. Unfortunately, a one-solution-fits-all does not exist, and the catalytic system has to be optimized to the specific source and emission point in which the abatement is practised [5]. A number of catalysts based on bulk, supported and un-supported metals, pure and mixed oxides, and metal-loaded zeolites have been reported in the literature [6]. Nevertheless, almost all studies have been typically performed under unrealistic conditions limiting the practical design of a catalyst for a real source. Reducing the gap between laboratory reaction models and real conditions is vital, and therefore the evaluation of catalysts under practically-relevant conditions becomes necessary.

In chemical industry, the two most significant sources of nitrous oxide emissions are nitric acid (NA) and adipic acid (AA) production. Global nitrous oxide emissions from these two sources accounted for more than 154 million metric tons of carbon dioxide (CO_2) equivalent (1 kg N_2O = 310 kg CO_2-eq) (Figure 2) in year 2000. It is estimated that the global nitrous oxide emissions from these sources are expected to grow approximately 13% between 2005 and 2020 [7].

UNIVERSITAT ROVIRA I VIRGILI
HEXAALUIMINATE-TYPE CATALYSTS FOR N2O ABATEMENT
Marta Santiago Redondo
ISBN:978-84-693-8864-8/DL:T.1943-2010

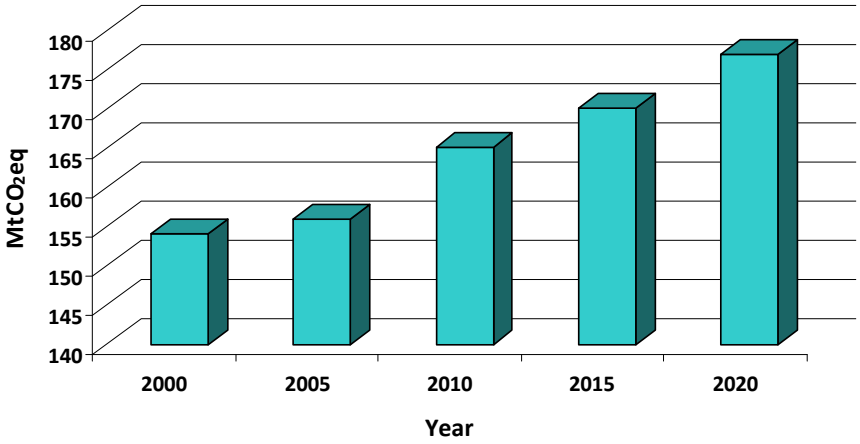

Figure 2. Global nitrous oxide emissions from nitric acid and adipic acid production 2000-2020. Source: EPA: Global Anthropogenic Non-CO_2 Greenhouse Gas Emissions: 1990-2020, June 2006 Revised.

Other sources are associated with chemical processes using nitric acid as oxidizing agent or those involving ammonia oxidation steps (caprolactam, glyoxal) [8,9]. Emissions related with the latter sources are not conveniently quantified and predicting their impact remains complicated. Regarding energy processes, the global N_2O emission from fossil-fuel combustion is estimated at 60-160 Mton CO_2-eq per year [6], without taking uncertain emissions from biomass and waste combustion into account. In the next sections, the state-of-the-art catalytic technologies for N_2O abatement are concisely reviewed.

2.1. Adipic acid production

Adipic acid is mainly used as the precursor in the production of Nylon 6,6 with an annual world production of 2.7 Mton per year. N_2O is generated during the oxidation of cyclohexanol-cyclohexanone mixtures with nitric acid. The most notorious feature of this source is the high content of N_2O 25-40 vol.%, simplifying the problem to finding a catalytic or thermal abatement process, since N_2O decomposition is an exothermal reaction.[5] One common practise for concentrated N_2O streams is to dilute the inlet N_2O stream with air to control the temperature rise in the catalyst bed and to guarantee safe and stable operation.

Adipic acid was the major source of N_2O emissions in the chemical industry until 2003. Major worldwide adipic acid producers organized a consortium targeting the voluntary reduction of N_2O emission either by thermal or catalytic N_2O decomposition which resulted in more than ~90% reduction [10].

The technologies in use so far for N_2O abatement in adipic acid manufacturing are $CuAl_2O_4/Al_2O_3$ and Ag/Al_2O_3 by BASF, $CoO\text{-}NiO/ZrO_2$ by DuPont, and CuO/Al_2O_3 by Asahi Chemical [11]. On the other hand, other attractive strategies to catalytic and thermal methodologies have also been proposed: the integration of adipic acid and nitric acid plants [12,13] implemented in the BASF's adipic acid and nitric acid plants in Ludwigshafen (Germany), and the reutilization of N_2O as a valuable oxidant to oxidize the benzene to phenol developed by Solutia and the Boreskov Institute of catalysis [14]. After the implementation of catalytic systems, limited progress has been achieved. Only Alini *et al*. [15] claimed $AB_{1-x}B'_xO_3$ perovskites with A = La or Ca, B = Mn or Fe, and B' = Cu or Ni as a possible candidate under realistic conditions.

2.2. Glyoxal and glyoxylic acid production

Glyoxylic acid is used as a key intermediate in the Pharma or Agro industries. It is used in the manufacturing of synthetic Vanillin and ethyl Vanillin, in the syntheses of widely used antibiotic, Amoxycillin and as a starting material for the synthesis of iron chelates, a product group used as micronutrient in the Agro industry.

Clariant at Lamotte, France is the only known manufacturer of glyoxal and glyoxilic acid where the production process gives rise to N_2O emissions. The company is also a pioneer in the application of N_2O abatement technology in glyoxal production. Thermal treatment system, promoted by specific catalyst, an ion-exchanged Fe-ferrierite patented by Grande Paroisse [16], is used in the abatement. In this treatment, the N_2O content in the tail gas (85 vol.%) is diluted to *ca.* 10 vol.% by air at the inlet of the process to control exothermally the reaction and allowing safe and stable operation of the catalyst. The adiabatic temperature rise in the reactor, 200 K, is used to preheat the inlet tail-gas up to 675 K. (It is known that N_2O is a very stable gas which requires energy input or the addition of reducing agents for achieving an acceptable

performance target in N_2O mitigation). The system reaches a decomposition rate of over 95% of N_2O when the catalyst is fresh [10].

2.3. Nitric acid production

Nitric acid is a widely produced basic chemical throughout the world. It is a key ingredient in ammonium nitrate fertilizers, nitrate explosives, and various complex acid products. N_2O is formed as a by-product in Ostwald reaction. Due to the different operation conditions, the abatement technology implemented with success in adipic acid plants (~90% emission reduction either by thermal or catalytic N_2O decomposition) cannot be extrapolated to nitric acid production. The relatively low N_2O concentration in nitric acid plants (in the order of 1000 ppm) and the presence of abundant inhibitors (H_2O, NO_x and O_2) made the development of active and stable catalyst systems essential for this application. As reviewed by Pérez-Ramírez *et al.* [5], N_2O abatement at different locations in the nitric acid plant was extensively investigated during the last decade.

As a result of the studies, direct N_2O decomposition below the noble metal gauzes in the ammonia burner (process-gas option) and in the tail-gas train (tail-gas option) were concluded to be cost-effective abatement measures for existing plants, and the major producers of nitric acid started the development of new catalytic systems.

In the process-gas option, the three catalytic systems described in the patent literature and developed by the industry mainly relates to supported spinels and bulk perovskite: CuO/Al_2O_3 by BASF [17], $La_{0.8}Ce_{0.2}CoO_3$ by Johnson Matthey [18], Co_2AlO_4/CeO_2 by Yara International [19]. The major advantage of process-gas decomposition is the universal application in all nitric acid plants.

In the tail-gas, Uhde commercialized EnviNOx process for the combined removal of N_2O and NO_X in a single fixed-bed reactor by use of iron-containing zeolites. However, this option is limited in plants with tail-gas temperature >700 K, since the use of Fe-zeolites at lower temperatures is prohibitive without the presence of reducing agents and gas preheating.[5,20].

Several catalytic systems have been studied in the last decade for being an alternative option to the methodologies already commercialized. A considerable

number of papers and patents claiming higher activity for N_2O decomposition were published but these systems failed to be considered as serious alternatives due to the 'ideal' conditions taken into consideration during the studies.

In the process-gas, very recent studies investigating $ABAl_{11}O_{19}$ hexaaluminates with A = Ba or La and B = Fe, Mn, Co, or Ni [21], α-alumina-supported iron oxide [22], and mayenite [23] can be found. In the tail-gas, only extra-framework Fe-ZSM-5 [24-26] showed remarkable activity and stability in simulated tail-gas mixtures.

2.4. Caprolactam production

Caprolactam is an intermediate primarily used in the production of Nylon 6 fibers and resins. The principal routes for the production of caprolactam are HPO (hydroxylamine phosphate oxime) and HSO (hydroxylamine sulfate oxime) where N_2O is formed as a by-product at different points of the process.

Until now, the uncertainty in annual N_2O emissions from caprolactam production has been estimated at about 70% and reduction measures are not available yet [10]. There are many open questions regarding the characteristic of the process and the dependence of process variant. Besides, the existence of multi-point emissions of N_2O makes the situation still more complex. However, some advances have been done, since in 2008, Ube Industries Ltd and Mitsubishi Corp have been jointly developing a process to reduce N_2O in Thailand (Thai Caprolactam). This is the world's first Clean Development Mechanism (CDM) project to reduce N_2O from caprolactam production. The catalyst used is a palladium on $AlSiO_2$-MgO. The catalyst will be implemented in the tail-gas operating at 823 K and it is expected to recover 90% of N_2O [27].

The Netherlands is making several efforts on making the producers aware of the emission data that need to be reported and studied to see if the existing N_2O abatement technologies can be applied to the caprolactam plants. However and despite of all these developments more information from other countries is required and more research regarding new technologies is needed.

2.5. Stationary combustion

Fluidized-bed combustion (FBC) is a combustion technology with an increasing presence in many countries due to its advantages. Its versatility in the use of fossils such as biomass, wastes, sludge and coals as well as its proven friendly environmental technology concerning SO_2 and NO_x emissions. FBCs feature a relatively low combustion temperature, leading to lower emission levels of NO_x and optimal conditions for sulphur capture. However, these merits are offset as the window operation temperature of the process (1023–1173 K) is typically in the range where N_2O formation is notable; up to 600 ppm depending on the combustion temperature and fuel used. The most important pathways that lead to N_2O are the homogeneous oxidation of N-groups in volatiles (mainly HCN) and heterogeneous reactions (direct oxidation of char-N and the reaction of char-N with NO) [28].

With the future requirements of more stringent GHG reductions after the first Kyoto protocol period of the United Nations Framework Convention on Climate Change (UNFCC, 1998), and the exponentially increase in energy demand due to the electrification of developing countries and the growing utilization of various-grade biofuels and waste, it can be expected that the use of FBC will continue increasing and even dominates N_2O emissions levels in stationary combustion sources [29].

Practical applications could be achieved by placing the catalysts in different positions in the FBC system differing on the temperature range. However, the critical point of this source for finding a suitable technology is the presence of SO_2 and H_2O two pollutants which usually are acting as poisons and/or severe inhibitors for many catalytic systems. Until now, only few studies have shown ZSM5 containing iron as promising candidate for N_2O decomposition in stationary combustion due to the promoting effect of these pollutants over its catalytic performance that also can be improved by the addition of reduction agents as propane [30-32]. However, contrarily to the chemical industry non counter-measures have been implemented thus far.

3. Aim of the thesis

Over the last decades, a large number of catalysts have been studied for catalytic decomposition of N_2O [6]. Most of these catalysts failed to be an alternative option for

already commercialized counterparts and few of them showed reasonable activities under realistic conditions. Metal-substituted hexaaluminates, β-aluminas, thus far applied mainly in the catalytic combustion of methane in gas-turbine applications [33], show excellent qualities as promising candidates for high-temperature N_2O abatement. Their layered structure together with the presence of redox sites provides chemical stability, high-resistant to thermal shock and activity in order to achieve high N_2O conversions.

This thesis focuses on the development of metal-substituted hexaaluminates, a novel catalytic system for high-temperature N_2O abatement. Synthesis, *in situ* thermal activation and characterization of metal-substituted hexaaluminates have been carried out with the aim of gaining a better understanding of their formation. The catalytic activity was also evaluated simulating realistic conditions in both processes, *i.e.* nitric acid plant and stationary combustion. Additionally, an alternative route of synthesis, using templating approaches for the first time, has been successfully developed improving its catalytic activity. Finally, transient studies in the Temporal Analysis of Products (TAP) reactor have been carried out over one of the most active metal-substituted hexaaluminate in order to gain insights into the N_2O decomposition mechanism into N_2 and O_2.

4. Outline of the thesis

An overview of nitrous oxide emissions from an environmental standpoint, its sources, abatement strategies in chemical industries, and a review of scientific studies dealing with catalytic decomposition of nitrous oxide are discussed in **Chapter 1**.

Chapter 2 focuses on the synthesis and characterization studies during thermal activation of dawsonite-type compounds to oxide catalysts. A combination of techniques (HT-XRD, FT-IR, TGA, and TPD-MS) is systematically applied to pure ammonium dawsonite-type compounds and materials incorporating other metals, such as La, Fe, and Mn. Mechanistic insights into the transformations of this versatile family of compounds to multimetallic mixed oxides, such as hexaaluminates, are studied as a function of their composition.

In **Chapter 3***,* characterization and performance evaluation of metal-substituted hexaaluminates in direct-N_2O decomposition are discussed. A complete

characterization of a number of lanthanum and barium hexaaluminates substituted by transition metals (Mn, Fe, Ni) is presented. The use of this family of oxides for high-temperature N_2O abatement in industrial sources, in ammonia burners of nitric acid, is highlighted on the basis of activity and stability tests under simulated conditions of temperature, space velocity, and gas composition.

Having shown metal-substituted hexaaluminates as promising and excellent options for N_2O decomposition at high temperature under realistic conditions in **Chapter 3**, **Chapter 4** deals with different methods to prepare the precursors, incorporating carbon as a template in order to increase the surface area [34]. Analyses of intermediate phases on transformation of the as-synthesized composites into the final hexaaluminates revealed fundamental understanding of the template action. The materials were characterized by ICP-OES, *in situ* and *ex situ* XRD, TEM, N_2 adsorption, He pycnometry, TGA, H_2-TPR, and XPS. Based on these analyses, aspects of the templating mechanism are discussed. Better performance was achieved in N_2O decomposition when carbon-templating route was used.

In **Chapter 5***,* barium-iron-hexaaluminate ($BaFeAl_{11}O_{19}$) was evaluated for N_2O decomposition under representative flue-gas conditions in fluidized-bed combustion and compared with several representative (benchmark) catalysts, including FeZSM-5, Co_2AlO_4, $LaCoO_3$.

Fluidized-bed combustion technology has attracted a rapidly growing interest, and a large number of commercial boilers of this type have been put into operation during the last years. Low emissions of nitric and sulphur oxides and fuel flexibility are the reasons behind this development. The low NO_x emission is a consequence of low temperature and reduction processes during combustion and the low SO_2 emission is a result of limestone addition to the combustion chamber, acting as a reactor for sulphur capture. However, it has been known that fluidized-bed boilers (FBBs) differs from conventional boilers by emitting significant amounts of nitrous oxide (N_2O), due to the low combustion temperature. Based on the results, opportunities in the implementation in fluidized-bed combustion are analyzed.

Chapter 6 reveals the kinetics and mechanism of N_2O decomposition over $BaFeAl_{11}O_{19}$ hexaaluminate via TAP reactor using the platform developed earlier by Kondratenko *et al.* [35-37] for studying the mechanism and microkinetics of iron-

containing zeolites. The aim of this analysis was (i) to identify mechanistic aspects governing the distinctive de-N_2O performance of $BaFeAl_{11}O_{19}$ and (ii) establish analogies and differences in direct N_2O decomposition over catalysts operating in high (>873K) and low-temperature (<723K).

Finally, **Chapter 7** brings the results presented throughout this thesis into perspective. Besides the findings and conclusions, expected future developments are discussed in this chapter too.

References

[1] K.L. Denman et.al. in Climate Change 2007.The Physical Science Basis. Contribution of Working Group I to the Fourth Assessment Report of the Intergovernmental Panel Control on Climate Change, S. Solomon, Eds. (Cambridge Univ. Press, Cambridge, 2007) 499.
[2] V. Ramanathan, R.J. Cicerone, H.H. Singh, J.T. Kiel, J. Geophys. Res. 90 (1985) 5547.
[3] IPCC 4th Assessment Report:Climate Change 2007: Synthesis Report.
[4] A.R. Ravishankara, J.S. Daniel, R.W. Portmann, Science 326 (2009) 123.
[5] J. Pérez-Ramírez, F. Kapteijn, K. Schöffel and J.A. Moulijn, Appl. Catal. B 44 (2003) 117.
[6] F. Kapteijn, J. Rodríguez-Mirasol, J.A. Moulijn, Appl. Catal. B 9 (1996) 25.
[7] EPA, 430-R-06-005, Global Mitigation of Non-CO_2 Greenhouse Gases, June 2006.
[8] J. Pérez-Ramírez, Catalyzed N_2O Activation. Promising (New) Catalysts for Abatement and Utilization, Ph.D. Thesis, Delft University of Technology, Delft, 2002.
[9] J. Pérez-Ramírez, F. Kapteijn, G. Mul, X. Xu, J.A. Moulijn. Catal. Today 76 (2002) 55.
[10] IPCC Guidelines for National GHG inventories, Chapter 3: Chemical Industry Emissions 2006.
[11] A. Shimizu, K. Tanaka, M.Fujimori, Chemosphere 2 (2000) 425.
[12] G. Kuhn, V. Schumacher, E. Wagner. Int. Fertil Soc. Proc. 435 (1999) 1.
[13] G. Kuhn, in Proceedings of the International Conference on Industrial Atmospheric Pollution, NO_x-N_2O Emission Control: Panel of Available Techniques, Session 4, ADEME Editions, Paris, 2001.
[14] G.I. Panov. CATTECH 4 (2000) 18.
[15] S. Alini, F. Basile, S. Blasioli, C. Rinaldi and A. Vaccari, Appl. Catal. B 70 (2007) 323.
[16] B. Neveu, C. Hamon, K. Malefant, French Patent WO 99/34901.
[17] M. Baier, T. Fettzer, O. Hofstadt, M. Hesse, G. Buerger, K. Harth, V. Schumacher, H. Wistuba, B. Otto, (BASF). WO0023176, 2000.
[18] S.A. Axon, D.R. Coupland, J.R. Foy, J. Ridland, I.C. Wishart (Johnson Matthey). WO040967-03A2, 2004.
[19] Ø. Nirisen, K. Schöffel, D. Waller, D. Øvrebø (Yara International). WO0202230, 2002.
[20] J. Pérez-Ramírez, F. Kapteijn, G. Mul, J.A. Moulijn, Chem. Commun. (2001) 693.
[21] J. Pérez-Ramírez, M. Santiago, Chem. Commun. (2007) 619.
[22] G. Giecko, T. Borowiecki, W. Gac and J. Kruk, Catal. Today 137 (2008) 403.

[23] M. Ruszak, M. Inger, S. Witkowski, M. Wilk, A. Kotarba, Z. Sokja, Catal. Lett. 126 (2008) 72.

[24] A. Ribera, I.W.C.E. Arends, S. de Vries, J. Pérez-Ramírez, R.A. Sheldon, J. Catal. 195 (2000) 287.

[25] J. Pérez-Ramírez, F. Kapteijn, J.C. Groen, A. Doménech, G. Mul, J.A. Moulijn, J. Catal. 214 (2003) 33.

[26] J. Pérez-Ramírez, F. Kapteijn, G. Mul, X. Xu, J.A. Moulijn, Catal. Today 76 (2002) 55.

[27] THAI CAPROLACTAM PCL N_2O Abatement in Tail Gas, http://www.tei.or.th/Event/eip/080709-ICS-CDM-N2O%20Abatement%20in%20Tail%20Gas.pdf.

[28] L. Armesto, H. Boerritger, A. Bahillo, J. Otero, Fuel 82 (2003) 1845.

[29] E. Tsupari, S. Monni, K. Tormonen, T. Pellikka, S. Syri, Int. J. Greenh. Gas Control 1 (2007) 289.

[30] J. Pérez-Ramírez, M.A.G. Hevia, S. Abelló, Chem. Commun. (2008) 5351.

[31] E. Ruiz-Martínez, J.M. Sánchez-Hervás, J. Otero-Ruiz, Appl. Catal. B 50 (2004) 195.

[32] E. Ruiz-Martínez, J.M. Sánchez-Hervás, J. Otero-Ruiz, Appl. Catal. B 61 (2005) 306.

[33] M.F.M. Zwinkels, S.G. Järås, P.G. Menon, T. A. Griffin, Catal. Rev.-Sci. Eng. 35 (1993) 319.

[34] F. Schüth, Angew. Chem. Int. Ed. 42 (2003) 3604 and references therein.

[35] E.V. Kondratenko, J. Perez-Ramirez, J. Phys. Chem. B 110 (2006) 22586.

[36] E.V. Kondratenko, J. Perez-Ramirez, Catal. Today 121 (2007) 197.

[37] E.V. Kondratenko, V.A. Kondratenko, M. Santiago, J. Perez-Ramirez, J. Catal. 256 (2008) 248.

UNIVERSITAT ROVIRA I VIRGILI
HEXAALUIMINATE-TYPE CATALYSTS FOR N2O ABATEMENT
Marta Santiago Redondo
ISBN:978-84-693-8864-8/DL:T.1943-2010

Chapter 2

Synthesis and thermal activation of dawsonite-type compounds to oxide catalysts

The thermal decomposition of metal-substituted ammonium aluminium carbonate hydroxide (AACH) materials with dawsonite-like structure has been studied by using *in situ* XRD, FT-IR, TGA, and TPD-MS in the temperature range 298-1573 K. The *in situ* approach enables accurate monitoring of the decomposition process and the nature and stability of the resulting oxide phases. This information is essential to optimize the thermal activation of these versatile materials for subsequent catalytic applications. Pure AACH and the corresponding substituted systems with La and/or transition metals (Fe or Mn) were synthesized by in line precipitation method using the carbonate route. *In situ* XRD indicated the destruction of the AACH phase at 473 K, independent of the composition of the material, leading to an amorphous alumina phase. This transition temperature is in excellent agreement with FT-IR, TGA, and TPD-MS data. The later techniques substantiate the one-step removal of H_2O, NH_3, and CO_2 within a narrow temperature range. In pure AACH, amorphous alumina is transformed into α-Al_2O_3 at 1373 K, while La-containing samples display the hexaaluminate structure above 1423 K. Incorporation of transition metals into the Al and La-Al systems promotes the formation of α-Al_2O_3 and hexaaluminate phases at significantly lower temperatures.

This chapter is based on the following publications:
M. Santiago, M.S. Yalfani, J. Pérez-Ramírez, J. Mater. Chem. 16 (2006) 2886.
M.S. Yalfani, M. Santiago, J. Pérez-Ramírez, J. Mater. Chem. 17 (2007) 1222.

1. Introduction

The mineral dawsonite, $NaAl(CO_3)(OH)_2$, named in 1874 after the Canadian geologist J. W. Dawson, forms by decomposition of aluminium silicates in the presence of carbonate/bicarbonate-rich solutions. The structure of this mineral is orthorhombic-disphenoidal (space group *Imam*), consisting of edge-sharing $AlO_2(OH)_4$ and $NaO_4(OH)_2$ octahedra and CO_3^{2-} groups [1,2]. Hydrogen bonding occurs between the Al chain and the CO_3^{2-} group, strengthening the three-dimensional framework [2]. Besides $NaAl(CO_3)(OH)_2$, a variety of compositions with dawsonite-type structures of generic formula $A_{2y+z-3x}M_x(CO_3)_y(OH)_z{\cdot}mH_2O$ have been synthesized using different reactants and phases (gas-liquid, gas-solid, and liquid-liquid) [3]. In this formula, A can be NH_4^+, an alkaline metal ion (K^+), an alkaline-earth metal ion (Mg^{2+}, Ca^{2+}, Ba^{2+}, Sr^{2+}), or a rare-earth cation (La^{3+}); M is typically a trivalent transition or non-transition metal cation (Al^{3+}, Cr^{3+}, Fe^{3+}), although divalent cations (Co^{2+}, Mn^{2+}) have also been incorporated into the structure [4-13].

Dawsonite-type compounds have been used as antacids, stabilizers, fire retardants, and increasingly as precursors for catalytic materials [7,10,14,15]. The latter application is motivated by the ability of these compounds to accommodate a large variety of divalent and trivalent cations, and the formation of high-surface area mixed oxides upon thermal activation. Several authors have been followed this route in order to achieve oxide materials with superior properties. However, the success depends strongly on the used synthesis method. *i.e*. Giannos *et al.* [7] obtained Al_2O_3 with surface areas of 450 $m^2\ g^{-1}$ and 145 $m^2\ g^{-1}$ after calcination at 973 K and 1273 K respectively, using a conventional batch precipitation, Ali *et al*. [3] extrapolated the dawsonite route to prepare bulk Cr_2O_3 and Fe_2O_3 by isomorphous substitution of Al by Cr or Fe in the precursor structure, but low-surface area oxides (<32 $m^2\ g^{-1}$) were obtained. Pitsch *et al.* [10] prepared bimetallic Fe-Al dawsonites by discontinuous precipitation using $NH_4Fe(SO_4)_2$ as the iron source and upon calcination at 873 K Fe_2O_3 with relatively high surface areas (up to 400 $m^2\ g^{-1}$ were attained).

Precipitation route is the most popular method to achieve oxides with better properties. However, two important drawbacks remain to be solved. First one is ineffective stirring leading to pH gradients in the reactor volume. The latter and more important is discontinuous operation, causing the residence time of the precipitate

UNIVERSITAT ROVIRA I VIRGILI
HEXAALUIMINATE-TYPE CATALYSTS FOR N2O ABATEMENT
Marta Santiago Redondo
ISBN:978-84-693-8864-8/DL:T.1943-2010

particles and concentration of reactants to change throughout the precipitation process, consequently changing the degree of nucleation and crystal growth between the start and the end product [16,17]. These prevent the maintenance of a constant product quality, which is often essential for the subsequent application of the resulting materials. On this basis, we introduced a continuous in-line dispersion precipitation (ILDP) method [18-20]. Figure 1 schematically shows the principle of the method.

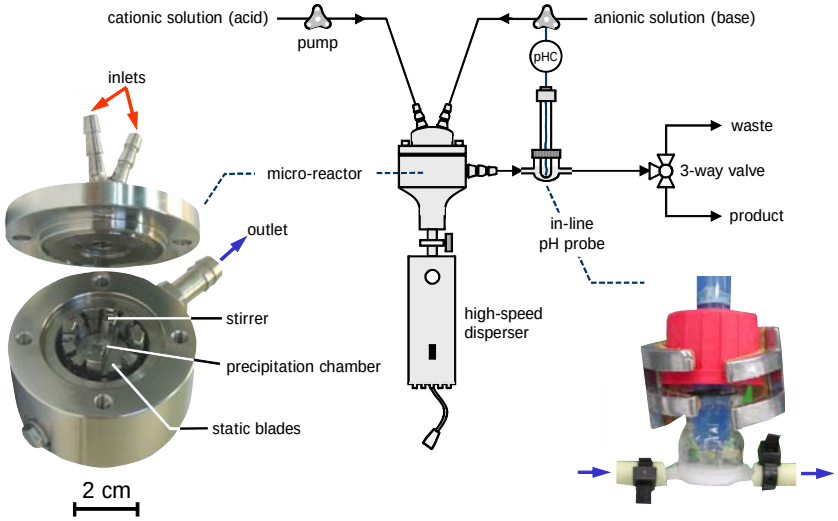

Figure 1. ILDP set-up, with photographs of the precipitation micro-reactor and the in-line pH probe.

The acid and base solutions are continuously fed by means of peristaltic pumps. The micro-reactor incorporates a rotating element attached to a high speed disperser (up to 24,000 rpm) and static blades in the periphery of the main axis that enable an impressively high degree of mixing in the miniaturized precipitation chamber leading to impeller Reynolds numbers up to 105 (turbulent regime at Re > 104)[21]. An in-line probe measures the pH of the slurry directly at the outlet of the micro-reactor and is connected to one of the pumps to maintain a constant pH.

The described configuration is in line with unit operations intensification in industry. Precipitation chamber is more compact and has higher productivity when compared to conventional batch precipitation. In a previous study, we illustrated the

benefits of this method by synthesizing metal-substituted dawsonites-type compounds with combinations of aluminium and various transition metal cations (Fe, Co, and Mn). Thermal activation of these materials up to 873 K led to mixed oxides with superior properties of component dispersion, surface area, thermal stability, and improved catalytic performance [18].

In addition, the incorporation of large cations such as barium, lanthanum, calcium, or strontium in the dawsonite structure (with or without additional transition metals) leads to hexaaluminates upon high-temperature treatment [22-24]. These materials exhibit a remarkable resistance towards sintering and thermal shock, and consequently have been successfully used in high-temperature catalytic applications, mainly for natural gas combustion in gas-turbine applications. Mn- and Fe-substituted La and Ba-hexaaluminates are regarded as the most thermally stable and active catalysts [5,8,9,25].

Monitoring the evolution during thermal activation of dawsonite-type compounds is of crucial importance for the proper utilization of the resulting oxide in catalysis. However, systematic investigations characterizing the thermal stability and decomposition mechanism of this family of materials are scarce. Groppi *et al.* [6] published a detailed XRD study on the phases formed upon calcination of Ba-Al dawsonite-type compounds to hexaaluminates in the temperature range 380-1670 K. However, as in most cases, the metamorphosis of the sample on heating was assessed by *ex situ* techniques [6,9,11,26-28]. *Ex situ* studies, where the sample is arrested at a certain temperature by quenching the reaction, followed by exposure to atmosphere, handling, and analysis of the product thereby obtained, have frequently proved to be unreliable. Instead, *in situ* monitoring of solid-state reactions is highly preferred, since the sample being analyzed is truly representative of the reaction matrix in real time [29,30]. Morinaga *et al*.[27] reported the only *in situ* study of the thermal decomposition of AACH, assessing the transformations of the different forms of alumina on heating by high-temperature XRD. We herein report on the evolution of metal-substituted dawsonite-type compounds during thermal treatment in air in the temperature range 298-1573 K. A combination of *in situ* techniques (HT-XRD, FT-IR, TGA, and TPD-MS) was systematically applied to pure AACH and materials incorporating other metals, such as La, Fe, and Mn. Mechanistic insights into the

transformations of this versatile family of compounds to multimetallic mixed oxides as a function of their composition are presented.

2. Experimental

2.1. Material preparation

Ammonium dawsonite-type compounds with aluminium and additional metals (denoted hereafter as A-B-Al, where A = La and B = Fe, Mn) were synthesized by co-precipitation using the carbonate route proposed by Groppi *et al*. [5] The nominal molar metal ratio in the binary and ternary systems was (A or B) : Al = 1 : 11 and A : B : Al = 1 : 1 : 11, respectively. The co-precipitation was carried out using the ILDP (in-line dispersion precipitation) method, whose features have been detailed elsewhere [18,19]. Briefly, an aqueous solution of the corresponding cations (1.1 M Al-nitrate, 0.1 M A-nitrate, and 0.1 M B-nitrate) acidified with concentrated nitric acid to pH 1, and an aqueous solution of ammonium carbonate ($(NH_4)_2CO_3$, 2 M) were continuously fed at 333 K to the precipitation micro-reactor (volume *ca.* 6 ml) by means of peristaltic pumps. Syntheses were carried out at a constant pH of 7.5-8, using a residence time of 18 s and a stirring speed of 13,500 rpm. The resulting slurry was aged at 333 K for 3 h, followed by filtration, washing, and drying at 378 K for 12 h. The metal precursors and precipitating agent used in the preparations were purchased from Panreac and Sigma-Aldrich and had purities >98%.

2.2. Techniques and procedures

The chemical composition of the as-synthesized samples was determined by inductive coupled plasma-optical emission spectroscopy (ICP-OES) (Perkin-Elmer Optima 3200RL (radial)). Elemental analysis (H, C, and N) was performed in a Carlo Erba EA1108 instrument.

X-Ray diffraction was carried out in a Siemens D5000 theta-theta diffractometer equipped with an Anton Paar HTK10 high-temperature chamber (volume *ca.* 1 l), a diffracted beam graphite monochromator using Ni-filtered CuKα radiation (λ= 1.5406 Å), and a Braun position-sensitive detector. A thin layer of sample (*ca.* 30 mg) was mounted on the platinum ribbon in the cell by placing a few droplets of a suspension

of finely ground powder in ethanol on the ribbon, followed by drying under ambient conditions. Great care was taken to minimize the specimen displacement effect by checking the exact position of the heater ribbon before every experiment and carefully reproducing the specimen installation.

In situ XRD patterns during thermal decomposition of the sample in static air at ambient pressure were recorded at intervals of 50 K in the temperature range 298-1573 K after 5 min equilibration at each temperature. The heating rate used was 5 K min^{-1}. The sample was directly heated by the alloy strip, whose temperature can be controlled within ±2 K. Diffractograms were acquired for the Bragg-Brentano geometry in the 2θ range 10-70° with a step size of 0.02° and a counting time per step of 4 s.

In situ Fourier transform infrared (FT-IR) spectra were recorded in a Thermo Nicolet 5700 Fourier transform spectrometer using a Spectratech collector II diffuse reflectance (DRIFT) accessory equipped with a high-temperature chamber and ZnSe windows. The transitions during thermal decomposition in air (20 cm^3 STP min^{-1}) were studied by placing the sample, previously diluted in KBr, on the ceramic holder of the cell. Spectra were collected at intervals of 25 or 50 K in the temperature range 298-823 K, using a heating rate of 5 K min^{-1}. The spectra were recorded in the range 650-4000 cm^{-1} directly after reaching every set-point, by co-addition of 256 scans and with a nominal resolution of 4 cm^{-1}.

Thermal analysis was carried out in a Mettler Toledo TGA/SDTA851e microbalance equipped with a 34-position sample robot. The solids (*ca*. 3 mg) were placed in 70 µl alumina crucibles without dilution. Analyses were performed in a dry air flow of 50 cm^3 STP min^{-1}. The temperature was ramped from 298 to 1173 K with a heating rate of 5 K min^{-1}.

The evolution of the gases during decomposition of the as-synthesized samples was studied by temperature-programmed desorption coupled to mass spectrometry (TPD-MS). *Ca.* 100 mg of sample were decomposed in air (100 cm^3 STP min^{-1}) in a quartz fixed-bed micro-reactor (10 mm i.d.), ramping the temperature from 298 K to 973 K at 5 K min^{-1}. Masses *m*/*z* 15 (NH_3), *m*/*z* 18 (H_2O), *m*/*z* 30 (NO), *m*/*z* 44 (CO_2), and *m*/*z* 46 (NO_2) were monitored by using a quadrupole mass spectrometer (Pfeiffer OmniStar GSD 301O).

3. Results and discussion

3.1. As-synthesized samples

The chemical composition of the as-synthesized samples determined by ICP-OES and elemental analysis is shown in (Table 1). The molar ratios between the substituted metal(s) and aluminium in the dried solids were very close to those in the starting solutions, indicating that the co-precipitation step was carried out effectively. The empirical formulas of the materials resemble that of AACH (ammonium aluminium carbonate hydroxide) reported by Vogel *et al*. [31] ($(NH_4)_2Al_6(CO_3)_3(OH)_{14}$ or $C_{0.5}H_{3.65}N_{0.3}O_{3.8}Al_{1.0}$) and differ from the ammonium-form of the dawsonite mineral ($NH_4AlCO_3(OH)_2$ or $C_{1.0}H_{6.0}N_{1.0}O_{5.0}Al_{1.0}$). Vogel *et al.* prepared AACH by precipitation of aluminium nitrate with ammonium hydroxide and ammonium bicarbonate at pH 8. Using the same reagents, Ali *et al*. [3] obtained a material with solid whose formula resembles more that of dawsonite, but the pH during precipitation was higher (11 instead of 8). Similarly, Morinaga *et al.* [27] obtained $NH_4AlCO_3(OH)_2$ by precipitation of $NH_4Al(SO_4)_2$ and NH_4HCO_3 at pH 10. Zhang *et al.* [13] demonstrated that pH values around 10 are optimal for synthesis of $NH_4AlCO_3(OH)_2$. Our data also confirm earlier postulates by Groppi *et al.* [5,6] who assumed the same chemical formula reported by Vogel *et al.* for AACH samples prepared using ammonium carbonate at pH 7.5-8.0. However, it should be noted that some of our samples using $(NH_4)_2CO_3$ are somewhat richer in aluminium than Vogel's formula obtained with NH_4OH and NH_4HCO_3 as precipitating agents.

Table 1. Chemical composition of the as-synthesized materials.

	La[a]	Fe[a]	Mn[a]	Al[a]	C[b]	H[b]	N[b]	O[c]	Empirical formula
Al	-	-	-	31.25	3.65	3.55	3.5	58.1	$C_{0.25}H_{3.0}N_{0.2}O_{3.1}Al_{1.0}$
Fe-Al	-	5.8	-	30.7	4.2	3.8	3.9	51.65	$C_{0.3}H_{3.3}N_{0.25}O_{2.85}Fe_{0.1}Al_{1.0}$
Mn-Al	-	-	5.35	26.7	4.55	3.5	3.55	56.4	$C_{0.4}H_{3.5}N_{0.25}O_{3.6}Mn_{0.1}Al_{1.0}$
La-Al	10.35	-	-	22.15	5.7	3.5	4.65	53.7	$C_{0.6}H_{4.2}N_{0.4}O_{4.1}La_{0.1}Al_{1.0}$
La-Fe-Al	8.9	3.65	-	18.7	5.2	3.5	4.4	55.65	$C_{0.6}H_{5.1}N_{0.45}O_{5.0}La_{0.1}Fe_{0.1}Al_{1.0}$
La-Mn-Al	9.05	-	3.85	19.6	5.5	3.2	3.4	55.4	$C_{0.6}H_{4.45}N_{0.3}O_{4.8}La_{0.1}Fe_{0.1}Al_{1.0}$

[a] ICP-OES. [b] Elemental analysis. [c] Calculated by difference.

UNIVERSITAT ROVIRA I VIRGILI
HEXAALUIMINATE-TYPE CATALYSTS FOR N2O ABATEMENT
Marta Santiago Redondo
ISBN:978-84-693-8864-8/DL:T.1943-2010

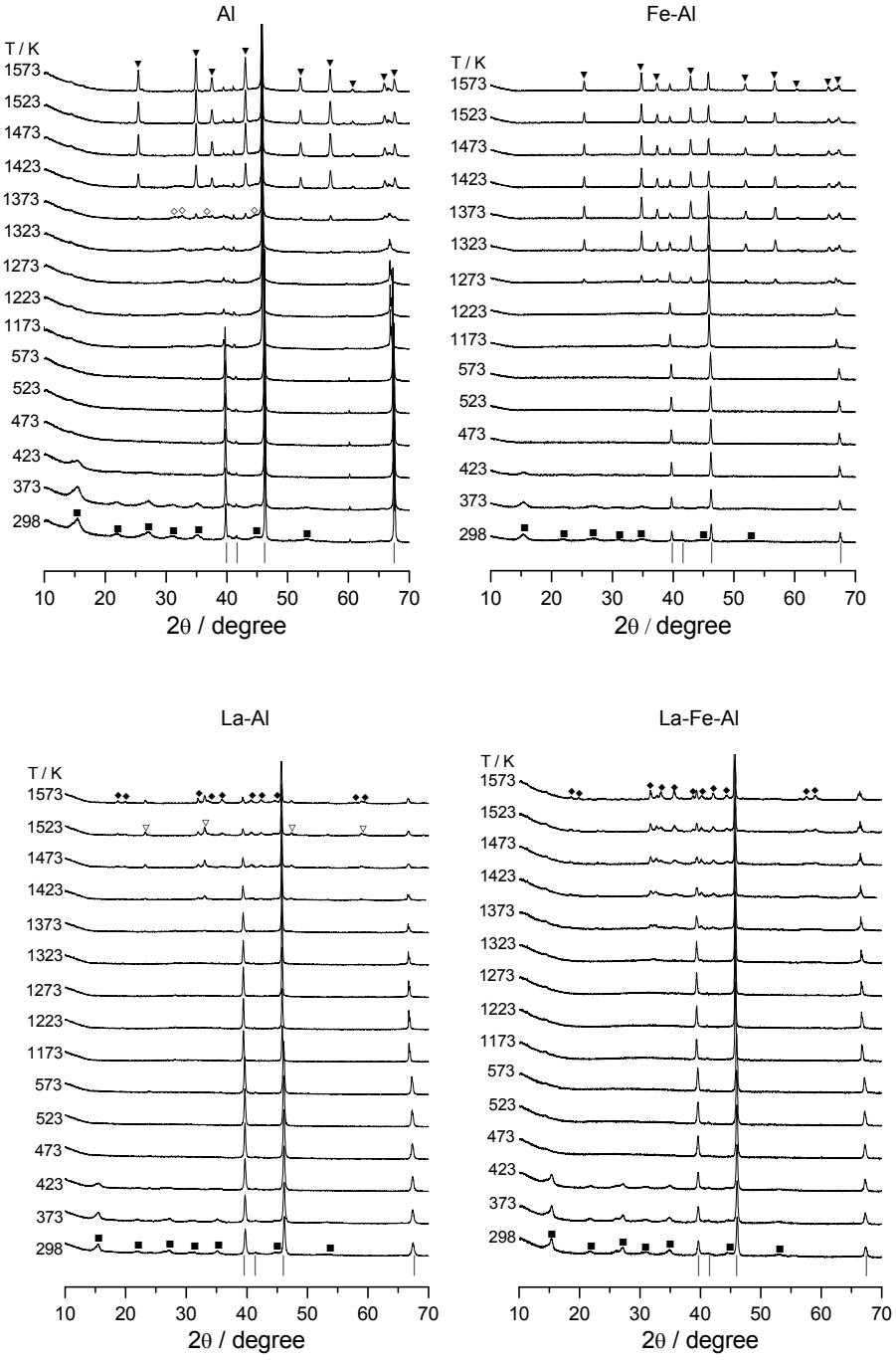

Figure 2. *In situ* XRD patterns during thermal decomposition of Al, Fe-Al, La-Al, and La-Fe-Al dawsonite-type compounds. Crystalline phases: (■) AACH, (◊) θ-Al_2O_3, (▽) $LaAlO_3$, (▼) α-Al_2O_3, (♦) $LaAl_{11}O_{18}$ or $LaFeAl_{11}O_{19}$. Vertical lines indicate the position of the main reflections of the Pt strip where the samples were mounted.

UNIVERSITAT ROVIRA I VIRGILI
HEXAALUIMINATE-TYPE CATALYSTS FOR N2O ABATEMENT
Marta Santiago Redondo
ISBN:978-84-693-8864-8/DL:T.1943-2010

As can be seen in the diffractograms at 298 K in (Figure 2 and 3), the XRD patterns of the as-synthesized samples show the characteristic reflections of ammonium aluminium carbonate hydroxide ($NH_4AlCO_3(OH)_2$, JCPDS 42-250). The material in this card was prepared by aging bohemite gel in a NH_4HCO_3 solution and was claimed to be iso-structural with $NaAlCO_3(OH)_2$ [32]. The patterns of our samples were indistinguishable from those measured by Vogel *et al.* [31] and Groppi *et al.* [6] (associated with $(NH_4)_2Al_6(CO_3)_3(OH)_{14}$). Accordingly, it can be concluded that the various AACH phases reported in the literature have a very similar crystal structure, being closely related to NH_4-dawsonite.

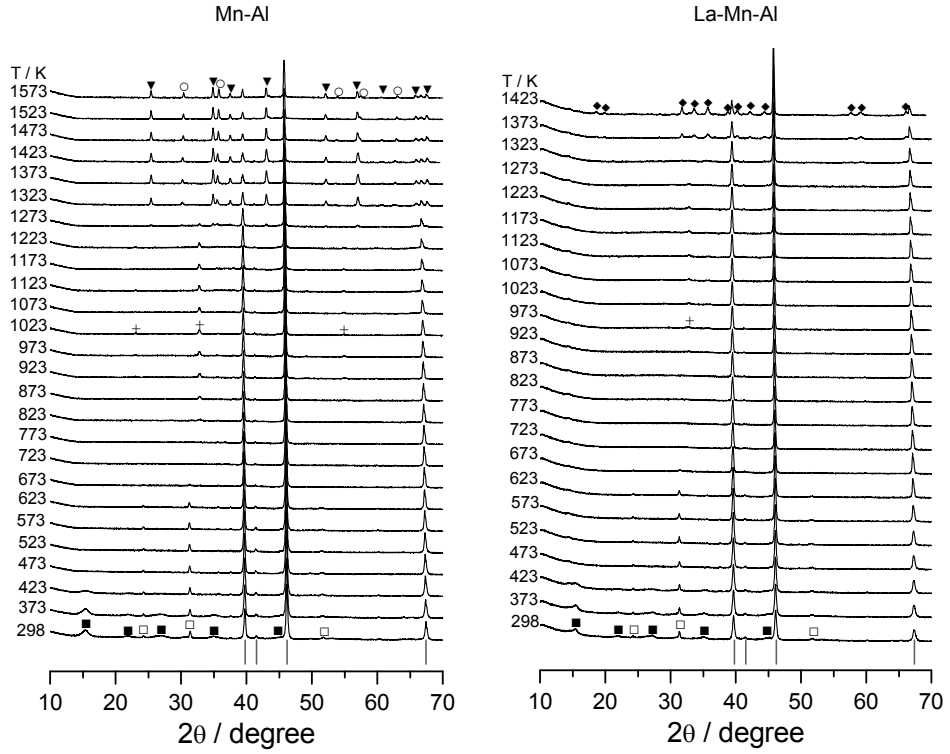

Figure 3. *In situ* XRD patterns during thermal decomposition of Mn-Al and La-Mn-Al dawsonite-type compounds. Crystalline phases: (■) AACH, (□) $MnCO_3$, (+) Mn_2O_3, (▼) α-Al_2O_3, (○) $MnAl_2O_4$, (♦) $LaMnAl_{11}O_{19}$. Vertical lines indicate the position of the main reflections of the Pt strip where the samples were mounted.

A marked broadening of the AACH reflections is observed in the diffractograms of the as-synthesized samples. The average crystallite size of the Al, Fe-Al, and Mn-Al

samples was estimated by the Scherrer equation applied to the (110) reflection at 15° 2θ, resulting in very similar values of *ca.* 4 nm. Somewhat larger crystallites were obtained in the La-containing samples (*ca.* 8 nm). The occurrence of very small dawsonite-type crystallites in the materials has been attributed to the particular characteristics of the applied ILDP method [18]. No additional iron-containing phase was present in the Fe-Al and La-Fe-Al dawsonite-type compounds, corroborating the statement by Pitsch *et al.* [10] that iron is located in the lattice structure of dawsonite. In contrast, the XRD patterns of the as-synthesized Mn-Al and La-Mn-Al samples (Figure 3) exhibit additional reflections of $MnCO_3$ (JCPDS 44-1472). The average crystallite size of this impurity was estimated to be *ca.* 30 nm. Groppi *et al.* [8,9] also identified this phase in the precursors of La-Mn-Al and Ba-Mn-Al hexaaluminates.

As shown in Figure 4 the FT-IR spectra of the as-synthesized materials at 298 K temperature exhibit the characteristic absorption bands of the hydroxyl, ammonium, and carbonate groups in dawsonite [3,11,33]. Table 2 provides a detailed band assignment. The absorption at 740 cm^{-1}, related to Al-O vibrations in the dawsonite structure, was observed too, being strongly overlapped with the ν_4 mode of the carbonate around 750 cm^{-1}. Al-O vibrations below 650 cm^{-1} were not visible in the spectra, since the *in situ* cell was equipped with ZnSe windows.

Table 2. Position of the bands (in cm^{-1}) in the infrared spectra of the dawsonite-type compounds.

Group	Mode	Al	Fe-Al	Mn-Al	La-Al	La-Fe-Al	La-Mn-Al
Hydroxyl	ν	3440	3440	3444	3438	3434	3438
	δ	989	991	991	991	995	991
Ammonium	ν	3175	3174	3176	3176	3174	3176
		3055	3083	3064	3037	3033	3037
		2850	2854	2858	2854	2858	2854
	δ	1832	1830	1832	1832	1832	1832
		1720	1720	1720	1722	1720	1722
Carbonate[a]	ν_3	1560	1550	1552	1564	1560	1564
		1452	1452	1454	1452	1452	1452
		1392	1394	1396	1394	1398	1394
	ν_1	1103	1103	1103	1105	1103	1105
	ν_2	854	854	856	852	852	852
	ν_4	754	754	754	754	750	750

[a] ν_1: Symmetric stretching; ν_2: out-of-plane deformation; ν_3: asymmetric stretching; ν_4: in-plane bending.

UNIVERSITAT ROVIRA I VIRGILI
HEXAALUIMINATE-TYPE CATALYSTS FOR N2O ABATEMENT
Marta Santiago Redondo
ISBN:978-84-693-8864-8/DL:T.1943-2010

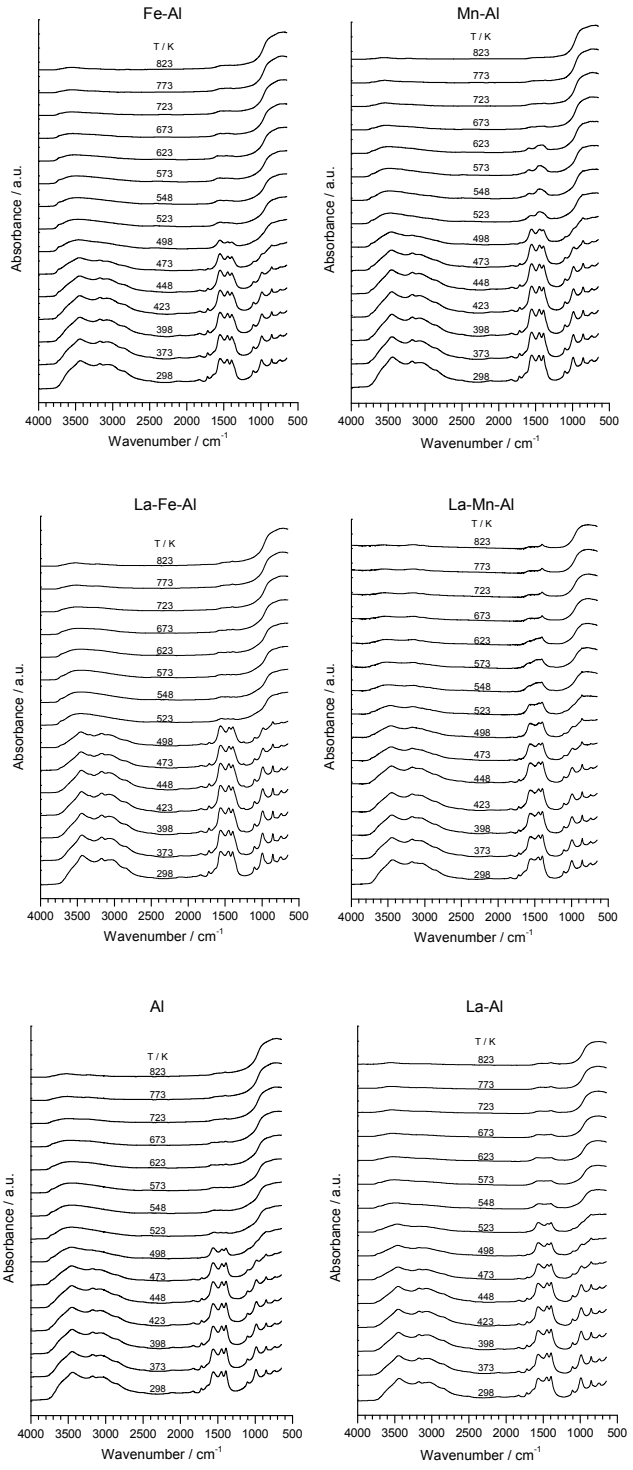

Figure 4. *In situ* FT-IR spectra during thermal decomposition of the dawsonite-type compounds.

3.2. Stability of the AACH phase

Figure 2 and 3 show the *in situ* XRD patterns obtained during thermal decomposition of the dawsonite-type compounds in air. The diffractograms clearly show that reflections of the AACH phase vanished at 473 K, leading to an amorphous phase. As shown in Figure 4, the decomposition of hydroxyl, ammonium, and carbonate groups in the samples as monitored by infrared spectroscopy mainly occurs in the range 498-523 K, in good correspondence with the destruction of the mineral structure according to XRD. The disappearance of the absorption bands of the various species appears to be simultaneous. This is substantiated by thermogravimetric analyses (Figure 5), presenting a one-step weight loss in the temperature range 420-480 K (maximum in the derivative curve at 460 K). The total weight loss amounts to *ca.* 50% in all the samples. This value is very close to the theoretical weight loss of the $(NH_4)_2Al_6(CO_3)_3(OH)_{14}$ formula proposed by Vogel *et al.* [31] (49.7%), further supporting the chemical composition analyses discussed in the previous section. The theoretical weight loss in the pure ammonium dawsonite $NH_4AlCO_3(OH)_2$ is *ca.* 63%.

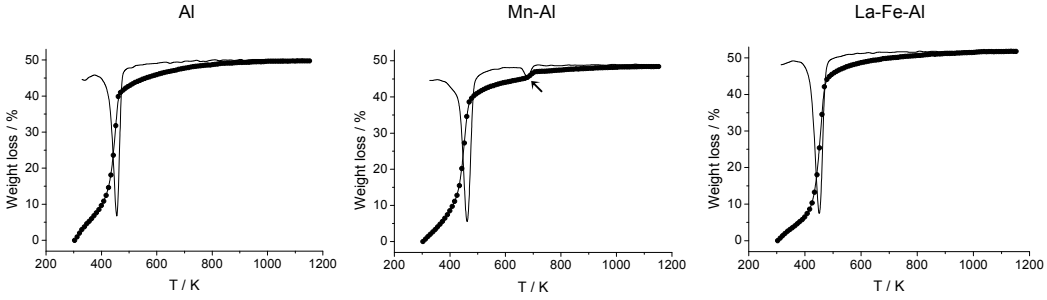

Figure 5. TGA-DGT profiles during thermal decomposition of selected dawsonite-type compounds in air at 5 K min^{-1}.

Further evidence for the single decomposition process of the dawsonite-type compounds in air was obtained by TPD-MS. This is exemplified for the Al sample in Figure 6. The masses associated with water, ammonia, and carbon dioxide simultaneously evolve from the sample, displaying a maximum at 480 K. The absence of NO and NO_2 at the reactor outlet was confirmed.

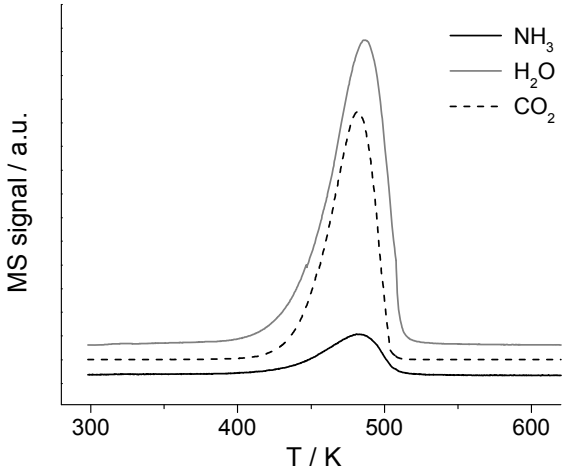

Figure 6. MS profiles during thermal decomposition of the Al sample in air at 5 K min^{-1}.

Studies in the literature assessing the thermal stability of the dawsonite-type compounds are scarce and lead to equivocal conclusions, since both one-step [6,27,31] and two-step [3,4,11] decomposition processes have been postulated. The *in situ* results in this study unequivocally demonstrate the one-step decomposition of the material. The thermal evolution and transition temperatures are remarkably similar over the different samples, indicating that the thermal stability is not influenced by the particular composition of the AACH phase.

3.3. Evolution of oxidic phases

Thermal decomposition of the dawsonite-type compounds leads to different oxidic phases as a function of temperature and metal combination in the material. This is summarized in Table 3 based on HT-XRD results and is elaborated below for each group of samples.

Pure Al sample. Decomposition of the AACH phase results in an amorphous phase in all materials. In general, temperatures above 1373 K were required in order to observe crystalline Al-containing phases. The infrared spectra of the sample above the decomposition temperature of the AACH phase according to this technique (523 K) exhibit very broad absorption bands in the OH stretching region. These surface hydroxyl species correspond to an amorphous alumina precursor phase, likely to be pseudobohemite (AlOOH). *Ex situ* diffraction studies of AACH decomposition reported

in the literature have shown that AlOOH is the most stable phase above 473 K, and is transformed into γ-Al_2O_3 at *ca.* 773 K [6].

In the Al sample, diffraction lines belonging to θ-Al_2O_3 (JCPDS 1-1304) and α-Al_2O_3 (JCPDS 10-173) coexisted in the pattern at 1373 K, while only α-Al_2O_3 is observed above 1423 K. In general, different transition phases such as γ-Al_2O_3, η-Al2O3, and θ-Al_2O_3 can be expected during thermal activation of the sample. As reviewed by Arai and Machida [34], γ-Al_2O_3 usually appears in the wide temperature range 773-1273 K, while η-Al_2O_3 and θ-Al_2O_3 are formed in the narrow temperature ranges 1273-1373 K and 1373-1423 K, respectively. Morinaga *et al.*[27] identified the presence of γ-, θ-, and α-Al_2O_3 upon calcination of AACH in the range 723-1323 K followed by isothermal annealing for up to 24 h at each temperature. However, γ-Al_2O_3 did not appear in the XRD pattern when the experiment was performed in continuous mode, *i.e.* heating the sample in air with holding time of 6 h at each temperature. This is in excellent agreement with our HT-XRD results, revealing the very slow crystallization of the γ-alumina phase.

Table 3. Crystalline phases at selected temperatures during thermal decomposition of the dawsonite-type compounds in air.

T/K	Al	Fe-Al	Mn-Al	La-Al	La-Fe-Al	La-Mn-Al
298	AACH[a]	AACH	AACH $MnCO_3$	AACH	AACH	AACH $MnCO_3$
473	-	-	$MnCO_3$	-	-	$MnCO_3$
873	-	-	Mn_2O_3	-	-	-
1273	-	α-Al_2O_3	α-Al_2O_3 Mn_2O_3	-		Mn_2O_3
1373	θ-Al_2O_3 α-Al_2O_3	α-Al_2O_3	α-Al_2O_3 $MnAl_2O_4$	-	$LaFeAl_{11}O_{19}$	$LaMnAl_{11}O_{19}$
1573	α-Al_2O_3	α-Al_2O_3	α-Al_2O_3 $MnAl_2O_4$	$LaAl_{11}O_{18}$ $LaAlO_3$	$LaFeAl_{11}O_{19}$	$LaMnAl_{11}O_{19}$

[a]AACH: ammonium aluminium carbonate hydroxide (JCPDS 42-250).

Fe- and Mn-substituted samples. The thermal evolution of the Fe-Al sample resembles that of the Al sample with respect to (i) the formation of an amorphous γ-Al_2O_3 phase after destruction of the dawsonite-type structure and (ii) the formation of α-Al_2O_3 upon calcination at 1573 K. In contrast, the presence of iron promotes the formation of crystalline α-Al_2O_3 at a temperature *ca.* 100 K lower than for the pure Al system. In addition, other intermediate forms of alumina (*e.g.* θ-Al_2O_3) were not

detected. Neither iron oxide nor iron-aluminium spinel were observed in XRD, further highlighting the high dispersion and resistance to sintering of this transition metal upon thermal treatment of the AACH precursor [10,18].

Besides AACH, the as-synthesized Mn-Al sample contains $MnCO_3$ as an impurity. The latter phase is stable up to 623 K (Figure 3). The presence of manganese carbonate is further substantiated by FT-IR (Figure 4). Bands associated with carbonates in the Al and Fe-Al samples are virtually absent above 523 K due to decomposition of the dawsonite-type structure. However, the Mn-Al sample exhibits significant absorptions at 1460 cm^{-1} and 1560 cm^{-1} (ν3 mode) and 852 cm^{-1} (ν2 mode) up to 623 K. This is in excellent agreement with the disappearance of the $MnCO_3$ reflections in HT-XRD. The decomposition of manganese carbonate was also monitored in thermal analysis. As can be seen in the TGA profile of the Mn-Al sample in Figure 5, a weight loss of <5% was observed at 600-680 K, coinciding with the decomposition temperature determined by HT-XRD and *in situ* FT-IR. The associated weight loss is small compared to the *ca.* 50% weight loss due to the dawsonite decomposition, giving an idea of the relatively low level of $MnCO_3$ impurity in the sample.

Upon decomposition of $MnCO_3$, an amorphous phase is formed in the temperature interval 673-773 K. At 823 K, characteristic reflections of Mn_2O_3 (JCPDS 41-1442) are evidenced, being stable up to 1273 K. The Mn_2O_3 phase is stable in the temperature range 823-1223 K, and its disappearance is coupled with the formation of α-Al2O3. As a consequence, manganese oxide transforms into manganese aluminate ($MnAl_2O_4$, JCPDS 29-880). Similarly to what was observed in the Fe-Al system, the substitution of manganese in the dawsonite-type structure leads to the formation of α-Al_2O_3 at 1273 K, *i.e.* at a temperature 100 K lower than over the pure Al sample. Therefore, it can be unequivocally concluded that transition metals such as Fe and Mn can promote phase transition reactions of alumina at lower temperatures. Very similar results were obtained with dawsonite-type compounds substituted by other transition metals (*e.g.* Co-Al, Ni-Al) (not described in this manuscript for the sake of conciseness).

The α-Al_2O_3 cell parameters in the Al, Fe-Al, and Mn-Al samples was calculated from the (110) reflection at 25° 2θ, and is shown in Table 4. This was determined from *ex situ* patterns, measured after thermal treatment of the samples at 1573 K and cooling of the cell to room temperature, in order to avoid thermal expansion effects at

high temperature. The presence of transition metal cations leads to somewhat larger cell sizes, likely due to their incorporation in the α-alumina lattice. This is particularly true for the Fe-Al sample. Mn induces a less pronounced effect in the α-Al_2O_3 cell than Fe, presumably due to the involvement of some of the manganese in a separate $MnAl_2O_4$ spinel phase. As shown in Figure 7, the α–Al_2O_3 formed by decomposition of the Fe-Al and Mn-Al samples consists of somewhat larger crystallites than that obtained from the pure Al sample. This result can be expected because of the promoted crystallization of the α–alumina phase in the presence of transition metals.

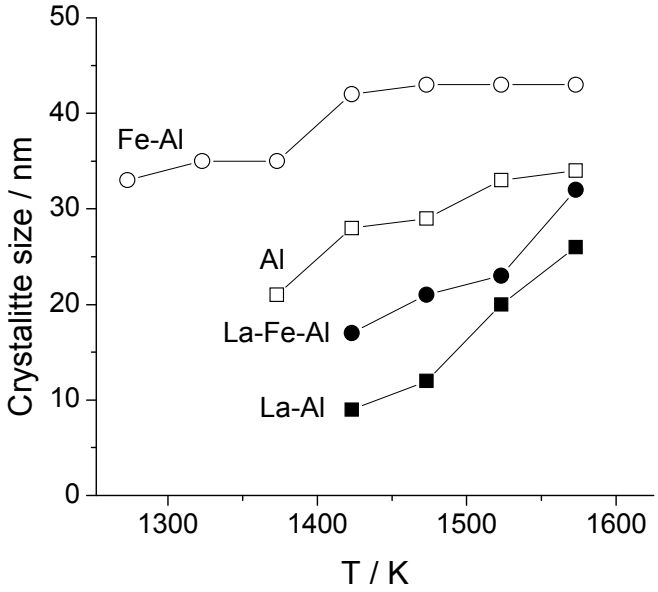

Figure 7. Evolution of the average crystallite size of α-Al_2O_3 and hexaaluminate phases with temperature.

Table 4. Cell parameter a of the oxide phases as determined from XRD analysis of the samples at room temperature after the *in situ* experiments shown in Figure 2 and 3.

Sample	Phase	Cell parameter a/nm
Al	α-Al_2O_3	0.5093
Fe-Al	α-Al_2O_3	0.5119
Mn-Al	α-Al_2O_3	0.5097
La-Al	Hexaaluminate	0.5565
La-Fe-Al	Hexaaluminate	0.5598
La-Mn-Al	Hexaaluminate	0.5605

La-substituted samples. As for Al and Fe-Al, the La-Al and La-Fe-Al samples underwent the formation of an amorphous phase upon decomposition of the dawsonite-type structure, lasting up to temperatures of 1373 K. As expected, an $MnCO_3$ phase was also present in the as-synthesized La-Mn-Al, decomposing to Mn_2O_3 at the sample temperature, as in Mn-Al (see XRD patterns in Figure 3). The XRD pattern of the La-Al system evidences the formation of hexaaluminate ($LaAl_{11}O_{18}$, JCPDS 36-699) and lanthanum aluminate ($LaAlO_3$, JCPDS 31-022) at 1423 K (Figure 2). In the presence of lanthanum, the hexaaluminate phase is formed at higher temperature (1423 K), compared with the formation of α-Al_2O_3 at 1373 K in the samples without lanthanum. Hexaaluminates consist of alternate stacking along the c-axis of γ-Al_2O_3 spinel blocks and mirror planes in which rare-earth (La^{3+}), large alkaline (K^{+}), or alkaline-earth cations (Ba^{2+}, Ca^{2+}, Sr^{2+}) are located [9,34,35].

As shown in Figure 2 and 3, incorporation of transition metals (Fe and Mn) in the La-Al sample leads to the formation of the corresponding hexaaluminate as $LaFeAl_{11}O_{19}$ or $LaMnAl_{11}O_{19}$ (JCPDS 36-1314 and 36-1317, respectively) at lower temperature (1373 K) than in the non-substituted La-Al sample (1423 K). In other words, insertion of transition metals within the structure of the AACH precursor lowers the temperature at which single-phase hexaaluminate is obtained. Groppi *et al.* [9] showed that partial substitution of Al^{3+} by Mn^{2+} and especially Mg^{2+} ions promoted the formation of monophasic La-hexaaluminates after calcination at 1573 K for 10 h, through a charge compensation mechanism.

Analogously to the samples without lanthanum, the transition metal-substituted La-hexaaluminates display larger average crystallite sizes than the non-substituted La-hexaaluminate (Figure 8). In agreement with the literature, the hexaaluminates possess significantly smaller crystallites than α-Al_2O_3 due to the inhibited crystal growth along their *c*-axis [9,34,35]. In order to confirm the presence of transition metals within the hexaaluminate structure, the cell parameter *a* was calculated taking the (110) reflection at 32° 2θ (Table 4). Values of *a* in the transition-metal-containing hexaaluminates were higher than that of the non-substituted one. This indicates that the larger Mn and Fe ions are located in the hexaaluminate structure, replacing smaller Al^{3+} ions.

4. Conclusions

A combination of *in situ* methods (XRD, FT-IR, TGA, and TPD-MS) made it possible to precisely monitor the evolution of metal-substituted dawsonite-type compounds upon thermal decomposition. The various techniques complement each other and provide information on phase transitions in the temperature range 298-1573 K. This is required to design optimal activation conditions for catalytic application of this versatile family of materials. The transition temperature at which dawsonite structure collapsed (*ca.* 473 K) is independent of the metal composition of the samples. The relatively low thermal stability of dawsonites is also characterized by the simultaneous removal of water, carbonates, and ammonium ions within a very narrow temperature range. The measured weight loss in our samples is in excellent agreement with the general AACH formula of $(NH_4)_2Al_6(CO_3)_3(OH)_{14}$, in line with chemical composition analyses. The occurrence of an amorphous Al-containing phase in the wide temperature range 473-1323 K during the *in situ* investigation reveals the remarkable resistance of γ-Al_2O_3 to crystallization. This contrasts with *ex situ* XRD approaches with long annealing periods, in which this phase was identified as an intermediate on the way to α-Al_2O_3. The pure Al and La-Al samples undergo transformation into α-Al_2O_3 and hexaaluminate at 1373 K and 1423 K, respectively. Substitution in the as-synthesized materials of transition metal cations promotes the appearance of these oxide phases at temperatures 50-100 K lower.

5. Acknowledgements

Dr F. Guirado (Servei de Recursos Científics, URV) is acknowledged for performing the X-ray diffraction analyses. M.S. Yalfani is acknowledged for his cooperation in this chapter.

References

[1] A.J. Frueh, J.P. Golightly, Can. Mineral. 9 (1967) 51.
[2] E. Corazza, C. Sabelli, S. Vannucci, Neues Jahrb. Mineral. Monatsh. 9 (1977) 381.
[3] A.A. Ali, M.A. Hasan, M.I. Zaki, Chem. Mater. 17 (2005) 6797 and references therein.
[4] H. Hernández, M.A. Ulibarri, J.Cornejo, M.J. Peña, C. J. Serna, Thermochim. Acta 94 (1985) 257.
[5] G. Groppi, M. Bellotto, C. Cristiani, P. Forzatti, P. L. Villa, Appl. Catal. A 104 (1993) 101.

[6] G. Groppi, C. Cristiani, P. Forzatti, M. Bellotto, J. Mater. Sci. 29 (1994) 3441.
[7] M. Giannos, M. Hoang, T.W. Turney, Chem. Lett. (1998) 793.
[8] L. Lietti, C. Cristiani, G. Groppi, P. Forzatti, Catal. Today 59 (2000) 191.
[9] G. Groppi, C. Cristiani, P. Forzatti, Appl. Catal. B 35 (2001) 137.
[10] I. Pitsch, W. Geßner, A. Brückner, M. Mehner, S. Möhmel, D.C. Ueckera, M.M. Pohl, J. Mater. Chem. 11 (2001) 2498.
[11] C.C. Ma, X.X. Zhou, X. Xu, T. Zhu, Mater. Chem. Phys. 72 (2001) 374.
[12] T.F. Yeh, H.G. Lee, C.B. Wang, in The 30th NATAS Annual Conference on Thermal Analysis and Application (2002) 263.
[13] X. Zhang, Z. Wen, Z. Gu, X. Xu and Z. Lin, J. Solid State Chem. 177 (2004) 849.
[14] C.J. Serna, J.L. White, S.L. Hem, J. Pharm. Sci., 1978, 67,324-327. 15 P. V. Bonsignore, Plast. Eng. 32 (1976) 41.
[16] Handbook of Heterogeneous Catalysis, ed. F.Schütz, K. Unger, G. Ertl, H. Knözinger, J. Weitkamp, VCH, Weinheim, 1997, vol. 2, pp. 72.
[17] P. Courty, C. Marcilly, in A. scientific approach to the preparation of bulk mixed catalysts, ed. G. Poncelet, P.Grange and P.A. Jacobs, Elsevier, Amsterdam, 1983, p. 488.
[18] M. Santiago, M.S. Yalfani, J. Pérez-Ramírez, J. Mater. Chem. 16 (2006) 2886.
[19] S. Abelló, J. Pérez-Ramírez, Adv. Mater. 18 (2006) 509.
[20] J. Pérez-Ramírez, S. Abelló Cros, M. Santiago Redondo, WO 2007147881 (2007)
[21] R.H. Perry, D.W. Green, J.O. Maloney, Perry's Chemical Engineer´s Handbook, McGraw-Hill, New York. 7th edn, 1997.
[22] M. Machida, K. Eguchi, H. Arai, Chem. Lett. (1986) 151.
[23] M. Machida, K. Eguchi, H. Arai, J. Catal. 103 (1987) 385.
[24] M.F.M. Zwinkels, S.G. Järås, P.G. Menon, T.A. Griffin, Catal. Rev-Sci. Eng. 35 (1993) 319.
[25] M. Machida, K. Eguchi, H. Arai, J. Catal. 120 (1989) 377.
[26] A. Ersson, K. Persson, I.K. Adu, S.G. Järås, Catal. Today 112 (2006) 157.
[27] K. Morinaga, T. Torikai, K. Nakagawa, S. Fijino, Acta Mater. 48 (2000) 4735.
[28] X. Zhang, Z. Wen, Z. Gu, X. Xu, Z. Lin, Thermochim. Acta 433 (2005) 116.
[29] G.R. Williams, D.O'Hare, J. Mater. Chem. 16 (2006) 3065.
[30] J. Pérez-Ramírez, G. Mul, F. Kaptejin, J.A. Mouljin, J. Mater. Chem. 11 (2001) 821.
[30] R.F. Vogel, G. Marcelin, W.L. Kehl, Appl. Catal. 12 (1984) 234.
[31] T. Iga, S. Kato, J. Ceram. Soc. Jpn. 86 (1978) 509.
[32] C.J. Serna, J.V. Garcia-Ramos, M.J. Peña, Spectrochim. Acta Part A 41 (1985) 697.
[33] H. Arai, M. Machida, Appl. Catal. A 138 (1996) 161
[34] J.G. McCarty, M.Gusman, D.M. Lowe, H.K.N. Lau, Catal. Today 47 (1999) 5.

UNIVERSITAT ROVIRA I VIRGILI
HEXAALUIMINATE-TYPE CATALYSTS FOR N2O ABATEMENT
Marta Santiago Redondo
ISBN:978-84-693-8864-8/DL:T.1943-2010

UNIVERSITAT ROVIRA I VIRGILI
HEXAALUIMINATE-TYPE CATALYSTS FOR N2O ABATEMENT
Marta Santiago Redondo
ISBN:978-84-693-8864-8/DL:T.1943-2010

Chapter 3

Decomposition of N_2O over hexaaluminate-type catalysts

Catalytic N_2O decomposition has been studied over metal-substituted hexaaluminates with the general formula $ABAl_{11}O_{19}$, where A = La, Ba, and B = Mn, Fe, Ni. The materials were prepared by coprecipitation via the carbonate route followed by calcination at 1473 K for 10 h. Inductively coupled plasma-optical emission spectroscopy (ICP-OES), X-ray diffraction (XRD), transmission electron microscopy (TEM), and N_2 adsorption techniques were used to characterize the catalysts. The activity in direct N_2O decomposition was evaluated by means of temperature programmed reaction and steady-state experiments. Fe- and Mn-containing hexaaluminates present the highest activities. The Ni-containing catalysts are significantly less active, comparable to the hexaaluminates without metal substitution. The catalytic activity was practically not influenced by the A cation (La or Ba) in the structure. The Fe- and Mn-substituted hexaaluminates exhibit high activity and stability for N_2O decomposition in mixtures simulating the outlet of the Pt-Rh gauzes in ammonia oxidation reactors, containing N_2O, NO, O_2, and H_2O. These materials are promising for high-temperature abatement of this powerful greenhouse gas in the chemical industry, particularly in nitric acid and caprolactam production.

This chapter is based on the following publications:
M. Santiago, J. Pérez-Ramírez, Environ. Sci. Technol. 41 (2007) 1704.
J. Pérez-Ramírez, M. Santiago, Chem. Commun. (2007) 619.

1. Introduction

N_2O mitigation is an important topic due to the adverse consequences of this harmful gas in our atmosphere [1,2]. Nitric acid plants currently represent the largest single source of N_2O in the chemical industry (400 kton N_2O/year), formed as a by-product of ammonia oxidation over the Pt-Rh alloy gauzes [3]. Research programs were initiated in the late 1990s in order to develop de-N_2O technologies in nitric acid production. The latter were partly motivated by moral pressure from adipic acid manufacturers, who voluntarily committed to reduce the emission from 600 to 100 kton N_2O/year [4], and later reinforced by incipient regulations and policies. Flexible mechanisms to reduce emissions of greenhouse gases associated with the Kyoto protocol [5], such as the International Emissions Trade, Joint Implementation, and Clean Development Mechanism, represent additional incentives for industrialized countries to implement N_2O mitigation technology.

As reviewed elsewhere [3], abatement options in different locations of the nitric acid plant have been investigated. Direct N_2O decomposition below the noble metal gauzes in the ammonia burner (process-gas decomposition) and in the tail-gas train (tail-gas decomposition) are the most cost-effective abatement measures for existing nitric acid plants. In the tail gas, Uhde is commercializing the EnviNOx process for the combined removal of N_2O and NO_x in a single fixed-bed reactor by use of iron-containing zeolites [6]. For process-gas N_2O abatement, three main catalytic systems are described in the patent literature [7-11]: CuO/Al_2O_3 (BASF), $La_{0.8}Ce_{0.2}CoO_3$ (Johnson Matthey), and Co_2AlO_4/CeO_2 (Yara International). A major advantage of process-gas decomposition is the universal application in all nitric acid plants. In contrast, N_2O abatement by use of iron zeolites is prohibitive in low-temperature tail gases (<673 K), since addition of reducing agents and gas preheating is required [3,12].

In contrast with the vast number of works dealing with end-of-pipe N_2O abatement [3], no study has been published in the open literature on design strategies and performance of process-gas (high temperature) de-N_2O catalysts. Successful process-gas catalysts should be active in order to achieve high N_2O conversions, but ensuring high chemical stability and mechanical robustness at the extreme conditions of temperature and gas composition in the burner (1073-1173 K, wet oxidizing atmosphere) is critical to fulfill a long lifetime and safe operation. Because of this,

component volatilization and solid-state reactions between active phase and support leading to catalyst deterioration must be emphatically avoided.

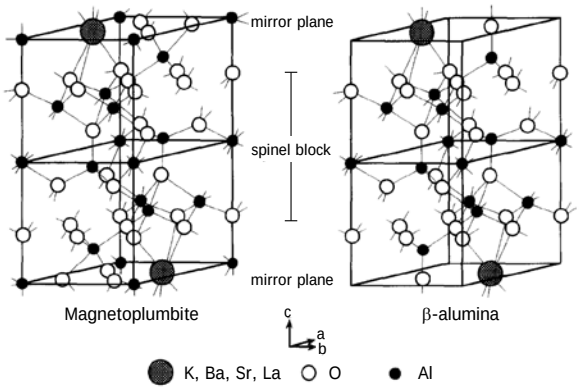

Figure 1. Hexaaluminate structures, showing the arrangement of Al^{3+}-containing spinel blocks and the mirror planes containing large cations.

Attending to these requirements, metal-substituted hexaaluminates can be considered as promising candidates toward active and durable catalysts for high-temperature N_2O decomposition. These oxides exhibit stable phase composition up to 1873 K and high resistance toward sintering and thermal shock [13,14]. They have been namely applied for catalytic combustion of natural gas in gas-turbine applications involving temperatures up to 1773 K [13-18]. The outstanding thermal stability of hexaaluminates is associated with their layered structure, consisting of alternate stacking along the c-axis of γ-Al_2O_3 spinel blocks and mirror planes in which large alkaline (K^+), alkaline-earth (Ba^{2+}, Ca^{2+}, Sr^{2+}), or rare-earth (La^{3+}) cations are located. Depending on the composition and the defectivity of the mirror plane, β-alumina or magnetoplumbite-like structures are obtained (Figure 1). These materials typically crystallize as hexagonal planar particles with strong anisotropic shape, because the grain growth along the direction of the c-axis is very slow due to inhibition of ion diffusion along the stacking direction [19]. Substitution of transition metal ions in Al^{3+} positions of the spinel blocks enables to introduce redox-active (catalytic) sites in the structure with little effect on the sintering resistance of the material [13,14]. In combustion applications, Mn- and Fe-substituted lanthanum and barium

hexaaluminates are generally found as the most thermally stable and active catalysts [15-18].

In this chapter, we have systematically prepared and characterized lanthanum and barium hexaaluminates substituted by transition metals (Mn, Fe, Ni). The catalytic performance of these materials in direct N_2O decomposition has been evaluated. The application of this family of oxides for high-temperature N_2O abatement in industrial sources, for example, in ammonia burners of nitric acid or caprolactam plants, is highlighted on the basis of activity and stability tests under simulated conditions of temperature, space velocity, and gas composition.

2. Experimental

2.1. Catalyst preparation

The preparation of hexaaluminates with formula $ABAl_{11}O_{19}$, (where A = La, Ba and B = Mn, Fe, Ni) involved the coprecipitation of dawsonite-type compounds via the carbonate route [16], followed by high temperature calcination. The coprecipitation was carried out using the ILDP (in-line dispersion precipitation) method [20]. An aqueous solution of the corresponding cations (1.1 M aluminium nitrate, 0.1 M "A" nitrate, and 0.1 M "B" nitrate) and an aqueous solution of ammonium carbonate ($(NH4)_2CO_3$, 2M) were continuously fed at 333 K to the precipitation microreactor. Syntheses were carried out at constant pH 7.5-8, with a residence time of 18 s and a stirring speed of 13,500 rpm. The resulting slurry was aged at 333 K for 3 h, followed by filtration, thorough washing, and drying. The dried solids were calcined in static air at 1473 K for 10 h with a ramp of 10 K min^{-1}.

2.2. Characterization

The chemical composition of the calcined materials was determined by inductively coupled plasma-optical emission spectroscopy (ICP-OES) [Perkin-Elmer Optima 3200RL (radial)]. Before analysis, the solid samples were treated following a home-developed alkaline fusion method with NaOH and Na_2O_2, followed by dilution with HCl.

Powder X-ray diffraction patterns were acquired in transmission on a Bruker AXS D8 Advance diffractometer equipped with a Cu tube, a Ge(111) incident beam

monochromator (λ = 1.5406 Å), and a Vantec-1 position-sensitive detector. Data were recorded in the 2θ range of 5-70° with an angular step size of 0.016° and a counting time of 2.4 s/step.

Transmission electron microscopy (TEM) was carried out in a JEOL JEM-1011 microscope. The samples were mounted onto a carbon-coated copper grid by placing a few droplets of a suspension of the powder sample in ethanol, followed by evaporation at ambient conditions.

N_2 adsorption at 77 K was performed in a Quantachrome Autosorb 1-MP gas adsorption analyzer. Prior to analysis, the samples were evacuated at 473 K for 12 h. The Brunauer-Emmett-Teller (BET) method [21] was applied to determine the total surface area.

2.3. Catalytic tests

Catalytic tests were carried out in a quartz fixed-bed reactor (10 mm i.d.) with 200 mg of sample (sieve fraction 200-300 mm), a total pressure of 1 bar, and a weight-hourly space velocity (WHSV) of 30,000 ml g^{-1} h^{-1}. Two protocols were applied for catalytic evaluation. Temperature-programmed reaction (TPR) was carried out by ramping the temperature from 673 to 1273 K at 5 K min^{-1} in a mixture of 5000 ppm N_2O in He. Steady-state tests were conducted isothermally in the range 673-1123 K in a mixture of 1500 ppm N_2O in He. The catalytic performance was also evaluated in a mixture of N_2O (1500 ppm), O_2 (10 vol.%), NO (1.5 vol.%), and H_2O (10 vol.%). The latter simulates the outlet gas of the Pt-Rh gauzes in ammonia burners. Generally, 30 min after a change of conditions, the conversion levels were constant and considered as the steady state. Prior to the tests, the catalysts were pretreated at 673 K in the corresponding feed mixture for 1 h. The degree of N_2O conversion was determined from analysis by mass spectrometry (Pfeiffer OmniStar GSD 3010) in TPR tests and by gas chromatography (SRA Instruments Micro-GC 3000) in steady-state tests.

3. Results and discussion

3.1. Catalyst characterization

X-ray diffraction of Al and La-Al dried precipitates exhibited reflections of ammonium aluminium carbonate hydroxide (AACH) phase ($NH_4Al(CO_3)(OH)_2$, JCPDS 42-250). The Ba-containing precipitates namely present the AACH phase, but additionally Ba-Al mixed compounds such as $BaAl_2(CO_3)_2(OH)_4 \cdot 2H_2O$ (JCPDS 31-116) and $Ba_2Al_4(OH)_{16}$ (JCPDS 24-16). Addition of the transition metal does not change the observed phases except for the manganese-containing samples, where $MnCO_3$ (JCPDS 44-1472) appeared as an impurity. Besides, the Ni-containing samples were virtually amorphous. The above XRD observations are in correspondence with works in the literature where the carbonate route is used to synthesize precursors for metal substituted hexaaluminates [17,22,23].

The chemical composition of the calcined samples as determined by ICP-OES is shown in Table 1. The content of A (Ba, La) and B (Mn, Fe, Ni) varied in the range of 16-19 and 5.5-7.5 wt.%, respectively. In general, the molar ratios between Al and the A and/or B metals in the solid were very close to the nominal values, indicating that the coprecipitation step was carried out effectively. The Al/Ni ratio in the nickel-containing samples was somewhat higher than the nominal value of 11. The filtrates during preparation of these samples had a slight green colour, suggesting incomplete precipitation of the transition metal. This has been attributed to the formation of $(Ni(NH_3)_4)^{2+}$ complexes in the presence of excess ammonia [17], which are soluble in a wide range of pH.

The XRD patterns of the oxides are shown in Figure 2. The sample with aluminium only displays sharp reflections belonging to α-Al_2O_3 (JCPDS 10-173). All the lanthanum-aluminium and barium-aluminium oxides incorporating a transition metal show hexaaluminate as the only crystalline phase: $LaAl_{11}O_{18}$ (JCPDS 33-699) and $BaAl_{12}O_{19}$ (JCPDS 26-135). The relative intensity of the reflections varies among the samples, indicating a different degree of crystallinity depending on the transition metal substituted in the structure. The non-substituted La-Al and Ba-Al samples also exhibited characteristic hexaaluminate reflections, but additional $LaAlO_3$ (JCPDS 31-22) and $BaAl_2O_4$ (JCPDS 17-306) phases, respectively, are prominently present. Previous

XRD work by Groppi *et al.* [17,22,23] evidenced both $LaAlO_3$ and $BaAl2O_4$ as intermediate phases in the formation of the hexaaluminate. The increase of the corresponding hexaaluminate reflections was coupled with decrease of the La-Al perovskite and Ba-Al spinel impurities. In the Ba_1-Al_{12} system, $BaAl_2O_4$ was formed at 1170 K, requiring calcination temperatures up to 1670 K for complete depletion of this phase in the pattern and formation of $BaAl_{12}O_{19}$ [22]. Similarly, the $LaAlO_3$ perovskite was visualized at 1273 K in the La_1-Al_{11} system and still coexisted with $LaAl_{11}O_{18}$ upon calcination of the sample at 1573 K [23].

Figure 2 shows that incorporation of a transition metal in the compound leads to the formation of pure hexaaluminate phase upon calcination of the specimen at 1473 K. Using the carbonate route followed by thermal treatment, Groppi *et al.* [23] showed that partial substitution of Al^{3+} by Mn^{2+} and especially Mg^{2+} ions promoted the formation of monophasic lanthanum hexaaluminates by calcination at 1573 K for 10 h through a charge compensation mechanism. Our results make it possible to conclude that the promotion of single-phased hexaaluminates can be generalized to all transition metals investigated (Mn, Fe, Ni). This was previously deduced from studies with materials synthesized through crystallization from the melted precursor to obtain single crystals or via high-temperature solid-state reaction to obtain highly sintered materials [24].

Table 1. Characterization data for the catalysts investigated in this study.

	Metal ratios, mol mol^{-1}								
	Al/A[a]		B/B[b]						
Sample	nominal	in solid	nominal	in solid	Al, wt %	A, wt %	B, wt %	a_0, Å	c_0, Å
Al					51.4				
La-Al	11	11.2			39.8	18.1		5.565[c]	21.91[c]
La-Mn-Al	11	11.1	11	10.6	35.4	16.4	6.8	5.615	22.91
La-Fe-Al	11	10.8	11	10.8	35.6	16.9	6.8	5.598	22.15
La-Ni-Al	11	10.7	11	12.1	36.1	17.4	6.5	5.604	22.11
Ba-Al	11	11.0			40.3	18.6		5.591[d]	22.76[d]
Ba-Mn-Al	11	10.6	11	11.1	36.6	17.5	6.7	5.645	22.74
Ba-Fe-Al	11	10.7	11	10.6	36.5	17.3	7.1	5.615	22.79
Ba-Ni-Al	11	10.6	11	14.6	37.0	17.7	5.5	5.610	22.70

[a] A cation = Ba or La. [b] B cation = Mn, Fe, or Ni. [c] Cell parameters in JCPDS 33-699 ($LaAl_{11}O_{18}$): $a_0 = b_0 = 5.561$ Å and $c_0 = 22.04$ Å. [d] Cell parameters in JCPDS 26-135 ($BaAl_{12}O_{19}$): $a_0 = b_0 = 5.607$ Å and $c_0 = 22.90$ Å.

The cell parameters a_0 and c_0 for the different hexaaluminate samples are reported in Table 1. The calculated values for the La-Al and Ba-Al samples are in very good agreement with those in the corresponding JCPDS cards (see footnote in table). The value of $a_0 = b_0$ in the transition metal containing materials is always higher than that of the non substituted ones. This points out that the larger Mn, Fe, and Ni ions are located in the hexaaluminate structure, replacing smaller Al^{3+} ions. Since Ba^{2+} has a larger ionic radius than La^{3+} (1.49 *vs.* 1.17 Å), the c_0 parameter was higher in the Ba-containing samples, but it was not significantly altered upon substitution by the different transition metals.

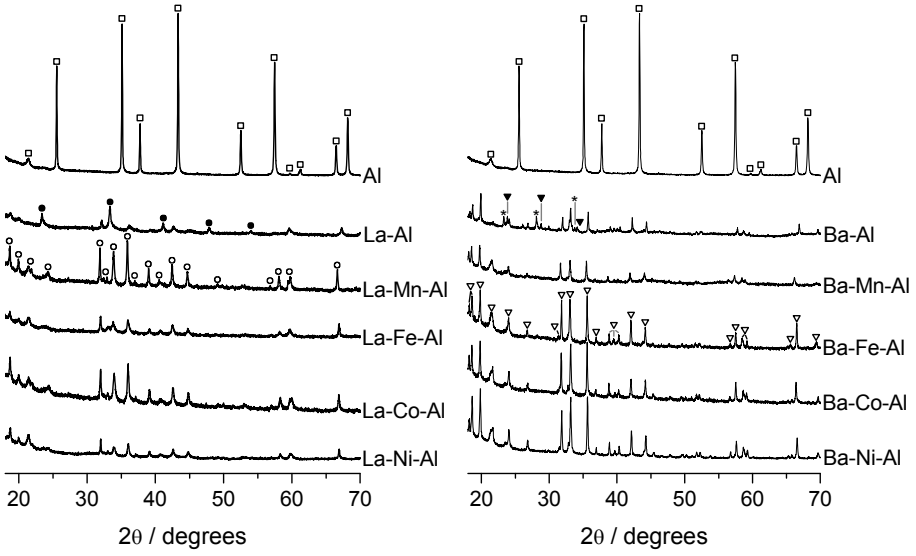

Figure 2. XRD patterns of the calcined samples. Crystalline phases: (□) α-Al_2O_3, (○) $LaAl_{11}O_{18}$, (●) $LaAlO_3$, (▽) $BaAl_{12}O_{19}$, and (▼) $BaAl_2O_4$. Reflections marked with asterisks in the Ba-Al sample were not assigned.

The diffractograms in Figure 2 show less intense and apparently broader reflections in the lanthanum than in the barium hexaaluminates. This can be tentatively related to the high degree of defectivity of the crystal lattice in the lanthanum-containing samples, with magnetoplumbite structure [25], originating scattering diffusion in (00*l*) crystallographic planes and thus leading to broadening of the diffraction lines [26]. The

occurrence of smaller crystals in the lanthanum hexaaluminates could also substantiate this observation.

TEM analyses (Figure 3) evidenced the extensive degree of sintering in the Al sample, resulting in very large α-Al_2O_3 crystals. Distinctively, much smaller crystals are obtained in the lanthanum and barium hexaaluminates, exhibiting the characteristic hexagonal planar morphology. The micrographs do not reveal significant differences in particle size between the two samples. Similar results as exemplified by the Mn-containing samples were obtained with the other transition metals.

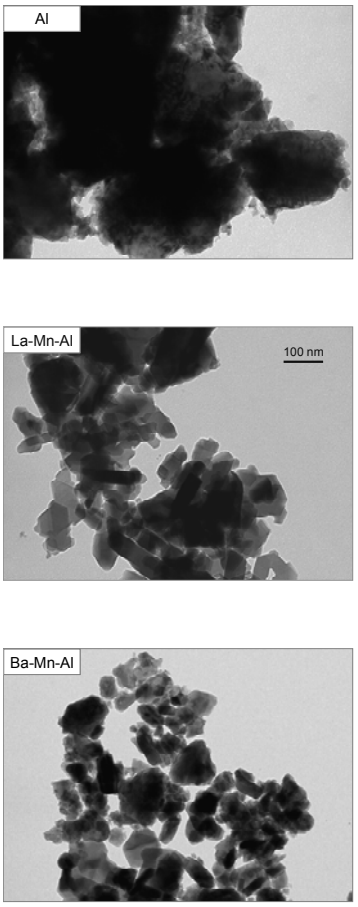

Figure 3. TEM of three representative oxides. The same scale bar applies to all the micrographs.

The specific BET surface areas of the samples are shown in Figure 4. As expected from its high degree of sintering, α-Al_2O_3 presents the lowest degree of porosity

UNIVERSITAT ROVIRA I VIRGILI
HEXAALUIMINATE-TYPE CATALYSTS FOR N2O ABATEMENT
Marta Santiago Redondo
ISBN:978-84-693-8864-8/DL:T.1943-2010

(4 m^2 g^{-1}). Incorporation of barium or lanthanum in the material stabilizes the β-alumina or magnetoplumbite phase, respectively, and reduces the degree of sintering (see TEM in Figure 3). As a consequence, 6-9 times higher surface areas are obtained in the La-Al (35 m^2 g^{-1}) and Ba-Al (25 m^2 g^{-1}) hexaaluminates with respect to α-Al_2O_3. The presence of transition metals leads to a lower surface area of the resulting oxide as compared to the non-substituted samples. For both A cations, the S_{BET} decreases with the B metal in the order Ni > Fe > Mn. The lanthanum-containing samples display a slightly higher surface area than the barium-containing samples, independently of the metal substituted.

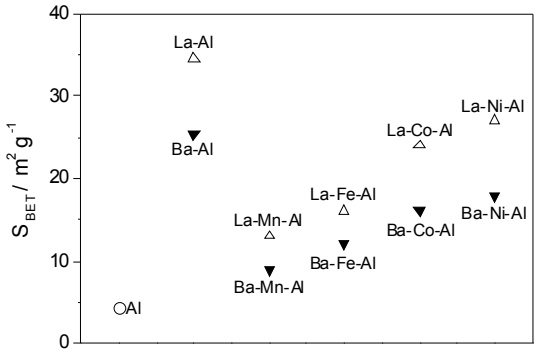

Figure 4. BET surface area of the oxide samples derived from N_2 adsorption measurements.

3.2. Catalytic performance

Temperature-programmed reaction experiments (Figure 5) were used for screening the N_2O decomposition activity of the hexaaluminate catalysts. The activity of the empty quartz reactor wall was also measured. In the absence of catalyst, N_2O is decomposed above 1050 K, reaching a conversion of *ca.* 75% at 1225 K. The conversion *vs.* temperature curves reveal that the Fe-substituted hexaaluminates were the most active catalysts, closely followed by the Mn-substituted hexaaluminates. Over these systems, N_2O conversion starts at 800 K and reaches practically 100% at 1050 K, with T_{50} (temperature for 50% N_2O conversion) around 900-925 K. The catalytic performance was not influenced by the A cation in the hexaaluminate, that is, La or Ba. The Ni-substituted hexaaluminates were considerably less active, exhibiting very similar behaviour to the non substituted hexaaluminates. The T_{50} over the latter group

of catalysts is 1025-1075 K. For this pair of samples, the Ba-containing system appears to be slightly more active that the La-containing system. As expected, α-Al_2O_3 presents very poor catalytic performance in the reaction (T_{50} = 1150 K), approaching the conversion profile obtained with the empty quartz reactor (T_{50} = 1180 K). The fact that the iron-substituted hexaaluminates were the most active catalysts was a priori not expected, attending to the established activity order of transition metals in different supports and oxide matrices for direct N_2O decomposition. As reviewed by Kapteijn *et al.* [27], Fe is a considerably less active transition metal as compared to Mn or Ni in pure oxides, solid solutions of transition metals in inert matrices, and mixed oxides such as perovskites and spinels. Our results indicate the high relative activity of iron based systems when the transition metal is located in a hexaaluminate matrix. More detailed characterization studies of the hexaaluminate samples are required to explain the activity order in Figure 5.

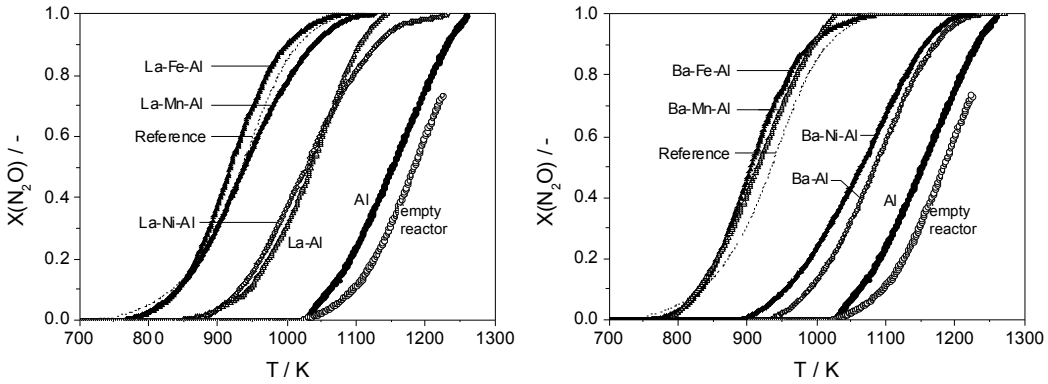

Figure 5. N_2O conversion *vs.* temperature in TPR experiments. Conditions: feed of 5000 ppm N_2O in He; P = 1 bar; WHSV= 30,000 ml g^{-1} h^{-1}; heating rate 5 K min^{-1}.

The steady-state N_2O conversion *vs.* temperature over the most active catalysts is shown in Figure 6. In N_2O+He feed (open symbols), both barium-iron-aluminium and barium-manganese aluminium hexaaluminates display significant N_2O conversion above 800 K, being >90% above 1025 K, in good agreement with TPR results. However, the T_{50} over iron-containing catalysts was *ca.* 50 K lower than that over manganese-containing catalyst (895 *vs.* 950 K). This is attributed to the higher apparent activation

energy over barium-iron-aluminium hexaaluminate (100 kJ mol^{-1}) than over barium-manganese-aluminium hexaaluminate (85 kJ mol^{-1}). These values were estimated around the inflection (50% conversion) of the steady-state conversion *vs.* temperature curves by assuming a plug-flow model and first order reaction in N_2O. In order to establish the potential of hexaaluminates for high-temperature N_2O abatement in industrial sources, the catalytic performance was evaluated under relevant process conditions of temperature, feed composition, and space velocity. In ammonia burners, ammonia-air mixtures (typically 10 vol.% NH_3, NH_3:O_2 = 1:2) react on PGM (platinum group metals) gauzes at 1173 K, leading to NO selectivities of 95-97%. The outlet gas contains small N_2O amounts (typically 1500 ppm), unreacted O_2, and the main reaction products NO and H_2O. The N_2O conversion profile in N_2O+NO+O_2+H_2O+He ("all" in Figure 6, solid symbols) is shifted to higher temperature with respect to the model N_2O+He feed due to inhibition by the additional components in the mixture. It can be seen that the Ba-Fe-Al hexaaluminate is a little more sensitive to inhibition than Ba-Mn-Al hexaaluminate. In the simulated mixture, total N_2O conversion was attained around 1100 K, that is, somewhat lower than the gas temperature at the outlet of the Pt-Rh gauzes in the ammonia burner (in the range of 1123-1173 K) [3].

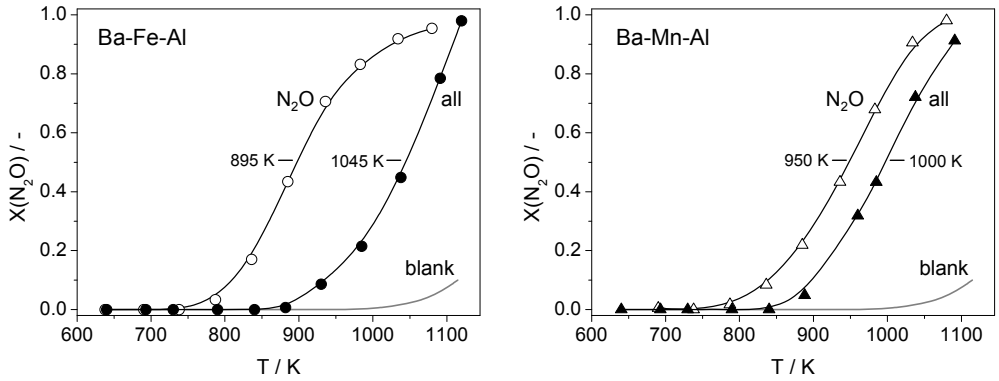

Figure 6. Steady-state N_2O conversion *vs.* temperature over barium-iron-aluminium and barium-manganese-aluminium hexaaluminates in N_2O+He (N_2O; open symbols) and N_2O+O_2+NO+H_2O+He (all; solid symbols). Conditions: feed of 1500 ppm N_2O, 10 vol.% O_2, 1.5 vol.% NO, and 10 vol.% H_2O, balance in He; P = 1 bar; WHSV = 30,000 ml g^{-1} h^{-1}.

Figure 7 illustrates the N_2O conversion *vs.* temperature in the different feed mixtures over the Ba-Fe-Al hexaaluminate. Ba-Fe-Al hexaaluminate displays significant N_2O conversion in N_2O+He feed above 750 K, being 90% above 1025 K. NO has no effect on the N_2O decomposition performance. The presence of O_2 inhibits the N_2O decomposition, shifting the conversion profile by *ca.* 25-50 K to higher temperatures. H_2O also inhibits the reaction, presenting a very similar behaviour to that of O_2 below 900 K and approaching the conversion with the N_2O+He mixture around 973 K. The negative influence of O_2 and H_2O in the reaction can be attributed to competitive adsorption over active N_2O decomposition sites in the catalyst [27]. Severe inhibition

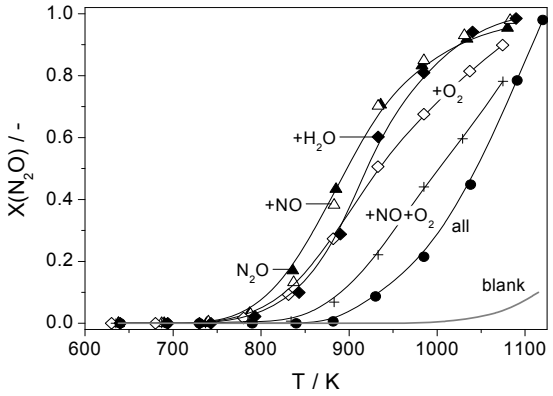

Figure 7. N_2O conversion *vs.* T over Ba-Fe-Al hexaaluminate in feed mixtures with N_2O and additional components at the outlet of the Pt-Rh gauzes in ammonia burners. Conditions as described in text.

of the catalytic activity was experienced in N_2O+NO+O_2 mixtures as compared with the individual components. This result suggests the formation of stable nitrate-type species on the catalyst surface, probably initiated by NO_2. Very similar results to those shown for Ba-Fe-Al hexaaluminate in Figure 7 were obtained over the Mn-substituted hexaaluminates.

In order to assess the short-term stability of the catalysts, the N_2O conversion was monitored with time in the mixture containing all the gases. The temperature was set so as to operate at intermediate degrees of N_2O conversion and visualize any sign of deactivation more clearly. As illustrated in Figure 8, the N_2O conversion at 1073 K (*ca.* 50%) was practically constant during 60 h on-stream over Ba-Fe-Al hexaaluminate. This result is promising, since average high-temperature catalysts (>973 K) show rapid deactivation in the first few hours of operation. In the activity tests with simulated mixtures, attention was also paid to analyzing any possible conversion of NO over the catalyst. This is highly detrimental, since the ability of a catalyst to assist NO decomposition (the desired product of ammonia oxidation) would annihilate any prospect of this family of materials assisting process-gas N_2O abatement. This result highlights the superior stability of this family of materials, a key property for high-temperature catalytic applications. We have shown that metal-

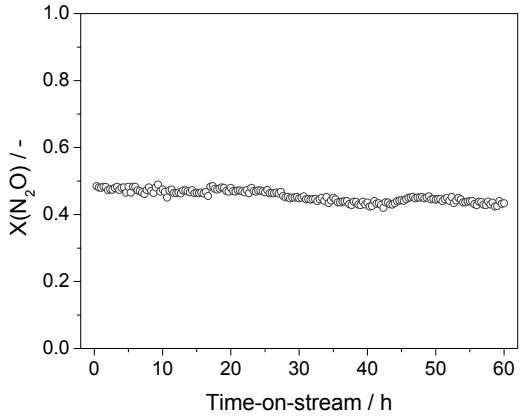

Figure 8. N_2O conversion *vs.* time-on-stream over barium-iron-aluminium hexaaluminate at 1073 K. Conditions were as described in the caption of Figure 6 for the multicomponent gas mixture.

substituted hexaaluminates fulfill the rigorous requirements of activity and stability to be effectively applied in high-temperature (process-gas) catalytic N_2O decomposition. This result highlights the superior stability of this family of materials, a key property for high-temperature catalytic applications. Our results enable us to conclude that the

degree of the NO conversion to N_2 was below the detection limit of the analytical method (<1%), evidence of the selective nature of the metal-substituted hexaaluminates for N_2O decomposition.

4. Conclusions

We have shown that metal-substituted hexaaluminates fulfill the rigorous requirements of activity and stability to be effectively applied in high-temperature (process-gas) catalytic N_2O decomposition. This has been demonstrated for a mixture simulating the conditions at the outlet of the noble metal gauzes in ammonia burners of nitric acid and caprolactam production plants, where N_2O is formed as byproduct. These are currently the most important anthropogenic sources of this powerful greenhouse gas in the chemical industry. The Fe- and Mn-substituted lanthanum and barium hexaaluminates can be considered as a promising alternative to the recently commercialized Co_2AlO_4/CeO_2 and $La_{0.8}Ce_{0.2}CoO_3$ systems. First, the chemical stability of hexaaluminates is superior to that of spinel- and perovskite-based mixed oxides. Besides, the cost of the hexaaluminate systems can be anticipated as highly competitive because inexpensive active phases are used within an alumina-based matrix, and the applied coprecipitation method for catalyst preparation is relatively simple and scalable.

References

[1] P.J. Crutzen, J. Geophys. Res. 76 (1971) 7311.
[2] L. Donner, Ramanathan, J. Atmos. Sci. 37 (1980) 119.
[3] J. Pérez-Ramírez, F. Kapteijn, K. Schöffel, J. Moulijn, Appl. Catal. B 44 (2003) 117 and references therein.
[4] R.A. Reimer, C.S. Slaten, M. Seapan, M.W. Lower, P.E. Tomlinson, Environ. Prog. 13 (1994) 134.
[5] The Kyoto Protocol, United Nations Framework Convention on Climate Change, COP3 (www.unfccc.int), 11 December 1997, Kyoto, Japan.
[6] M. Groves, R. Maurer, M. Schwefer, R. Siefert, Proceedings of the Nitrogen Conference, Vienna, Austria, 2006; pp 121.
[7] V. Schumacher, G. Buerger, T. Fetzer, M. Baier, M. Hesse (BASF). Method for the catalytic decomposition of N_2O. WO9955621, 1999.
[8] M. Baier, T. Fetzer, O. Hofstadt, M. Hesse, G. Buerger, K. Harth, V. Schumacher, H. Wistuba, B. Otto (BASF). High temperature stabile catalsyts for decomposing N_2O. WO0023176, 2000.

[9] S.A. Axon, D.R. Coupland, B.T. Horner, J. Ridland, I. C. Wishart (Johnson Matthey). Improved catalyst charge design. WO04096702A2, 2004.

[10] S.A. Axon, D.R. Coupland, J.R. Foy, J. Ridland, I. C. Wishart (Johnson Matthey). Ammonia oxidation process. WO040967-03A2, 2004.

[11] Ø. Nirise, K. Schöffel, D. Waller, D. Øvrebø (Yara International). Catalyst for decomposing nitrous oxide and method for performing processes comprising formation of nitrous oxide. WO0202230, 2002.

[12] J. Pérez-Ramírez, F. Kapteijn, G. Mul, J.A. Moulijn, Chem. Commun. (2001) 693

[13] M. Machida, K. Eguchi, H. Arai, J. Catal. 103 (1987) 385.

[14] M.F.M. Zwinkels, S.G. Järås, P.G. Menon, T.A. Griffin, Catal. Rev.s Sci. Eng. 35 (1993) 319.

[15] M. Machida, K. Eguchi, H. Arai, J. Catal. 120 (1989) 377.

[16] G. Groppi, M. Belloto, C. Cristiani, P. Forzatti, P.L. Villa, Appl. Catal. A 104 (1993) 101.

[17] L. Lietti, C. Cristiani, G. Groppi, P. Forzatti, Catal. Today 59 (2000), 191.

[18] P. Artizzu-Duart, J.M. Millet, N. Guilhaume, E. Garbowski, M. Primet, Catal. Today 59 (2000) 163.

[19] M. Machida, K. Eguchi, H. Arai, J. Am. Ceram. Soc. 71 (1988) 1142.

[20] M. Santiago, M.S. Yalfani, J. Pérez-Ramírez, J. Mater. Chem. 16 (2006) 2886.

[21] S. Brunauer, P.H. Emmett, E. Teller J. Am. Chem. Soc. 60 (1938) 309.

[22] G. Groppi, M. Belloto, C. Cristiani, P. Forzatti, J. Mater. Sci. 29 (1994) 3441.

[23] G.Groppi, C. Cristiani, P. Forzatti, Appl. Catal. B 35 (2001) 137.

[24] F. Laville, A.M. Lejus, Cryst. Growth 63 (1983) 426.

[25] N. Iyi, Z. Inoue, S. Takekawa, S. Kimura, J. Solid State Chem. 54 (1984) 70.

[26] J.G. Park, A.N. Cormack, J. Solid State Chem. 130 (1997) 199.

[27] F. Kapteijn, J. Rodríguez-Mirasol, J.A. Moulijn, Appl. Catal. B 9 (1996) 25 and references therein.

UNIVERSITAT ROVIRA I VIRGILI
HEXAALUIMINATE-TYPE CATALYSTS FOR N2O ABATEMENT
Marta Santiago Redondo
ISBN:978-84-693-8864-8/DL:T.1943-2010

Chapter 4

Carbon-templated hexaaluminates with enhanced surface area and catalytic performance

Carbon templating was used to synthesize high-surface area $LaFeAl_{11}O_{19}$ hexaaluminates leading to improved catalytic performance. The oxide precursor-template composites were prepared by impregnation, complexation with citric acid, and coprecipitation routes varying the amounts of acetylene black incorporated. Calcination in static air at 1473 K led to single-phased hexaaluminates. The samples were characterized at different stages of the synthetic protocol by ICP-OES, *in situ* and *ex situ* XRD, TEM, N_2 adsorption, He pycnometry, TGA, H_2-TPR, and XPS. The templating effect of carbon originates fine oxide particles. Consequently, the specific surface area of the non-templated hexaaluminates (1-11 $m^2\ g^{-1}$ depending on the preparation method) increased up to a factor of 25 upon incorporation of carbon in the synthesis. The stabilization of small particles occurs despite the temperature difference between the elimination of carbon (973 K) and the attainment of the hexaaluminate phase above 1373 K. The morphology of the oxide obtained upon carbon removal determines the textural properties of the hexaaluminate particles. Our results demonstrate that the confined space synthesis is not exclusively responsible for small oxide particles. The stabilization of small crystallites on the carbon surface in the composite and breakage of the oxide layer caused by template combustion are key aspects for attaining finely dispersed particles when the carbon is macroporous. The enhanced catalytic activity and time-on-stream stability of the templated hexaaluminates was demonstrated in the direct N_2O decomposition using model and simulated feed mixtures. In this application, a quasi-linear relation between the reaction rate and the specific surface area of the samples was obtained. Characterization by H_2-TPR and XPS indicated that the nature of iron in $LaFeAl_{11}O_{19}$ was not altered by carbon incorporation.

This chapter is based on the following publication:
M. Santiago, J.C. Groen, J. Pérez-Ramírez, J. Catal. 257 (2008) 152.

1. Introduction

Suitable catalysts for high-temperature applications should accomplish defined targets associated with activity and selectivity. However, only those materials additionally exhibiting extraordinary chemical and mechanical stability are ultimately implemented in industry. Metal-substituted hexaaluminates are attractive catalysts and catalyst supports for high-temperature applications, including natural gas combustion in power turbines [1-7], (partial) oxidation of hydrocarbons [8,9], CO_2-reforming of methane [10], and process-gas N_2O decomposition [11]. These materials exhibit stable phase composition up to 1873 K and remarkable resistance to sintering and thermal shock. These unique properties are associated with their structure, consisting of alternate stacking along the c-axis of γ-Al_2O_3 spinel blocks and mirror planes in which large alkaline (K^+), alkaline-earth (Ba^{2+}, Ca^{2+}, Sr^{2+}), or rare-earth (La^{3+}) cations are located [12]. Substitution of transition metal ions in Al^{3+} positions of the spinel blocks creates redox active centers in the structure with minimal effect on the sintering resistance of the material [1,3].

Hexaaluminate precursors are typically prepared by sol-gel synthesis using metal alkoxides or organometallic compounds [1,2,7,9] or coprecipitation of metal nitrate solutions with ammonium carbonate [5,6,11,13]. Calcination of the material above 1473 K results in single-phased metal-substituted hexaaluminates with specific surface areas in the typical range of 5-15 $m^2\ g^{-1}$ [14]. Increasing the surface area of hexaaluminates by novel or modified synthesis routes is of interest for prospective catalytic use. In the high temperature regime, mass transfer usually plays an important role in the overall process and materials with large surface-to-volume ratios are advantageous. Zarur and Ying [15] introduced a reverse microemulsion-mediated sol-gel method to synthesize Ba-hexaaluminate nanoparticles with surface areas ranging from 40 to 160 $m^2\ g^{-1}$. However, this route is not amenable to industrial implementation due to economic, safety, and scalability constraints. Metal alkoxides are harmful and expensive and their hydrolysis should be practiced under extremely controlled conditions (moisture and oxygen-free environment). Besides, relatively sophisticated freeze and supercritical drying techniques are necessary for nanoparticle recovery. Alluding to these limitations, Teng *et al.* [16] developed a reverse

microemulsion route using inorganic salts and drying in supercritical ethanol, obtaining $BaMnAl_{11}O_{19}$ with 70 $m^2\ g^{-1}$.

Alternatively, templating approaches can be used to synthesize high-surface area materials with control over their structural and textural properties on length scales between nanometers and micrometers [17-19]. The concept of templating was introduced in the zeolite field and was extended to ordered mesoporous materials, where periodic pore systems are created by occlusion of molecular or supramolecular units in the resulting solid (referred to as 'endotemplating'). A more recent approach is 'exotemplating' also termed 'hard templating,' 'confined space synthesis,' or 'compartment solidification' [17]. Exotemplates are extended porous structures providing the space where a divided solid can form. Carbon is the ideal exotemplate attending to its easy removal by combustion, versatile porous characteristics, and relatively low cost. Carbon templating has been applied to synthesize mesoporous zeolite crystals and nanocrystalline zeolites [20,21] as well as high surface area oxides [22]. In the latter group, single metal oxides (*e.g.*, MgO, Fe_2O_3, Cr_2O_3, TiO_2), spinels (*e.g.*, $CoCr_2O_4$, $NiAl_2O_4$), and perovskites (*e.g.*, $LaFeO_3$) with 4-20 times higher surface area than the non-templated counterparts have been obtained. However, most of these studies merely report increased surface area, and only exceptionally evaluate the effect of the created porosity on the catalytic performance [23].

The typical preparation of oxides by templating involves the impregnation of carbon with concentrated solutions of the metal cations followed by drying and thermal treatment [17,22]. To the best of our knowledge, other strategies to prepare the oxide precursor-carbon composites have not been widely explored. In addition, it is not straightforward to predict the effectiveness of carbon templating for synthesizing oxides requiring extremely high calcination temperatures, such as hexaaluminates. Work with oxides was restricted to perovskites requiring calcination temperatures up to 1073 K [22]. However, the radically different temperature between the combustion of carbon (typically 973 K) and the hexaaluminate formation (typically 1473 K) could lead to severe sintering of the intermediate oxidic phase once the carbon is removed, probably abrogating the template effect for achieving enhanced surface area and ultimately improved catalytic activity.

Herein we demonstrate the carbon templating route to prepare single-phased $LaFeAl_{11}O_{19}$ hexaaluminates (magnetoplumbite structure) with significantly higher surface area than the nontemplated counterparts. Different methods to prepare the precursors have been practiced, incorporating variable carbon amounts. The materials were characterized by ICP-OES, *in situ* and *ex situ* XRD, TEM, N_2 adsorption, He pycnometry, TGA, H_2-TPR, and XPS. Based on these analyses, aspects of the templating mechanism are discussed. The templated hexaaluminates possess clear benefits in terms of catalytic performance compared to the carbon-free hexaaluminates, as illustrated by their application in direct N_2O decomposition using model and simulated mixtures. In our previous study [11], Fe-substituted hexaaluminates proved suitable catalysts for process-gas N_2O abatement in ammonia burners of nitric acid and caprolactam production. For this high-temperature application (1073-1173 K, wet oxidizing conditions), materials combining high catalytic activity and excellent chemical stability are required [24].

2. Experimental

2.1. Catalyst preparation

Hexaaluminates with the formula $LaFeAl_{11}O_{19}$ were obtained by calcination of differently prepared precursors. As starting point, an aqueous solution of the corresponding metal nitrates, *i.e.* $La(NO_3)_3{\cdot}6H_2O$, $Fe(NO_3)_3{\cdot}9H_2O$, and $Al(NO_3)_3{\cdot}9H_2O$ (Aldrich, purity >98%), with 0.1 M La, 0.1 M Fe, and 1.1 M Al was prepared. Carbon black (acetylene, 50% compressed) from Alfa Aesar (product code 39724) was incorporated in the synthesis as the template. The carbon has a nominal surface area of 80 $m^2\ g^{-1}$. Previous to use, the as-received sample was dried at 378 K for 24 h. The carbon content given in the below recipes and in the code of the samples along the manuscript is expressed as weight percent with respect to the total weight of carbon and metal nitrates.

Impregnation

The precursor-template composite was prepared by a conventional impregnation method described elsewhere [22]. A fixed amount of carbon (40 wt.% based on the

total weight of carbon and metal nitrates) was impregnated with the aqueous solution of metal cations and mixed well with a spatula. This led to the formation of crumbly solid particles, which were dried at 363 K for 12 h and then calcined in static air at 1473 K for 1 h using a ramp of 5 K min^{-1}. The non-templated hexaaluminate counterpart was prepared using a solid-state route, *i.e.* mechanically mixing appropriate amounts of the metal nitrate salts followed by calcination according to the above program.

Complexation

A soft-chemical route equivalent to that described in [25] was carried out by mixing the solution of metal nitrates with citric acid at room temperature using a molar ratio of total cations to the complexant of 3 until a clear solution was obtained. Nominal carbon contents in the range 5-50 wt.% were added to the resulting solution. Subsequently, the temperature of the resulting slurry was increased from 298 K to 433 K in static air using a heating rate of 0.7 K min^{-1} and held for 12 h. The dried composite was crushed in an agate mortar followed by thermal treatment according to the program: heating from 433 K to 733 K at 5 K min^{-1} and kept isothermal for 5 h, and finally heating to 1473 K at 5 K min^{-1} for 1 h. The corresponding non-templated sample was prepared according to the same procedure without adding carbon to the solution of metal nitrates and citric acid.

Coprecipitation

A certain amount of carbon (nominal content of 25 and 50 wt.%) was first impregnated by the solution of metal nitrates. Subsequently, an aqueous solution of 2 M $(NH_4)_2CO_3$ was added drop-wise under mechanical stirring (500 rpm) until pH 8.0 was reached. The slurry was aged at 333 K for 1 h, filtered, washed with deionised water, dried at 378 K for 12 h, and calcined in static air at 1473 K for 1 h using a heating rate of 5 K min^{-1}. The non-templated sample was prepared using the same coprecipitation method without the carbon impregnation step.

2.2. Catalyst characterization

The chemical composition was determined by Inductive Coupled Plasma-Optical Emission Spectroscopy (ICP-OES) (Perkin-Elmer Optima 3200RL (radial)). Prior to the analysis, the solids were treated using an alkaline fusion method with NaOH and Na_2O_2, followed by dilution with HCl.

Ex situ powder X-ray diffraction (XRD) patterns were acquired in a Bruker AXS D8 Advance diffractometer equipped with a Cu tube, a Ge(111) incident beam monochromator (λ = 0.1541 nm), and a Vantec-1 PSD. Data were collected in the 2θ range 10-70° with an angular step size of 0.02° and a counting time of 4 s per step.

In situ XRD during thermal decomposition of the precursors in air flow (100 ml STPmin^{-1}) was studied in a Bruker AXS D5005 diffractometer equipped with a Bruker AXS MRI high-temperature chamber and a diffracted beam graphite monochromator using CuKα radiation. A thin layer of sample (*ca.* 30 mg) was mounted on the Pt90-Rh10 heater strip inside the chamber by placing a few droplets of a suspension of finely ground sample in ethanol on the strip followed by drying under ambient conditions. Data were collected in the 2θ range 10-70° with an angular step size of 0.05° and a counting time of 0.5 s per step. Patterns were recorded at intervals of 50 K in the range 323-1673 K after 2 min equilibration at each temperature. The heating rate was 60 K min^{-1}. The sample was directly heated by the heater strip, whose temperature can be controlled within 2 K.

Transmission Electron Microscopy (TEM) was carried out in a JEOL JEM-1011 microscope operated at 100 kV and equipped with a SIS Megaview III CCD camera. A few droplets of the sample suspended in ethanol were placed on a carbon-coated copper grid followed by evaporation at ambient conditions.

The skeleton density of selected solids was measured by helium pycnometry at 295 K in a Quantachrome Pentapycnometer. Prior to the measurement, the sample was dried at 393 K for 12 h.

Nitrogen adsorption-desorption isotherms at 77 K were measured on a Quantachrome Autosorb 6B analyzer. Before analysis, the samples were degassed in vacuum at 393 K for 16 h. The BET method [26] was applied to calculate the total surface area and the *t*-plot method [27] was used to discriminate between micro and

mesoporosity. The BJH model [28] applied to the adsorption branch of the isotherm provides information on the mesopore size distribution.

Thermal analysis was carried out in a Mettler Toledo TGA/SDTA 851e microbalance equipped with a 34-positions sample carrousel. The solid (3 mg) was placed in 70 µl-alumina crucibles without dilution. Analyses were performed in dry air flow (50 cm^3 STP min^{-1}), ramping the temperature from 298 to 1173 K with a heating rate of 5 $Kmin^{-1}$.

Temperature-programmed reduction with hydrogen (H_2-TPR) was carried out in a Thermo TPDRO 1100 system equipped with a thermal conductivity detector (TCD). The catalyst sample (150 mg) was loaded in the quartz micro-reactor (11 mm i.d.), pretreated in N_2 (20 ml STP min^{-1}) at 673 K for 1 h, and cooled to 323 K in the same atmosphere. The analysis was done in a high purity mixture of 5 vol.% H_2 in N_2 (20 ml STP min^{-1}), ramping the temperature from 323 to 1373 K at 10 K min^{-1}.

X-ray photoelectron spectroscopy (XPS) measurements were obtained using a PHI 5500 Multitechnique System from Physical Electronics equipped with monochromatic AlKα radiation at 1486.6 eV as the X-ray source, a nine-channeltron detection system, and a hemispheric electron analyzer operating at a constant pass energy of 23 eV and a resolution energy of 0.1 eV. The measurements were carried out in a UHV chamber, where the pressure was maintained between 5×10^{-9} and 2×10^{-8} Torr. The binding energies were referenced to the C 1s line at 284.8 eV.

2.3. Activity tests

Direct N_2O decomposition was studied in a quartz fixed-bed reactor (10 mm i.d.) using 200 mg of sample (sieve fraction 200-300 µm), a total pressure of 1 bar, and a weight-hourly space velocity (WHSV) of 60,000 ml g^{-1} h^{-1}. Isothermal tests were conducted in the range 573-1123 K, typically using a model mixture containing 1.5 mbar N_2O in He. Selected catalysts were additionally tested at 923 K in a feed mixture containing 1.5 mbar N_2O, 10 mbar NO, 100 mbar O_2, 100 mbar H_2O in He, *i.e.* simulating the gas composition at the outlet of the Pt-Rh gauzes in ammonia burners, where these catalytic systems can be potentially used [11]. Generally, 30 min after a change of conditions, the conversion levels were constant and considered as steady state. Prior to the tests, the catalysts were pretreated at 673 K in the feed mixture for

1 h. The reactant and product gases were analyzed by gas chromatography (SRA Instruments Micro-GC 3000) equipped with HP-PlotQ and HP-Plot MoleSieve columns and a TCD detector.

3. Results and discussion

The sample codes along the manuscript contain the initials of the metals in the hexaaluminate (LFA for La, Fe, and Al), the synthesis method (IM: impregnation, CA: complexation with citric acid, and BC: batch coprecipitation), and the nominal carbon content in the composite. For example, LFA-BC-0 and LFA-BC-25 denote the samples prepared by batch coprecipitation without carbon or with 25 wt.% carbon, respectively.

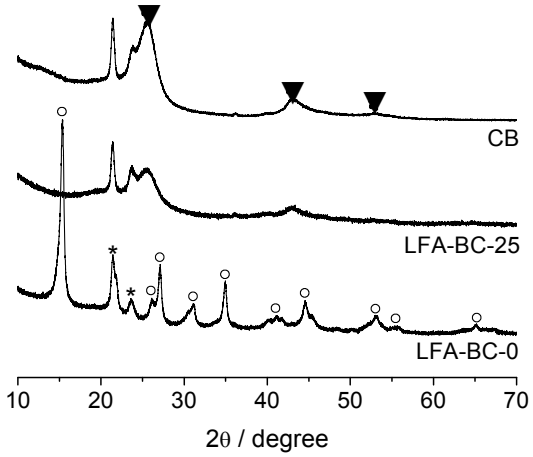

Figure 1. *Ex situ* X-ray diffraction patterns of the hexaaluminate precursors prepared by coprecipitation in the absence (LFA-BC-0) or presence (LFA-BC-25) of carbon. The pattern of carbon (CB) is included for comparative purposes. Phases: (○) AACH, JCPDS 42-250; (▼) carbon, JCPDS 26-1080. The reflections marked by asterisk are due to the sample holder.

3.1. Precursors

The precursors prepared with and without template were characterized by XRD (crystalline structure), TEM (morphology), N_2 adsorption-desorption at 77 K (porosity), and He pycnometry (density). Specifically, we elaborate here on the precursor and

UNIVERSITAT ROVIRA I VIRGILI
HEXAALUIMINATE-TYPE CATALYSTS FOR N2O ABATEMENT
Marta Santiago Redondo
ISBN:978-84-693-8864-8/DL:T.1943-2010

precursor-carbon composite synthesized by coprecipitation. The sample prepared in the absence of carbon (LFA-BC-0) presents characteristic reflections of ammonium aluminium carbonate hydroxide (AACH, $NH_4Al(OH)_2CO_3$) as the only crystalline phase (Figure 1). As shown by transmission electron microscopy, the specimen consists of small irregular particles having a size distribution in the range 5-15 nm (Figure 2, middle). The nitrogen isotherm of LFA-BC-0 (Figure 3, open circles) evidences high uptake at $p/p_0 < 0.1$, indicative of a mostly microporous solid. As shown in Table 1, application of the *t*-plot method resulted in a micropore volume of 0.10 $cm^3\ g^{-1}$ and a mesopore surface area of 80 $m^2\ g^{-1}$, while the BET method estimated a much higher surface area (307 $m^2\ g^{-1}$) due to the microporosity.

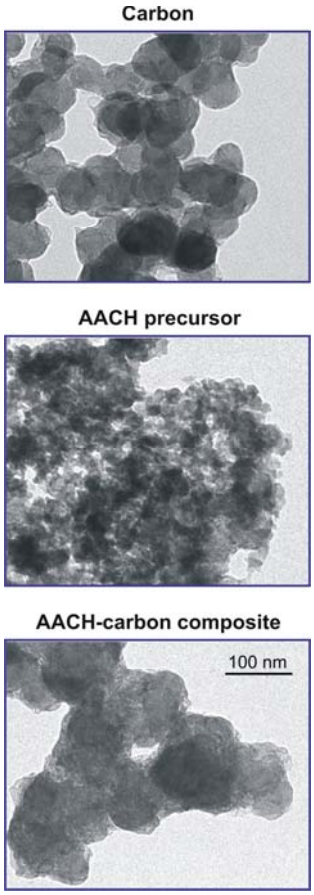

Figure 2. Transmission electron micrographs of carbon (CB), precursor (LFA-BC-0), and precursor-carbon composite (LFA-BC-25). The scale applies to all the micrographs.

UNIVERSITAT ROVIRA I VIRGILI
HEXAALUIMINATE-TYPE CATALYSTS FOR N2O ABATEMENT
Marta Santiago Redondo
ISBN:978-84-693-8864-8/DL:T.1943-2010

Strikingly, none of the AACH diffraction lines in the XRD pattern of LFA-BC-0 were present in the LFA-BC-25 composite. The latter sample only exhibits the background pattern corresponding to the carbon (Figure 1). In a similar manner, Schwickardi *et al.* [22] generally did not detect any crystalline phase upon impregnation of metal nitrates on activated carbon, which was attributed to the formation of small metal nitrate particles confined in the pore system of the template. The occurrence of XRD-invisible AACH crystallites, *i.e.* in the low nm-range, could indeed explain the absence of diffraction lines in LFA-BC-25. However, the formation of an amorphous phase distinct from AACH when the coprecipitation was conducted in the presence of carbon cannot be ruled out. In line with X-ray diffraction, transmission electron microscopy demonstrates the radically different morphology of the non-templated and templated precursors. In the composite (Figure 2, bottom), the hexaaluminate precursor is deposited onto the carbon particles.

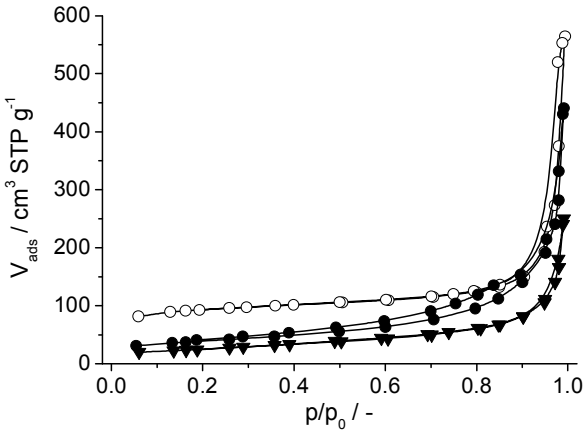

Figure 3. Nitrogen isotherms at 77 K of (▼) carbon (CB), (○) precursor (LFA-BC-0), and (●) precursor-carbon composite (LFA-BC-25).

The carbon black consists of spherical particles with an average size of 70 nm (Figure 2, top). The size of the agglomerates increases substantially in the composite (around 100 nm), implying the coating of the carbon particles by the hexaaluminate precursor during the coprecipitation step.

The N_2 isotherm of the carbon black (Figure 3, inverted triangles) is of type II according to IUPAC nomenclature [29], implying non-porous or macroporous properties. The BET surface area (80 $m^2\ g^{-1}$) results from textural porosity, *i.e.* surface roughness of the particles and interparticle voidage. The coating of the carbon particle by the precipitate induces mesoporous properties by partial filling of the interparticle space. The development of mesoporosity can be concluded from the uptake in the isotherm of LFA-BC-25 at intermediate relative pressures (Figure 3, solid circles) and the textural parameters in Table 1. Interestingly, the composite has no microporosity, in contrast with LFA-BC-0, which is predominantly microporous. This implies that the morphology and texture of the precursor phase in the non-templated and templated samples presents marked differences, although it does not necessarily imply that different phases are obtained. Camblor *et al.* [30] previously demonstrated that zeolite nanocrystals present a distinct lower microporosity or even absence of microporosity as the crystal size decreases into the lower nm-range. This reasoning could apply to our system, *i.e.* the absence of microporosity in the templated sample being attributed to the small crystal size of the precursor species. In addition, the presence of small crystallites can also explain the higher mesopore surface area of 137 $m^2\ g^{-1}$ in the composite as compared to 80 $m^2\ g^{-1}$ in LFA-BC-0. The precursors were also characterized by He pycnometry. The skeleton density of the AACH precursor in LFA-BC-0 (2.53 $cm^3\ g^{-1}$) was slightly higher than that of carbon black (2.15 $cm^3\ g^{-1}$), and as expected the LFABC- 25 composite had an intermediate value (2.34 $cm^3\ g^{-1}$).

Table 1. Textural properties of selected samples.

Sample	Treatment	V_{pore} ($cm^3\ g^{-1}$)	V_{micro} [a] ($cm^3\ g^{-1}$)	S_{meso} [a] ($m^2\ g^{-1}$)	S_{BET} [b] ($m^2\ g^{-1}$)
LFA-BC-0	Precursor	0.58	0.10	80	307
	Calcined at 973 K	0.70	0.08	112	266
	Calcined at 1473 K	0.06	0	11	11
LFA-BC-25	Precursor-carbon composite	0.43	0	137	137
	Calcined at 973 K	0.77	0.01	165	190
	Calcined at 1473 K	0.10	0	32	32
BC	Carbon	0.27	0	80	80

[a] *t*-plot method.
[b] BET method.

UNIVERSITAT ROVIRA I VIRGILI
HEXAALUIMINATE-TYPE CATALYSTS FOR N2O ABATEMENT
Marta Santiago Redondo
ISBN:978-84-693-8864-8/DL:T.1943-2010

3.2. Thermal activation

The thermogravimetric profile of LFA-BC-0 in air shows a one step weight loss in the range 420-500 K (Figure 4, top), which is assigned to the decomposition of the AACH phase [13,31]. The transition temperature was determined at 477 K from the derivative of the weight loss (Figure 4, bottom). The total weight loss of the sample was slightly above 50%. The combustion of pure carbon black occurs at much higher temperature, starting at 1000 K and being completed at 1200 K (transition at 1125 K). The LFA-BC-25 composite shows a two-step decomposition pattern with a total weight loss of *ca.* 80%. The first weight loss occurs at 477 K, *i.e.* exactly the same temperature as in the non-templated sample. This suggests the occurrence of the same AACH phase

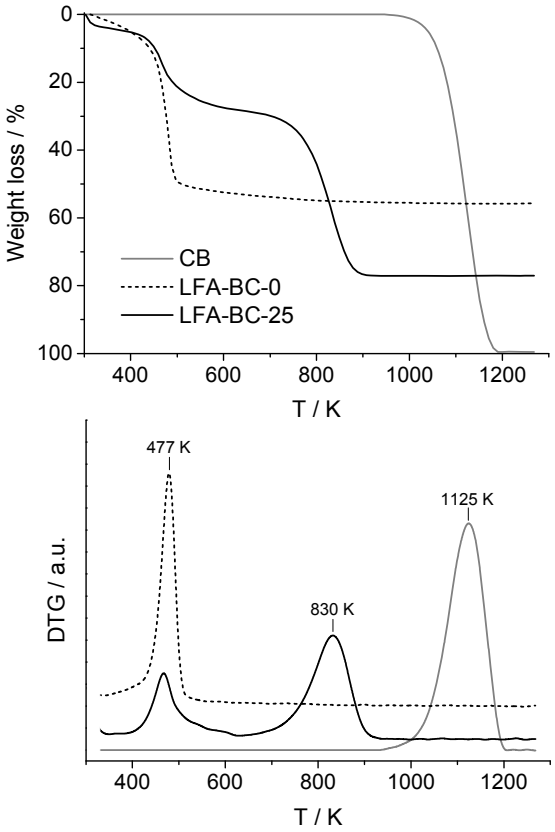

Figure 4. Thermogravimetric profiles (top) and the resulting derivative curves (bottom) of carbon (CB), precursor (LFA-BC-0), and precursor-carbon composite (LFA-BC-25).

in both precursors, *i.e.* the presence of carbon in the synthesis does not alter the chemical nature of the precipitate. On this basis, we put forward that the invisibility of AACH reflections in the XRD pattern of LFABC- 25 in Figure 1 and the absence of microporosity are consequences of the nanocrystalline nature of the AACH phase in the composite. The second weight loss in LFA-BC-25 (transition at 830 K) is associated with the combustion of carbon, although it occurs at *ca.* 300 K lower temperature than in pure carbon. The shift to lower temperature in the composite was also noticed by Schwickardi *et al.* [22] and is due to the catalyzed combustion of the template by the intermediate mixed metal oxide obtained upon decomposition of the precursor. The first and second steps of weight loss in LFABC-25 amount to *ca.* 30 and 50%, respectively. Accordingly, 37 wt.% of this composite is oxide precursor and the remaining 63 wt.% is carbon.

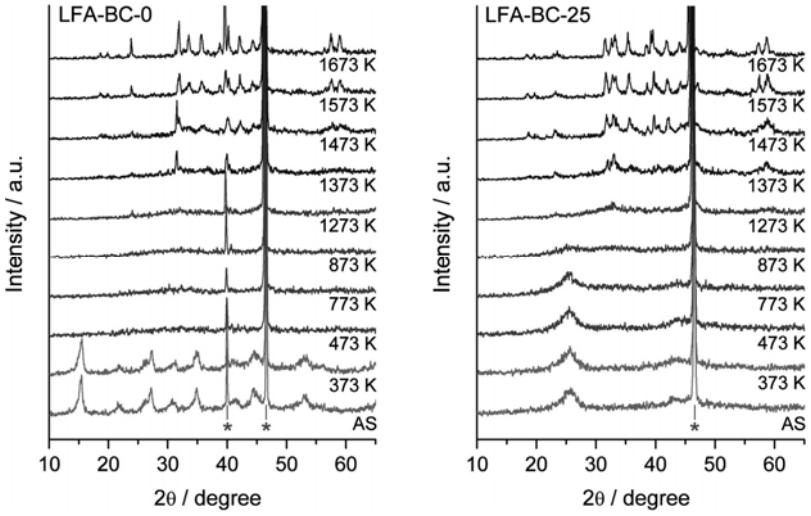

Figure 5. *In situ* X-ray diffraction patterns at selected temperatures during thermal activation of LFA-BC-0 and LFA-BC-25 in air. The reflections marked by asterisk are due to the Pt_{90}-Rh_{10} heater strip.

In situ X-ray diffraction during thermal activation of LFA-BC-0 and LFA-BC-25 in air was carried out to study the evolution of the precursors toward the hexaaluminate and to determine whether the presence of carbon in the composite has any effect on *e.g.* transition temperatures or occurrence of additional or intermediate crystalline phases during thermal activation. Figure 5 shows the patterns of the samples at temperatures

where relevant changes occurred. The characteristic reflections of AACH in LFA-BC-0 vanished at 473 K, leading to an amorphous oxide phase. This temperature is in excellent agreement with thermogravimetry. The XRD of the sample remains silent until 1373 K, where distinctive reflections of $LaFeAl_{11}O_{19}$ (JCPDS 36-1314) start to appear. The hexaaluminate pattern develops on increasing the temperature due to its progressive crystallization.

In correspondence with *ex situ* measurements in Figure 1, the pattern of the LFA-BC-25 composite only displayed the broad reflections at 2θ = 25° and 43° belonging to carbon. The intensity of this reflection gradually decreases with increasing temperature and ultimately disappears at 873 K, in concordance with the occurrence of the weight loss due to carbon combustion in Figure 4. As in the non-templated sample, characteristic reflections of $LaFeAl_{11}O_{19}$ appear in the pattern at 1373 K, *i.e.* the incorporation of carbon did not noticeably affect to the temperature at which the hexaaluminate is formed. In both non-templated and templated oxides, $LaFeAl_{11}O_{19}$ was the only crystalline phase present.

Figure 6 summarizes the morphological changes of the samples prepared by coprecipitation with and without carbon at different stages of the thermal treatment toward the hexaaluminate. Selected temperatures, based on TGA and *in situ* XRD analysis, were 973 K (at which carbon removal is completed), 1273 K (just before hexaaluminate formation), and 1473 K (at which well-crystallized hexaaluminate is attained). In the conventional method, *i.e.* without carbon, the spherical-like nanoparticles in the precipitate developed into platelets upon calcination at 973 K (Figure 6b, left). The platelets extensively agglomerate on further heating, leading to anisotropic elongated hexaaluminate particles with a broad size distribution in the range 40-110 nm (Figure 6d, left). The corresponding carbon-templated samples present remarkable morphological differences. The intermediate oxide at 973 K shows very small particles (5-10 nm) (Figure 6b, right) in contrast with the larger platelets in the carbon-free synthesis. The LFA-BC-25 sample at 973 K clearly shows voids in the structure being the heritage of the carbon that was removed upon combustion. In fact, holes in the size range 20-30 nm can be visualized in the micrograph (also confirmed by N_2 adsorption, vide infra). Carbon removal in our templated sample does not result in hollow sphere architectures with an outer shell of the oxide as found in synthesis

routes using ordered meso- and macroporous carbons [32,33]. The formation of hollow spheres is favoured when the oxide shell surrounding the carbon particle is continuous and relatively thick (in the order of 100 nm [33]), since the strength of the shell is thereby increased. A relatively thin layer of oxide does not resist the pressure generated upon release of CO_2 and H_2O on carbon combustion, fragmenting it into smaller particles. In fact, the vigorous process of carbon removal, cracking the outer shell of the intermediate oxide, could be responsible for the attainment of small oxide particles and large void fraction.

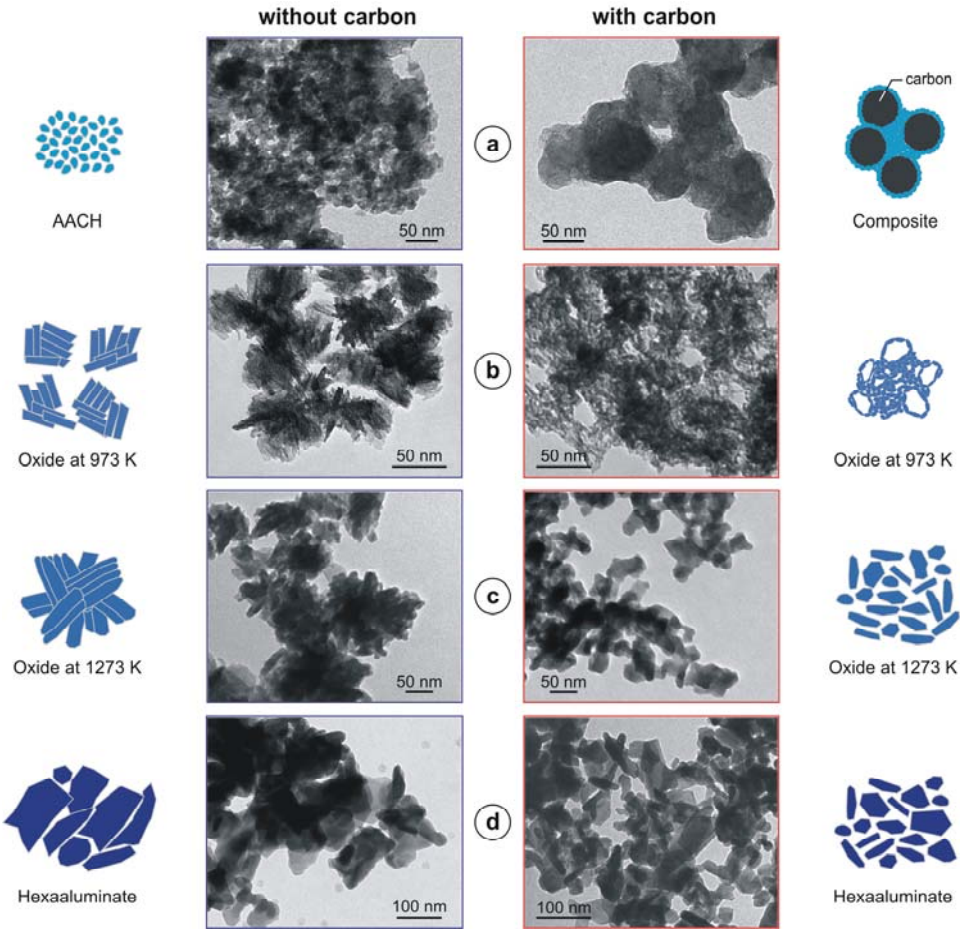

Figure 6. Transmission electron micrographs and pictorial schemes of the samples at different stages during preparation of $LaFeAl_{11}O_{19}$ from LFA-BC-0 (non-templated) and LFA-BC-25 (carbon templated) precursors.

Schwickardi *et al.* [22] proposed that the confinement of the metal nitrate in the pores of an activated carbon with well developed micro- and mesoporosity (S_{BET} = 1500 m^2 g^{-1}), is most probably the origin of small oxide particles and hence high surface areas. This concept can be simplistically visualized as 'dispersing' the metal oxide precursor in the carbon pore network so that agglomeration is reduced. Since our carbon black is purely macroporous (Figure 3 and Table 1), this mechanism can be discarded at an intraparticle level. However, we cannot rule out the confined space synthesis mechanism caused by the interparticle space, which also limits the growth of hexaaluminate precursor. As shown by TEM of the LFA-BC-25 composite (Figure 2), the precipitate should be mostly deposited over the external surface of the carbon particles. Accordingly, we put forward that the confinement-based mechanism [22] is not uniquely responsible for small oxide particles by exotemplating approaches. The precipitation of small crystallites in our composite and particle breakage of oxide particles originated by the carbon combustion process are also important for attaining finely dispersed oxide particles.

The small particles in LFA-BC-25 treated at 973 K certainly grow on increasing the temperature for the attainment of the hexaaluminate phase at 1473 K, but the TEM micrographs in Figure 6d clearly visualized much smaller particles in LFA-BC-25 as compared to LFA-BC-0. A priori, one could anticipate that the small particles of the intermediate oxide at 973 K would grow extensively up to 1473 K, ultimately resembling the hexaaluminate prepared in the absence of carbon. However, the positive effect of carbon toward smaller particles (higher external surface) occurs despite the 300 K difference between the elimination of carbon by combustion and the formation of the hexaaluminate. Consequently, the unique morphology of the intermediate oxide determines the morphology of the final oxide. Figure 7 and Table 1 show the evolution of the textural properties of the as-synthesized samples with and without template and the respective oxides calcined at 973 K and 1473 K.

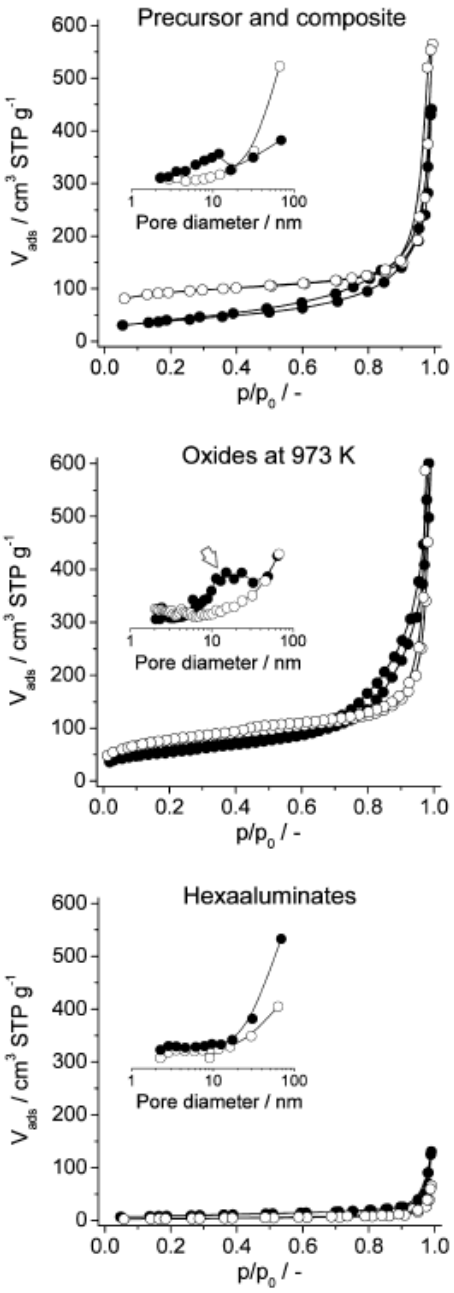

Figure 7. Nitrogen isotherms at 77 K of (○) LFA-BC-0 and (●) LFA-BC-25 at different stages during preparation of $LaFeAl_{11}O_{19}$. Insets: adsorption BJH pore size distributions.

The differences in porosity between the precursor and composite samples were discussed in the previous section. Interestingly, a significantly higher BET surface area of 266 $m^2\ g^{-1}$ is obtained over the oxide at 973 K derived from the carbon-free method compared to the carbon templating route (190 $m^2\ g^{-1}$). This is attributed to a pronounced contribution of microporosity (0.08 $cm^3\ g^{-1}$) to the total surface area of

LFA-BC-0, which is substantially lower (0.01 $cm^3\ g^{-1}$) in LFA-BC-25. The latter sample evidences a higher mesopore surface area of 165 $m^2\ g^{-1}$, mostly obtained by 20-30 nm pores as evidenced in the BJH pore size distribution (inset). This is in good agreement with TEM investigations (Figure 6b, right) and is the result of the templating effect. The hexaaluminate synthesized by the carbon templating route presents a three times higher surface area than the non-templated counterpart (32 *vs.* 11 $m^2\ g^{-1}$) and a somewhat higher total pore volume, as revealed by the increased adsorbed volume at higher relative pressures in the N_2 isotherm. This result ultimately proves the positive effect of the carbon templating route in achieving higher surface areas over high-temperature catalysts such as hexaaluminates.

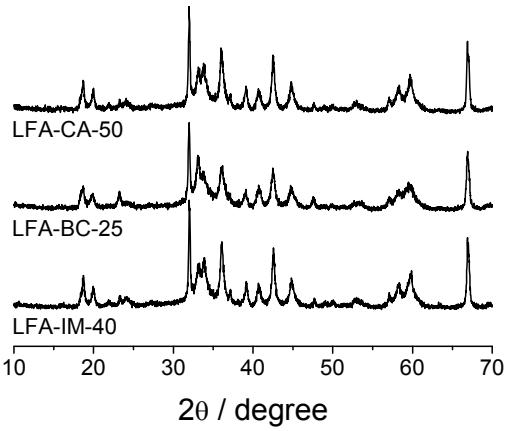

Figure 8. *Ex situ* X-ray diffraction patterns of carbon-templated $LaFeAl_{11}O_{19}$ obtained by different synthesis routes. The reflections correspond to $LaFeAl_{11}O_{19}$, JCPDS 36-1314.

3.3. Hexaaluminates

Ex situ XRD patterns of representative samples obtained by calcination of the differently prepared precursors are shown in Figure 8.

$LaFeAl_{11}O_{19}$ was the only crystalline phase observed, regardless the synthesis route and the carbon content in the precursor. The chemical composition of several non-templated and templated hexaaluminates was determined by ICP-OES. The molar metal ratios in the solids were in all cases very close to the nominal values (La:Fe:Al = 1:1:11), indicating that the preparations were carried out effectively. The positive

effect of carbon templating on the specific surface area of the resulting hexaaluminate has been observed for all the preparation methods.

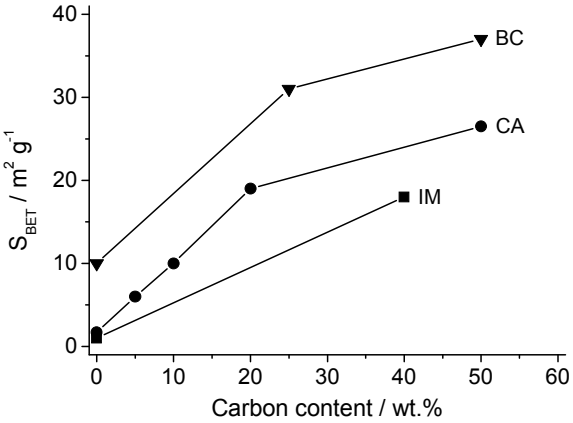

Figure 9. BET surface area of $LaFeAl_{11}O_{19}$ *vs.* the nominal carbon content for different preparation methods.

The BET surface area gradually increases with increasing the nominal carbon content in the composite (Figure 9). The surface area of the non-templated hexaaluminate prepared by coprecipitation is higher than the counterparts prepared by the other two methods. It is then clear that the synthesis route of the precursor is also crucial to maximize the surface area by arriving at smaller hexaaluminate particles. The surface area of the non-templated samples prepared by impregnation and complexation (1-2 m^2 g^{-1}) is enhanced by a factor of 4-25 (depending on the synthesis route) when carbon was incorporated in the synthesis. The highest surface area was attained in the hexaaluminate prepared by coprecipitation using a nominal carbon content of 50 wt.% (*ca.* 40 m^2 g^{-1}). Application of reverse-microemulsion routes generally leads to hexaaluminates with higher surface areas (40-160 m^2 g^{-1}) [15,16,34]. However, the template route using carbon is regarded as highly attractive when balancing the significant increase in surface area of the oxide and the utilization of scalable methods (coprecipitation, impregnation, complexation) for large-scale synthesis of this type of materials.

Prior to demonstrating the benefits of the carbon-templated hexaaluminates in catalytic applications, it is important to evaluate the potential impact of carbon on the nature of the species in the oxide as compared to the hexaaluminate prepared in the absence of template. In the prospects of the work by Schwickardi *et al.* [22], it is hypothesized that for oxides with easily reduced metal ions, intermediate reactions might take place during carbon removal that could lead to low-valence crystalline phases. We have conducted temperature-programmed reduction with hydrogen and X-ray photoelectron spectroscopy in order to comparatively investigate the nature of iron in the non-templated and templated $LaFeAl_{11}O_{19}$ hexaaluminates. The H_2-TPR profiles in Figure 10 show different regions of hydrogen consumption. The peaks centered at 700 and 900 K can be attributed to the formation of ferrous ions and the

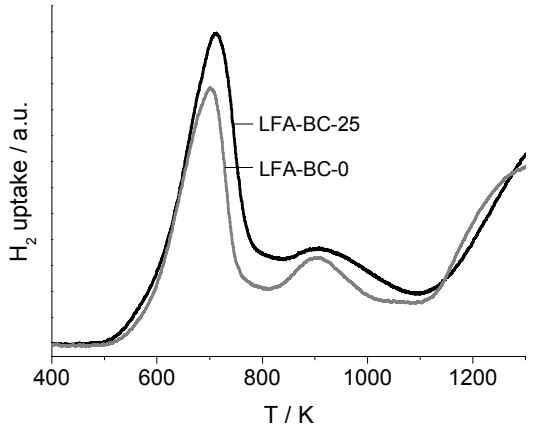

Figure 10. H_2-TPR profiles of $LaFeAl_{11}O_{19}$ prepared by coprecipitation in the absence or presence of carbon.

consumption above 1100 K is assigned to the reduction into metallic iron. Importantly, the results show the practically identical profiles with respect to peak position and amount of hydrogen consumed in the non-templated and templated hexaaluminates, indicating that the nature and amount of redox-active iron species in the oxide are not significantly affected by the incorporation of carbon in the synthesis. However, the H_2-TPR analyses are not meant to quantitatively determine the oxidation state of iron in

UNIVERSITAT ROVIRA I VIRGILI
HEXAALUIMINATE-TYPE CATALYSTS FOR N2O ABATEMENT
Marta Santiago Redondo
ISBN:978-84-693-8864-8/DL:T.1943-2010

the samples, since the assignment of the various overlapped hydrogen consumption peaks is not definitive.

The Fe 2p core level XPS spectra of LFA-BC-0 and LFA-BC-25 (Figure 11) is practically identical, further supporting that the incorporation of carbon in the synthesis does not alter the nature of iron in the final catalysts. The core level XPS spectra of other elements in the hexaaluminate were very similar too. The atomic

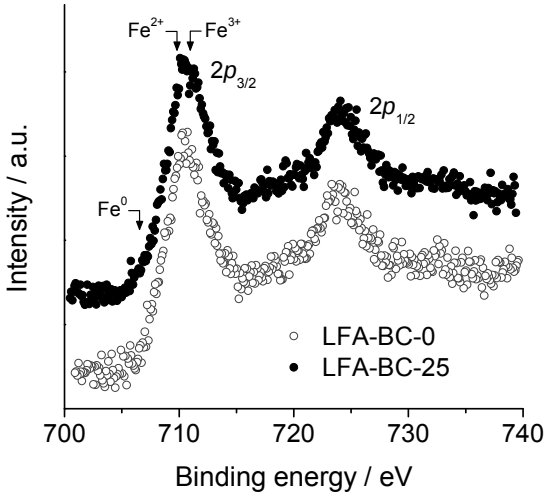

Figure 11. Fe 2p core-level spectra of $LaFeAl_{11}O_{19}$ prepared by coprecipitation in the absence or presence of carbon.

metal ratio determined by XPS was La/Fe/Al = 1.3/0.9/11 in LFABC-0 and 1.2/0.8/11 in LFA-BC-25, indicating a certain enrichment of lanthanum at the hexaaluminate surface with respect to bulk analyses (La/Fe/Al = 1/1/11). The position of the broad peak centered at 710.5 eV in Figure 11 is intermediate between those typically reported for Fe(II) (709.9 eV) and Fe(III) (710.8 eV) [35]. Based on this, the presence of both ferric and ferrous ions in the hexaaluminates can be put forward. Metallic iron, with a characteristic binding energy of 706.5 eV [35], can be safely excluded in the samples. The presence of both Fe^{2+} and Fe^{3+} in different lattice positions of a $LaFeAl_{11}O_{19}$ single crystal (annealed in air at 1773 K) was convincingly shown by Lejus *et al.* [36,37] using XRD, EPR, UV-vis DR spectroscopy, and Mössbauer spectroscopy. In particular, Fe^{2+} (*ca.* 32% of the iron in the sample) was concluded to be preferentially located in

tetrahedral sites of the lattice, while Fe^{3+} (the remaining 67%) appears in tetrahedral as well as bipyramidal sites. The nature of iron in the more widely studied $BaFeAl_{11}O_{19}$ (β-Al_2O_3 structure) is substantially different compared to $LaFeAl_{11}O_{19}$ (magnetoplumbite structure). In the former, iron is exclusively trivalent and occupies octahedral coordination [5,7,38].

3.4. Catalytic activity

In the previous chapter, we demonstrated the excellent performance of non-templated metal-substituted hexaaluminates under simulated process conditions at the outlet of the Pt-Rh gauzes in ammonia burners, *i.e.* in a mixture containing N_2O, NO, O_2, and H_2O.

Now, the improved activity of carbon-templated hexaaluminates with respect to equivalent syntheses in the absence of carbon is demonstrated. For this purpose, a model mixture with N_2O+He was used in the first place.

Both the preparation method and the incorporation of carbon during the synthesis of the hexaaluminate impact on the catalytic performance. In the absence of carbon, the sample prepared by coprecipitation (BC) displays higher activity than the samples prepared by complexation (CA) and impregnation (IM). The T_{50} (temperature for 50% N_2O conversion) is 875 K over LFA-BC-0, shifting to 950 K and 975 K over LFACA-0 and LFA-IM-0, respectively. The templating effect of carbon proves beneficial for the catalytic performance, independent on the synthesis method applied. Accordingly, the light-off is shifted 50-100 K to lower temperature compared to the non-templated samples. As expected, the largest improvement was observed in the sample prepared by impregnation due to the very low surface area of the non-templated hexaaluminate (1 m^2 g^{-1}, Figure 9). As elaborated in the previous section, H2-TPR and XPS characterizations demonstrated that the nature of the iron species in the hexaaluminates prepared was not altered by the incorporation of carbon in the synthesis. Accordingly, the positive effect on the catalytic activity can be exclusively assigned to the enhanced surface area resulting from the stabilization of fine particles induced by the template.

Figure 12 shows the N_2O conversion *vs.* temperature profiles over selected $LaFeAl_{11}O_{19}$ hexaaluminates.

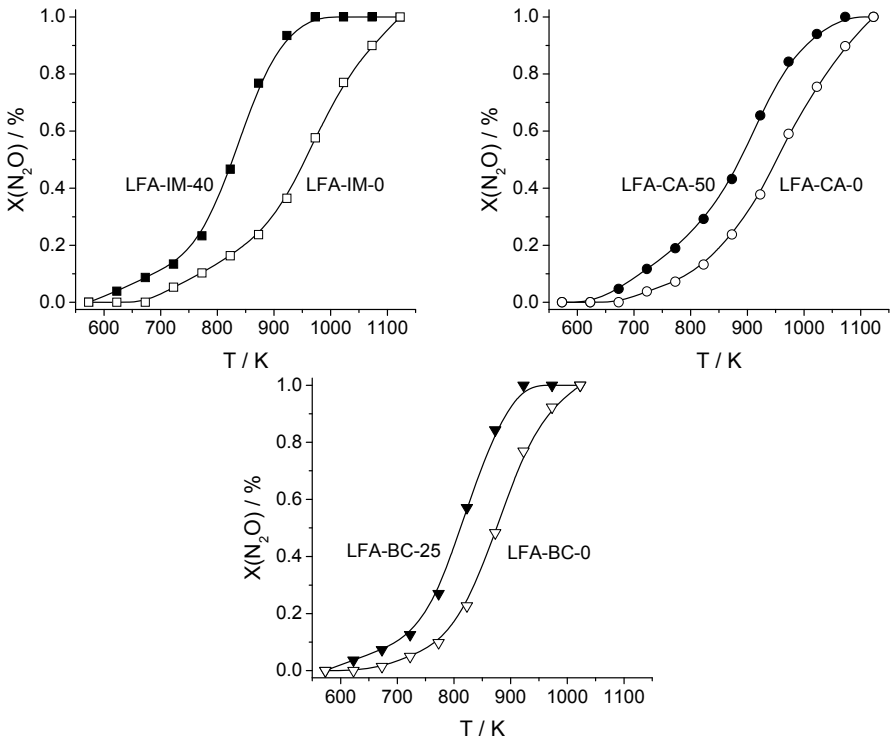

Figure 12. N_2O conversion *vs.* temperature over differently synthesized $LaFeAl_{11}O_{19}$ in the absence or presence of carbon. Conditions: 1.5 mbar N_2O in He, WHSV = 60,000 ml g^{-1} h^{-1}, P =1 bar.

Figure 13 plots the relative reaction rate for N_2O decomposition *vs.* the relative surface area for the catalysts. The values of reaction rate and surface area of the carbon-templated hexaaluminates were normalized with respect to the non-templated counterparts for each preparation method. The reaction rate was determined at 850 K; at this temperature, the degree of N_2O conversion over the catalysts ranges from 20 to 80%. The dependence is quasilinear, indicating that the specific surface area is a prime performance indicator of the catalyst. For example, carbon incorporation in LFA-IM-40 leads to an increased surface area of 15 times with respect to the non-templated LFA-IM-0 counterpart and the reaction rate is 3.5 times higher. In LFA-BC-25, where *S*BET was 3 times higher than in LFA-BC-0, the reaction rate for N_2O decomposition is

doubled. The templated hexaaluminates exhibit smaller particle size, *i.e.* higher surface-to-volume ratios, than the non-templated ones and therefore eventual external diffusion limitations are alleviated. The flattened dependence in Figure 13 upon increasing the surface area can be explained as follows. Below a certain particle size, external diffusion limitations become less important and the chemical regime dominates. In consequence, the surface area of the catalyst has a less marked influence on the reaction rate. Certainly, internal diffusion cannot explain this

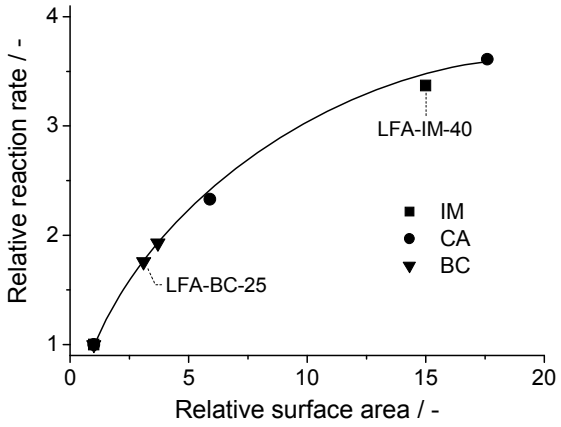

Figure 13. Rate of N_2O decomposition *vs.* BET surface area of $LaFeAl_{11}O_{19}$. The values of reaction rate and specific surface area are relative to those of the non-templated hexaaluminates for each preparation method. Conditions: 1.5 mbar N_2O in He, T = 850 K, WHSV = 60,000 ml g^{-1} h^{-1}, P =1 bar.

behaviour since hexaaluminates are practically non-porous, *i.e.* the total surface area derives from the external surface (particle size effect) and surface roughness.

It can be anticipated that the beneficial effect of carbon templating in a model N_2O+He feed will remain in mixtures simulating more closely process conditions. To demonstrate that, we conducted isothermal tests over LFA-BC-0 and LFA-BC-25 in a feed containing N_2O, NO, O_2, and H_2O. This mimics the outlet gas of the Pt-Rh gauzes in ammonia burners, where N_2O decomposition at high temperature (process-gas option) is practiced [11,41].

UNIVERSITAT ROVIRA I VIRGILI
HEXAALUIMINATE-TYPE CATALYSTS FOR N2O ABATEMENT
Marta Santiago Redondo
ISBN:978-84-693-8864-8/DL:T.1943-2010

As shown in Figure 14, the N_2O conversion was significantly higher over the templated hexaaluminate in model and in simulated feeds. In addition, the stability of the catalysts was remarkable in the 6 h testing period. It is essential for practical implementation that the improved porous properties of the hexaaluminates due to carbon templating are preserved during process operation. We confirmed that the relatively high surface area of LFA-BC-25 was fully retained after 6 h on stream at 923 K. This was foreseen, since the calcination temperature to form the hexaaluminate (1473 K) is several hundreds of degrees higher than the temperature at the outlet of the noble metal gauzes in the ammonia burner.

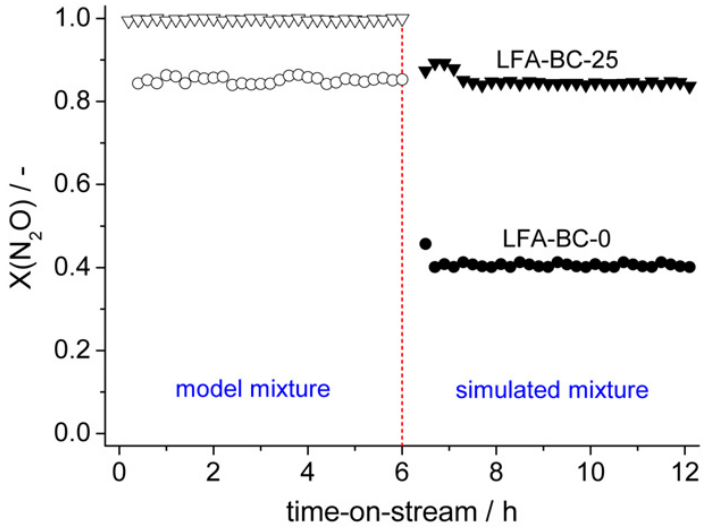

Figure 14. N_2O conversion *vs.* time-on-stream over (○,●) LFA-BC-0 and (∇,▼) FA-BC-25 in a model mixture (open symbols) containing 1.5 mbar N_2O in He and in a simulated mixture (solid symbols) containing 1.5 mbar N_2O, 10 mbar NO, 100 mbar O_2, 100 mbar H_2O in He. Conditions: T = 923 K, WHSV = 60,000 ml g^{-1} h^{-1}, P =1 bar.

Finally, it should be stressed that comparing the de-N_2O performance of metal-substituted hexaaluminates with low-temperature catalysts such as calcined hydrotalcites and zeolites loaded with transition and noble metals [39-41] is not feasible since both systems need to fulfill markedly different requirements and are thus installed in different locations of the process [24]. In the case of nitric acid production, the major source of N_2O in the chemical industry, low-temperature

catalysts (displaying activity <773 K) are applied in the tail-gas train. Contrarily, the intrinsically less active hexaaluminates and other mixed oxide catalysts such as perovskites are installed right after the noble metal gauzes in the ammonia burner. The latter systems must satisfy the number one condition of chemical stability coupled to high catalytic activity for implementation in the harsh environment of the ammonia burner (high temperature and wet oxidizing conditions). Low-temperature catalysts can be discarded under these conditions due to lack of chemical and/or thermal stability.

4. Conclusions

Incorporation of a commercial non-ordered macroporous carbon in the synthesis of metal-substituted hexaaluminates ($LaFeAl_{11}O_{19}$) leads to increased surface areas and improved catalytic performance in N_2O decomposition as compared to the non-templated counterparts. The BET surface area of the oxides is enhanced by a factor of 4-25, depending on the synthesis route and the amount of carbon incorporated. The templating action of carbon leads to finely dispersed hexaaluminate particles, despite the large temperature difference between the combustion of carbon (973 K) and the hexaaluminate formation (1473 K). Analyses of intermediate phases on transformation of the as-synthesized composites into the final hexaaluminates revealed fundamental understanding of the template action. The morphology of the oxide obtained upon carbon removal determines the final properties of the hexaaluminate particles. The growth of small crystallites at the carbon surface in the composite and the vigorous combustion of the template are key aspects in the attainment of small particles through fragmentation of the oxide layer deposited on the template. The confined space synthesis mechanism also contributes. However, it may play a less significant role attending to the purely macroporous nature of the carbon used in this study. The highest surface area was attained in the hexaaluminate prepared by coprecipitation using 50 wt.% of carbon (*ca.* 40 $m^2\ g^{-1}$). This value is lower than reported hexaaluminates using reverse micro-emulsion methods. Advantageously, the templating route is more amenable to practical implementation due its versatility, low cost, simplicity, and scalability. The carbon-templated $LaFeAl_{11}O_{19}$ is more active for N_2O decomposition than the non-templated counterpart and displays stable

conversion in simulated mixtures (containing N_2O, NO, O_2, and H_2O). Our tests demonstrate a quasi-linear correlation between the reaction rate and the specific surface area of the samples. The improved catalytic performance is related to the increased specific surface area of the hexaaluminate, as the nature of iron in the oxide in non-templated and templated oxides was not affected by the incorporation of carbon in the synthesis. Consequently, the carbon-assisted templating route enables the preparation of more efficient high-temperature catalysts, combining reduced light-off temperature with high stability.

5. Acknowledgements

N.M. van der Pers at the Department of Materials Science and Engineering of TUDelft is acknowledged for the *in situ* X-ray analyses and M.S. Yalfani for experimental input. J.C. Groen is acknowledged for his cooperation in this chapter.

References

[1] M. Machida, K. Eguchi, H. Arai, J. Catal. 103 (1987) 385.
[2] M. Machida, K. Eguchi, H. Arai, J. Catal. 120 (1989) 377.
[3] M.F.M. Zwinckels, S.G. Järås, P.G. Menon, T.A. Griffin, Catal. Rev-Sci. Eng. 35 (1993) 319.
[4] G. Groppi, M. Bellotto, C. Cristiani, P. Forzatti, P.L. Villa, Appl. Catal. A 104 (1993) 101.
[5] L. Lietti, C. Cristiani, G. Groppi, P. Forzatti, Catal. Today 59 (2000) 191.
[6] G. Groppi, C. Cristiani, P. Forzatti, Appl. Catal. B 35 (2001) 137.
[7] P. Artizzu-Duart, J.M. Millet, N. Guilhaume, E. Garbowski, M. Primet, Catal. Today 59 (2000) 163.
[8] T.V. Chouldhary, S. Banerjee, V.R. Choudhary, Appl. Catal. A 234 (2002) 1.
[9] R. Kikuchi, Y. Iwasa, T. Takeguchi, K. Eguchi, Appl. Catal. A 281 (2005) 61.
[10] Z. Xu, M. Zhen, Y. Bi, K. Zhen, Appl. Catal. A 198 (2000) 267.
[11] J. Pérez-Ramírez, M. Santiago, Chem. Commun. (2007) 619.
[12] M. Machida, K. Eguchi, H. Arai, J. Am. Ceram. Soc. 71 (1988) 1142.
[13] M.S. Yalfani, M. Santiago, J. Pérez-Ramírez, J. Mater. Chem. 17 (2007) 1222.
[14] P. Forzatti, G. Groppi, Catal. Today 54 (1999) 165.
[15] A.J. Zarur, J.Y. Ying, Nature 403 (2000) 65.
[16] F. Teng, Z. Xu, G. Xiong, Y. Xu, Z. Xu, L. Lin, Green Chem. 7 (2005) 493.
[17] F. Schüth, Angew. Chem. Int. Ed. 42 (2003) 3604, and references therein.
[18] K.J.C. van Bommel, A. Friggeri, S. Shinkai, Angew. Chem. Int. Ed. 42 (2003) 980.
[19] X.S. Zhao, F. Su, Q. Yan, W. Guo, X.Y. Bao, L. Lv, Z. Zhou, J. Mater. Chem. 16 (2006) 637.
[20] C. Madsen, C.J.H. Jacobsen, Chem. Commun. (1999) 673.
[21] M. Kustova, K. Egeblad, K. Zhu, C.H. Christensen, Chem. Mater. 19 (2007) 2915.

[22] M. Schwickardi, T. Johann, W. Schmidt, F. Schüth, Chem. Mater. 14 (2002) 3913.
[23] J. Blanco, A.L. Petre, M. Yates, M.P. Martin, S. Suarez, J.A. Martin, Adv. Mater. 18 (2006) 1162.
[24] J. Pérez-Ramírez, F. Kapteijn, K. Schöffel, J.A. Moulijn, Appl. Catal. B 44 (2003) 117.
[25] J. Pérez-Ramírez, B. Vigeland, Angew. Chem. Int. Ed. 44 (2005) 1112.
[26] S. Brunauer, P.H. Emmett, E.J. Teller, J. Am. Chem. Soc. 60 (1938) 309.
[27] B.C. Lippens, J.H. de Boer, J. Catal. 4 (1965) 319.
[28] E.P. Barret, L.G. Joyner, P.H. Hallenda, J. Am. Chem. Soc. 73 (1951) 373.
[29] K.S.W. Sing, D.H. Everett, R.A.W. Haul, L. Moscou, R.A. Pierotti, J. Rouquerol, T. Siemieniewska, Pure Appl. Chem. 57 (1985) 603.
[30] M.A. Camblor, A. Corma, S. Valencia, Microporous Mesoporous Mater. 25 (1998) 59.
[31] G. Stoica, J. Pérez-Ramírez, Chem. Mater. 19 (2007) 4783.
[32] L. Zhibin, L. Jianmin, K. Yanxiong, Y. Zhang, H. Zhang, L. Fanqing, X. Jinyun, J. Mater. Chem. 11 (2001) 2930.
[33] X. Yongde, R. Mokaya, J. Mater. Chem. 15 (2005) 3126.
[34] Z. You, K. Inazu, K. Aika, T. Baba, J. Catal. 251 (2007) 321.
[35] D.D. Hawn, B.M. DeKoven, Surf. Interface Anal. 10 (1987) 63.
[36] F. Laville, A.M. Lejus, J. Cryst. Growth 63 (1983) 426.
[37] E. Tronc, F. Laville, M. Gasperin, A.M. Lejus, D. Vivien, J. Solid State Chem. 81 (1989) 192.
[38] D. Naoufal, J.-M. Millet, E. Garbowski, Y. Brullé, M. Primet, Catal. Lett. 54 (1998) 141.
[39] Y. Li, J.N. Armor, Appl. Catal. B 1 (1992) L21.
[40] F. Kapteijn, J. Rodríguez-Mirasol, J.A. Moulijn, Appl. Catal. B 9 (1996) 25.
[41] J. Pérez-Ramírez, J. Overejinder, F. Kapteijn, J.A. Moulijn, Appl. Catal. B 23 (1999) 59.

UNIVERSITAT ROVIRA I VIRGILI
HEXAALUIMINATE-TYPE CATALYSTS FOR N2O ABATEMENT
Marta Santiago Redondo
ISBN:978-84-693-8864-8/DL:T.1943-2010

Chapter 5

Evaluation of catalysts for N_2O abatement in fluidized-bed combustion

Several catalysts, including FeZSM-5, Co_2AlO_4, $LaCoO_3$, and $BaFeAl_{11}O_{19}$, were evaluated for N_2O decomposition under representative flue-gas conditions in fluidized-bed combustion (FBC). Closely related formulations proved active and stable catalysts for process-gas or tail-gas de-N_2O in nitric acid plants. With this as starting point, their potential suitability for N_2O abatement in stationary combustion was assessed. Tests were carried out in a fixed-bed reactor at ambient pressure and in the temperature range of 473-1123 K using mixtures of N_2O, O_2, NO, CO, SO_2, and H_2O. The mixed oxide catalysts were strongly inhibited by water and sulfur dioxide and experienced fast deactivation in the simulated mixture containing all the gases. Bulk sulfate phases were detected by X-ray diffraction in the used perovskite and hexaaluminate, revealing insufficient chemical stability in the presence of sulphur and discouraging installation in the freeboard of the combustor. In great contrast, the activity of steam activated FeZSM-5 in the model and simulated mixtures was comparable, rendering very stable performance during 30 h on stream. The unique tolerance of this iron zeolite to the complex combination of feed components makes it prone to implementation after the cyclone of FBCs, where temperatures are typically 800-1100 K.

This chapter is based on the following publication:
M. Santiago, M.A.G. Hevia, J. Pérez-Ramírez, Appl. Catal. B 90 (2009) 83.

1. Introduction

The energy demand grows exponentially due to the increasing consumption in developed countries and the electrification of the Third World. Among fossil fuels, coal is the most vital energy resource, providing more than 40% of the World electric power. The coal consumption pace will probably remain and even increase due to its higher abundance and more even distribution around the globe compared to oil and gas [1]. The concern associated with SO_x and NO_x emissions from coal fired power plants led to the necessity of developing environmentally friendlier combustion technology, such as fluidized-bed combustion (FBC). Fluidized-bed combustors operate at a relatively low combustion temperature (1023-1173 K), leading to lower emission levels of NO_x and optimal conditions for sulphur capture by limestone or dolomite [2]. They are also versatile with respect to the type of fuel (fossil, biomass, and general waste). Unfortunately, these merits are off-set by a strongly increased emission of N_2O, reaching values up to 600 ppm depending on the combustion temperature, type of combustor, and fuel used [3-5].

The most important pathways that lead to N_2O are the homogeneous oxidation of N-groups in volatiles (mainly HCN) and heterogeneous reactions (direct oxidation of char-N and the reaction of char-N with NO) [4]. Anthropogenic N_2O emissions have become increasingly under review by environmental authorities over the last decade due to its recognized action as a powerful greenhouse gas and its inclusion in the Kyoto protocol. A number of catalysts based on bulk and supported mixed metal oxides and metal-loaded zeolites have been implemented for N_2O decomposition in adipic acid plants (*e.g.* $CuAl_2O_4/Al_2O_3$ and Ag/Al_2O_3 by BASF, $CoO\text{-}NiO/ZrO_2$ by DuPont, and CuO/Al_2O_3 by Asahi Chemical) [6] and in nitric acid plants (CuO/Al_2O_3 by BASF, $La_{0.8}Ce_{0.2}CoO_3$ by Johnson Matthey, Co_2AlO_4/CeO_2 by Yara International, and FeZSM-5 by Uhde) [7].

Other catalytic systems have been recently evaluated under simulated conditions of adipic acid and nitric acid plants, such as yttrium-doped zirconias [8], $AB_{1-x}B'_xO_3$ perovskites with A = La or Ca, B = Mn or Fe, and B' = Cu or Ni [9], $ABAl_{11}O_{19}$ hexaaluminates with A = Ba or La and B = Fe, Mn, Co, or Ni) [10], α-alumina supported iron oxide [11], and mayenite [12]. In contrast to chemical plants, catalytic technology for N_2O mitigation in fluidized-bed combustion has not been installed so far.

UNIVERSITAT ROVIRA I VIRGILI
HEXAALUIMINATE-TYPE CATALYSTS FOR N2O ABATEMENT
Marta Santiago Redondo
ISBN:978-84-693-8864-8/DL:T.1943-2010

The global N_2O emission from fossil-fuel combustion is estimated at 60-160 Mton CO_2-eq per year [13], without taking account the still uncertain emission from biomass and waste combustion. The overall figure likely exceeds the N_2O emission from nitric acid production (125 Mton CO_2-eq per year), which is currently the largest source in the chemical industry. Accordingly, the enforcement of environmental regulations for N_2O control in combustion processes can be foreseen in the short term. Additional incentive for producers comes from a recent directive that includes N_2O as a tradable gas under the EU Emission Trading Scheme for the period 2008-2012 [14].

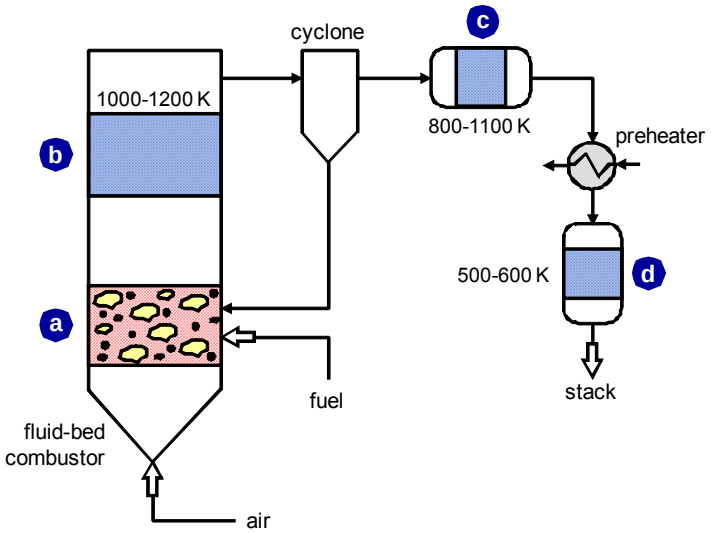

Figure 1. Simplified flow sheet of a bubbling fluidized-bed combustor with possible locations for catalytic N_2O abatement. The position determines the main requirements for a suitable catalyst: high chemical stability and attrition resistance in (a) and low-temperature activity in (c). The location after the cyclone (b) is an intermediate case.

In a bubbling fluidized-bed combustor, three locations for catalytic N_2O abatement can be potentially conceived (Figure 1): (a) in the freeboard (1000-1200 K), (b) after the cyclone (800-1100 K), or (c) after the preheater (500-600 K). A major difficulty to develop robust de-N_2O catalysts in FBC off-gases stems from the complexity of the mixtures, containing N_2O, O_2, NO_x, CO, CO_2, SO_2, and H_2O. Several papers have addressed the de-N_2O activity of different catalysts in the presence of some of these gases [15-23], which often cause strong inhibition and deactivation. However, there is

a clear lack of systematic studies including individual and combined effects of the components over representative catalysts. In particular, the sulfur tolerance is of primary importance for combustion applications and requires deeper analysis.

As starting point, it appears reasonable to evaluate whether existing de-N_2O catalysts for the aforementioned chemical plants are suitable for FBCs. It should be recalled that the extrapolation of catalytic technology from one source to another is often infertile, as de-N_2O catalysts are designed for particular conditions of feed composition, temperature, and pressure [7].

Herein, we have investigated Co_2AlO_4 spinel, $LaCoO_3$ perovskite, $BaFeAl_{11}O_{19}$ hexaaluminate, and FeZSM-5 zeolite for catalytic N_2O decomposition under realistic conditions of FBC off-gases. The catalytic performance was evaluated in model and simulated flue-gas mixtures and the effect of individual gaseous components for each catalyst was categorized. The three mixed oxide catalysts decompose N_2O beneath the Pt-Rh gauzes in ammonia burners of nitric acid plants [7,10], withstanding temperatures in the range 1073-1173 K and high concentrations of O_2, NO, andH_2O. Based on their remarkable chemical stability under harsh conditions, they can be regarded as potential candidates for de-N_2O in the freeboard of the combustor (Figure 1). The iron zeolite, used for tail-gas N_2O abatement in nitric acid plants, is attractive because the rate of N_2O removal is accelerated by SO_2 [24]. However, tests were conducted in the absence of other relevant gaseous components such as NO, CO, and H_2O. Differently to previous works over iron-containing zeolites [17,22,23], the extra addition of hydrocarbons as reducing agents was explicitly avoided in order to maximize the cost effectiveness of the catalytic after-treatment. Based on our results, prospects for practical implementation are discussed.

2. Experimental

2.1. Catalyst preparation

The mixed oxides (Co_2AlO_4, $LaCoO_3$, and $BaFeAl_{11}O_{19}$) were prepared by coprecipitation of the corresponding precursors using the in-line dispersion precipitation (ILDP) method [25] followed by high-temperature calcination. An aqueous solution of the corresponding metal nitrates (spinel: 0.2 M Co and 0.1 M Al,

perovskite: 0.1 M La and 0.1 M Co, and hexaaluminate: 0.1 M Ba, 0.1 M Fe, and 1.1 M Al) and an aqueous solution of 2 M Na_2CO_3 (spinel and perovskite precursors) or $(NH_4)_2CO_3$ (hexaaluminate precursor) were pumped into a 6 ml microreactor attached to a high-shear homogenizer rotating at 13,500 rpm. The pH of the slurry was measured and controlled by an in-line probe directly at the outlet of the precipitation chamber. Syntheses were carried out at constant pH 8 with an average residence time of 18 s. The slurries were aged at 333 K for 3 h, filtered, washed thoroughly, and dried at 353 K for 12 h. The resulting solids were calcined in static air at 1123 K (Co_2AlO_4), 1273 K ($LaCoO_3$), and 1473 K ($BaFeAl_{11}O_{19}$) for 10 h using a heating rate of 5 K min^{-1}. The preparation of steam activated FeZSM-5 was detailed elsewhere [26]. Briefly, the isomorphously substituted iron zeolite was prepared by hydrothermal synthesis using TPA^+ as the template followed by calcination in static air (823 K, 10 h) and steam treatment (300 mbar H_2O and 30 ml STP N_2 min^{-1}, 873 K, 5 h).

2.2. Catalyst characterization

The chemical composition of the catalysts was determined by X-Ray Fluorescence (Philips PW 2400) and by Inductive Coupled Plasma-Optical Emission Spectroscopy (PerkinElmer Optima 3200RL (radial)). Powder diffraction patterns were measured in a Siemens D5000 diffractometer with Bragg-Brentano geometry and Ni-filtered Cu Kα radiation (λ = 0.1541 nm). Data were recorded in the range 5-70° 2θ with an angular step size of 0.05° and a counting time of 8 s per step. N_2 adsorption at 77 K was performed in a Quantachrome Autosorb 1-MP gas adsorption analyzer. Prior to analysis, the samples were degassed at 473 K for 6 h.

2.3. Activity tests

Activity tests were carried out in a MicroActivity Reference setup (PID Eng&Tech) using a quartz microreactor (9 mm i.d.). The catalyst (0.1 g, sieve fraction 125-300 mm) was loaded between two layers of quartz wool and rested over a porous frit. The sample was pretreated in He at 673 K for 1 h and cooled down to the initial reaction temperature (473 K). Then, the feed mixture was introduced and the temperature was increased at intervals of 25-50 K up to 1123 K, using a heating rate of 5 K min^{-1} and

keeping an isothermal period of 30 min at each set point. In this period of time, constant conversion levels were obtained and can be considered as the steady state. The experiments were carried out at ambient pressure using a space time ($W/F°(N_2O)$) of 1245 g h mol^{-1}. Gas mixtures containing 0.3 mbar N_2O, 60 mbar O_2, 0.1 mbar NO, 0.14 mbar CO, 0.1 mbar SO_2, and 100 mbar H_2O in He were used. The N_2O conversion *vs.* temperature curves for each feed composition was measured with a fresh catalyst sample. The stability of selected catalysts was studied by means of isothermal tests in the full gas mixture. Reactant and product gases were analyzed by a gas chromatograph (Agilent 6890N) equipped with HP-PLOT and DB-FFAP columns and TCD and FID detectors.

3. Results and discussion

3.1. Catalyst characterization

Prior to catalytic tests, the materials were subjected to basic characterization. The molar metal ratios in the mixed oxides determined by XRF were very close to the nominal values, indicating that the coprecipitation step was carried out effectively. As shown in Figure 2, the X-ray diffraction patterns of the samples correspond to the desired pure phases: spinel (Co_2AlO_4, JCPDS 38-814), perovskite ($LaCoO_3$, JCPDS 25-1060), and hexaaluminate ($BaFeAl_{11}O_{19}$, JCPDS 26-135). Due to the high calcination temperature required for their crystallization, the bulk mixed oxides have a relatively low BET surface area, *i.e.* 20 m^2 g^{-1} in Co_2AlO_4, 4 m^2 g^{-1} in $LaCoO_3$, and 12 m^2 g^{-1} in $BaFeAl_{11}O_{19}$ The iron zeolite contains a molar Si/Al ratio of 31.3 and 0.67 wt.% Fe as determined by ICP. Extensive physico-chemical characterization of this specific catalyst was reported elsewhere [26-28] and will not be repeated here for the shake of conciseness. The material contains a distribution of extraframework iron species in the form of isolated ions, oligonuclear species, and iron oxide nanoparticles of 1-2 nm.

UNIVERSITAT ROVIRA I VIRGILI
HEXAALUIMINATE-TYPE CATALYSTS FOR N2O ABATEMENT
Marta Santiago Redondo
ISBN:978-84-693-8864-8/DL:T.1943-2010

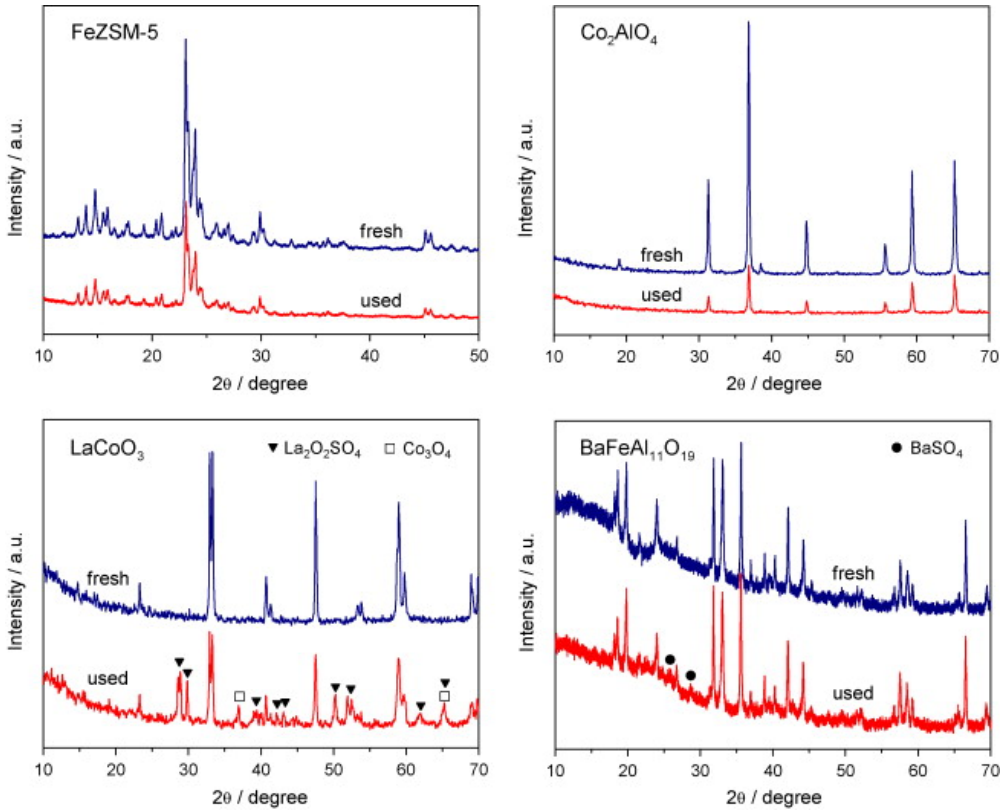

Figure 2. X-ray diffraction patterns of the catalysts before and after catalytic tests in the simulated FBC mixture (see caption of Figure 3).

3.2. Model *vs.* simulated mixtures

First of all, the catalytic activity of the four catalysts was evaluated in model and simulated mixtures. Figure 3a shows the N_2O conversion *vs.* temperature in a feed containing only N_2O and O_2. The iron zeolite was the most active catalyst, displaying significant N_2O conversion above 700 K, followed by the spinel and the hexaaluminate. The perovskite resembles the spinel in the low temperature region, shifting towards the hexaaluminate at higher temperatures. A quantitative comparison of the four catalysts can be given by the T_{50} (temperature at 50% N_2O conversion): 770 K for FeZSM-5, 860 K for Co_2AlO_4, and 900 K for $LaCoO_3$ and $BaFeAl_{11}O_{19}$. Tests in the simulated FBC mixture, containing N_2O, O_2, NO, CO, SO_2, and H_2O rendered a completely different picture. The concentration of the components was selected attending to values in the literature for FBC flue-gases [13] and following advice from recognized experts in the field of coal combustion [29].

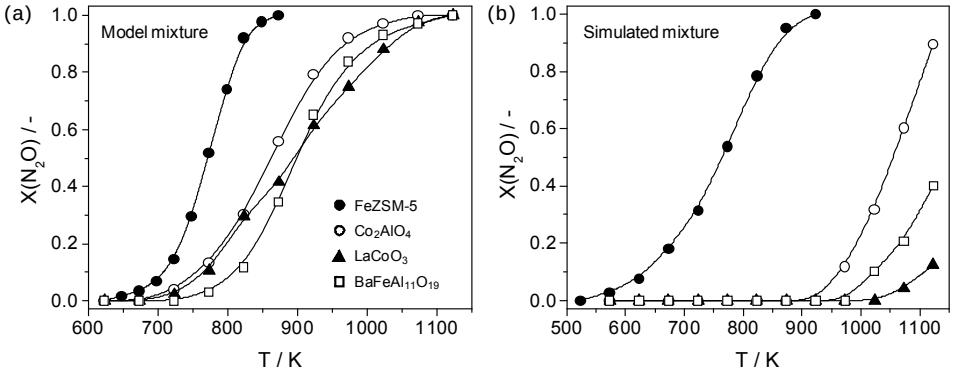

Figure 3. N_2O conversion *vs.* temperature over the catalysts in (a) model and (b) simulated mixtures. The model mixture contains 0.3 mbar N_2O and 60 mbar O_2 in He. The simulated mixture contains 0.3 mbar N_2O, 60 mbar O_2, 0.1 mbar NO, 0.14 mbar CO, 0.1 mbar SO_2, and 100 mbar H_2O in He. Other conditions: P = 1 bar and $W/F°(N_2O)$ = 1245 g h mol^{-1}.

Comparison of the N_2O conversion curves in Figure 3a and b makes it possible to conclude that the iron zeolite behaves similarly in the model and simulated mixtures (T_{50} = 770 K), while the de-N_2O activity of the mixed oxide catalysts is severely suppressed in the complex mixture with additional gases. For example, the T_{50} of Co_2AlO_4 shifts from 860 K in the model feed to 1050 K in the simulated feed. $BaFeAl_{11}O_{19}$ and $LaCoO_3$ suffered from a more pronounced inhibiting effect, particularly the perovskite. Accordingly, the activity differences are emphasized under realistic process conditions, enabling a proper discrimination of the catalysts.

This statement is further supported by two particular examples. First of all, the light-off temperature in the model mixture is 100 K lower over the zeolite than over the spinel, and more than 350 K in the simulated mixture. Secondly, the simulated mixture evidences more pronounced activity differences between the three mixed oxide catalysts in comparison with the model mixture. In conclusion, these results highlight the absolute necessity of conducting experiments at conditions as close as possible to the real process in order to draw valid conclusions on their potential practical interest. It is often felt that optimistic assessment of catalysts in the literature is made from tests in mixtures that contain only some of the relevant gases in the source under consideration.

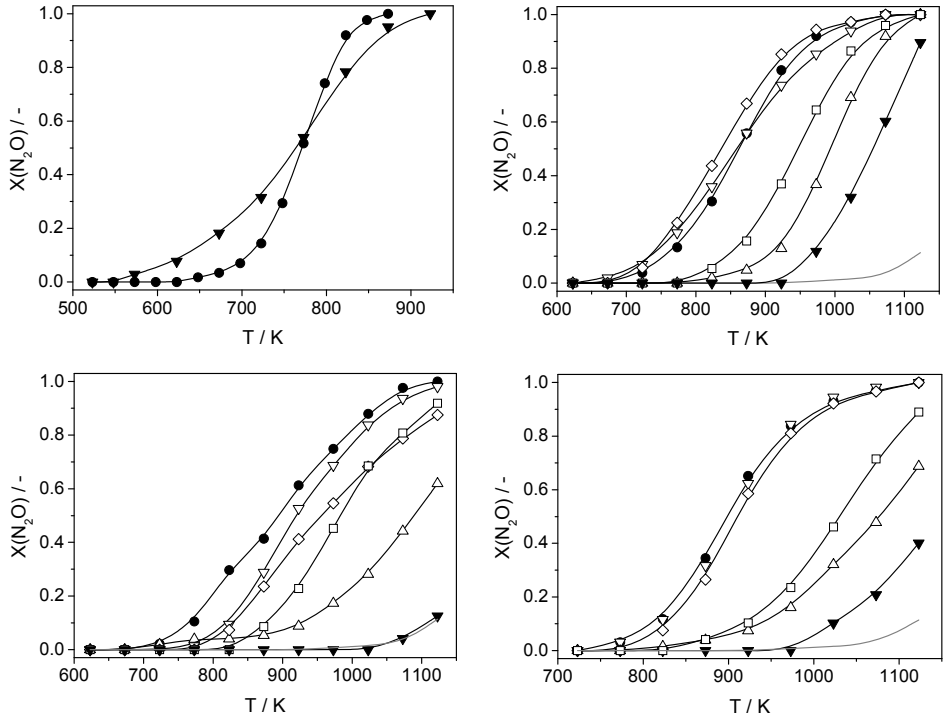

Figure 4. N_2O conversion *vs.* temperature over the catalysts in different mixtures, which are indicated in the legend of the hexaaluminate sample. The partial pressure of the components was 0.3 mbar N_2O, 60 mbar O_2, 0.1 mbar NO, 0.14 mbar CO, 0.1 mbar SO_2, and 100 mbar H_2O in He. Other conditions: P = 1 bar and W/F°(N_2O) = 1245 g h mol^{-1}. Gray line: N_2O conversion in a blank experiment with the empty quartz reactor.

3.3. Effect of individual gases

The influence of each constituent of the gas mixture on the de-N_2O activity was investigated by adding one component to the N_2O+O_2 mixture over fresh catalyst. The resulting conversion profiles are depicted in Figure 4. It can be seen that CO and NO affected to a minor extent the de-N_2O activity over the spinel, hexaaluminate, and perovskite catalysts. $LaCoO_3$ presented some inhibition by NO, most likely due to competitive adsorption with N_2O for active sites and/or to the formation of stable surface nitrate species. Water suppressed the catalytic activity to a much larger extent due to active site blockage, causing a shift of the N_2O conversion profiles by *ca.* 100-125 K to higher temperatures. The strongest inhibition was caused by sulfur dioxide,

increasing the operation temperature by 200 K for the same degree of N_2O conversion. At low temperatures, the behaviour of the mixed oxides is similar in the presence of SO_2, *i.e.* N_2O conversion is measurable above 923 K. However, in the high temperature region, Co_2AlO_4 appears less affected than $LaCoO_3$ and $BaFeAl_{11}O_{19}$. The N_2O conversion in the full mixture was much lower than with the individual components, indicating that the combination of gases exerts a more detrimental effect on the catalytic activity. In fact, $LaCoO_3$ was completely inactive, since the conversion profile matched the conversion of the empty quartz reactor (gray line in Figure 4).

After the test in the simulated FBC gas mixture, the catalysts were re-tested in the model N_2O+O_2 mixture. All of them displayed a much lower N_2O conversion, confirming that the mixed oxides were severely deactivated under simulated conditions of FBC off-gases. Irreversible deactivation occurred when sulfur dioxide was present in the feed and particularly in combination with water. The inhibition and deactivation of the mixed oxides by sulfur dioxide can a priori be attributed to sulfate formation. The drastic effect of SO_2 on the structural integrity of some of the mixed oxides due to extensive sulfation was confirmed by inspecting the X-ray diffraction patterns of the catalysts after the test in the simulated mixture. As seen in Figure 2, the used catalysts were less crystalline than the fresh counterparts.

More noticeably, the perovskite phase partially segregated into lanthanum oxysulfate (La2O2SO4, JCPDS 41-678) and cobalt oxide (Co_3O_4, JCPDS 43-1003), while traces of baryte ($BaSO_4$, JCPDS 01-072-1378) were detected in the used hexaaluminate. Additional reflections belonging to bulk sulfate containing or other phases were not detected in the pattern of Co_2AlO_4, suggesting that sulfation only occurs at a surface level.

The catalytic behaviour of FeZSM-5 is radically different from those of the mixed oxides. The outcome is that the catalytic activity in the full mixture is somewhat higher than in the model mixture <773 K and slightly lower above this temperature (Figure 4). The apparent activation energy of FeZSM-5 in N_2O+O_2 was estimated at 137 kJ mol^{-1}, being reduced to 86 kJ mol^{-1} in the simulated mixture. The unique tolerance of the steam-activated iron zeolite can be envisaged attending to works in the literature dealing with this specific catalytic system. Individually, the N_2O decomposition activity

is not affected by O_2 [30], while NO [31], CO [32], and SO_2 [24] promote the catalytic N_2O removal with or without O_2 in the feed.

As detailed in these publications, nitric oxide is a gaseous promoter and facilitates O_2 desorption via adsorbed NO_2 intermediates, while carbon monoxide and sulfur dioxide act as selective reducing agents scavenging adsorbed oxygen species deposited by N_2O. H_2O decreases the de-N_2O activity of steam activated. FeZSM-5, although its excellent hydrothermal stability in simulated tail-gases of nitric acid plants has been highlighted [30]. The combination of all these gases renders a catalyst yielding pretty comparable activity in the model and simulated mixtures. In our recent work over iron-containing zeolites with sulfur dioxide [24], tests were conducted in N_2O+SO_2(+O_2), *i.e.* without other relevant gaseous components. Herein we show that the unique behaviour of FeZSM-5 applies to simulated FBC mixtures. The X-ray diffraction pattern of the used iron zeolite was not altered (Figure 3), although it experienced certain loss of crystallinity as generally noticed for the mixed oxides.

3.4. Stability

Stability tests were conducted over the spinel and zeolite catalysts. For this purpose, attending to the profiles in Figure 3, the temperature was set at 773 K (FeZSM-5) and 973 K (Co_2AlO_4) in N_2O+O_2 and after 2 h, the simulated FBC mixture was introduced. In this manner, the short-term stability is studied at intermediate degrees of N_2O conversion. The N_2O conversion *vs.* time is shown in Figure 5. Co_2AlO_4 rapidly losses its activity, going from *ca.* 20% in the simulated mixture to practically no activity after 30 h on stream. Switching the feed back to the model feed at the same temperature led to a N_2O conversion of 45%, *i.e.* much lower than the *ca.* 90% of the fresh sample. This confirms the partial irreversible deactivation of the catalyst. In contrast, FeZSM-5 is stable during the 30-h period, keeping a fairly constant degree of N_2O conversion at *ca.* 65%.

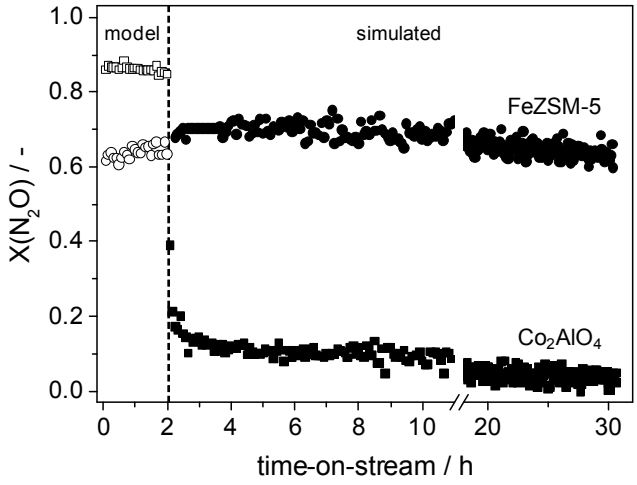

Figure 5. N_2O conversion *vs.* time-on-stream over FeZSM-5 (circles) at 773 K and Co_2AlO_4 (squares) at 973 K in model and simulated mixtures. Conditions as in caption of Figure 3.

Previous tests in the presence of water over this zeolite were conducted in mixtures with 1.5 vol.% H_2O [30], *i.e.* the characteristic content in the tail-gas of nitric acid plants. The water content in FBC off-gases is considerably higher (10 vol.% H_2O was used here). Due to this, zeolite dealumination can occur and might provoke structural damage, clustering of active iron species, and ultimately deactivation. Based on the stable N_2O conversion in Figure 5, we believe that eventual dealumination of our zeolite in the catalytic tests was largely minimized. This is due to the particular preparation of the iron zeolite, specifically the treatment in a stream of inert containing 30 vol.% H_2O at 873 K for 5 h. This activation step, which is primarily intended for dislodgement of isomorphously substituted iron towards active extra-framework positions, also causes partial dealumination [26-28]. In our opinion, the treatment effectively stabilizes the zeolite for subsequent use in wet waste streams since both temperature and steam content are more severe in the activation step than under optimal operating FBC conditions. We inspected the used zeolite after the isothermal stability test by transmission electron microscopy, observing that the size of the visible iron oxide nanoparticles was not altered, *e.g.* due to clustering and sintering, with respect to the fresh zeolite (not shown). Additional characterization of intracrystalline iron species such as isolated ions and oligonuclear clusters in the

zeolite pores is beyond the scope of this paper and would be needed to confirm the no alternation of the iron speciation.

3.5. Opportunities for implementation in FBC

The implementation of N_2O abatement technology in flue-gases of fluidized-bed combustors should likely occur within the next few years due to (i) the significant emission, even exceeding that of chemical production processes, (ii) the enforcement of environmental regulations by governments, and (iii) the recent inclusion of N_2O as a tradable greenhouse gas under the EU Emission Trading Scheme. The extrapolation of catalytic systems operative in chemical plants to FBCs is not straightforward due to the distinct conditions. The presence of SO_2 combined with high concentrations of H_2O characteristic of combustion processes are critical aspects to develop stable catalysts. The spinel, perovskite, and hexaaluminate catalysts evaluated in this study proved highly stable for process-gas N_2O decomposition in ammonia burners of nitric acid plants, *i.e.* withstanding high temperatures (1073-1173 K) and the presence of high concentrations of O_2, NO, and H_2O [7,10]. However, the mixed oxides are very sensitive to sulfur and the presence of water, experiencing rapid deactivation. The chance of implementing such system in FBCs, *e.g.* in the freeboard of a bubbling fluidized-bed, is remote in view of their limited chemical stability whenever sulfur dioxide is present. The same outcome in this or other location of the process is expected over other active N_2O decomposition catalysts such as Rh/Al_2O_3 [15], Rh/ZrO_2 [20], Ru/Al_2O_3 [33], calcined Co-Al hydrotalcites with Rh or Pd [34], Co-ZSM-5 [35], and Cu-ZSM-5 [35,36], since they are also strongly inhibited and or deactivated by SO_2. The sulfur tolerance is of primary importance to develop robust catalysts in environmental applications associated with combustion sources, not only for N_2O abatement but also for NOx storage and reduction [37-39] and hydrocarbon oxidation [40,41]. Promising results arise from the application of steam-activated FeZSM-5 zeolite. This system is unique since its de-N_2O activity is promoted by components coined as inhibitors and poisons for most catalysts (mainly NO and SO_2). Stable performance has been obtained during 30 h on stream at 773 K. This temperature is too high for eventual installation of the catalyst after the preheater, where the temperature does not exceed 600 K (position c in Figure 1). Addition of hydrocarbons (*e.g.* propane) could lower the

operating temperature of the iron zeolite [22,23]. However, reaching a complete degree of N_2O conversion remains challenging at such low temperature. In addition, the operating cost of the 'selective catalytic reduction' option is prohibitive compared to the 'direct decomposition' option [7]. The location of the iron zeolite catalyst after the cyclone (Figure 1, position b) appears suitable attending to the available temperature (800-1100 K). As discussed above, the synthesis route of FeZSM-5 is considered to be a decisive factor for its stable behaviour. The steam treatment of our catalyst under conditions (temperature, steam content) exceeding its operation in FBCs is advisable to stabilize the zeolite framework and distribution of iron species in the material.

4. Conclusions

The extrapolation of commercial catalysis for N_2O abatement in chemical plants to stationary combustion sources such as fluidized-bed combustions requires careful consideration. In spite of their remarkable performance for process-gas N_2O abatement in nitric acid plants, mixed oxide catalysts such as Co_2AlO_4, $LaCoO_3$, and $BaFeAl_{11}O_{19}$, lack chemical stability and experience severe deactivation under FBC conditions, mainly due to the presence of SO_2 and H_2O. Steam-activated FeZSM-5 zeolite displays remarkable activity and stability and is a serious candidate for practical implementation in stationary combustion facilities.

References

[1] http://www.worldcoal.org, January 3, 2009.
[2] S.N. Oka, Fluidized-Bed Combustion, Marcel Dekker, New York, 2004.
[3] M.A. Wójtowicz, J.R. Pels, J.A. Moulijn, Fuel Process. Technol. 34 (1993) 1.
[4] L. Armesto, H. Boerritger, A. Bahillo, J. Otero, Fuel 82 (2003) 1845.
[5] M.J. Fernandez Gutierrez, D. Baxter, C. Hunter, K. Svoboda, Waste Manage. Res. 23 (2005) 133.
[6] A. Shimizu, K. Tanaka, M. Fujimori, Chemosphere 2 (2000) 425.
[7] J. Pérez-Ramírez, F. Kapteijn, K. Schöffel, J.A. Moulijn, Appl. Catal. B 44 (2003) 117.
[8] P. Granger, P. Esteves, S. Kieger, L. Navascues,G. Leclercq, Appl. Catal. B 62 (2006) 236.
[9] S. Alini, F. Basile, S. Blasioli, C. Rinaldi, A. Vaccari, Appl. Catal. B 70 (2007) 323.
[10] J. Pérez-Ramírez, M. Santiago, Chem. Commun. (2007) 619.
[11] G. Giecko, T. Borowiecki, W. Gac, J. Kruk, Catal. Today 137 (2008) 403.

[12] M. Ruszak, M. Inger, S. Witkowski, M. Wilk, A. Kotarba, Z. Sokja, Catal. Lett. 126 (2008) 72.
[13] F. Kapteijn, J. Rodríguez-Mirasol, J.A. Moulijn, Appl. Catal. B 9 (1996) 25.
[14] Reference COD/2008/0013, amendment of Directive 2003/87/EC, more details available at http://ec.europa.eu/environment/climat/emission, January 3, 2009.
[15] T. Dann, K.H. Schulz, M. Mann, M. Collings, Appl. Catal. B 6 (1995) 1.
[16] J. Rodríguez-Mirasol, E. Ito, C.M. van den Bleek, L. Monceaux, P. Courtine, F. Kapteijn, J.A. Moulijn, in J.A. Pajares, J.M.D. Tascón (Eds.), Coal Science, Elsevier Science, Amsterdam, 1995, pp. 1911-1914.
[17] G. Centi, F. Vazzana, Catal. Today 53 (1999) 683.
[18] E. Sasaoka, N. Sada, K. Hara, Md. Azhar Uddin, Y. Sakata, Ind. Eng. Chem. Res. 38 (1999) 1335.
[19] T. Shimizu, M. Hasegawa, M. Inagaki, Energy Fuels 14 (2000) 104.
[20] G. Centi, S. Perathoner, F. Vazzana, M. Marella, M. Tomaselli, M. Mantegazza, Adv. Environ. Res. 4 (2000) 325.
[21] J. Pérez-Ramírez, F. Kapteijn, G. Mul, J.A. Moulijn, Appl. Catal. B 35 (2002) 227.
[22] E. Ruiz-Martínez, J.M. Sánchez-Hervás, J. Otero-Ruiz, Appl. Catal. B 50 (2004) 195.
[23] E. Ruiz-Martínez, J.M. Sánchez-Hervás, J. Otero-Ruiz, Appl. Catal. B 61 (2005) 306.
[24] J. Pérez-Ramírez, M.A.G. Hevia, S. Abelló, Chem. Commun. (2008) 5351.
[25] M. Santiago, M.S. Yalfani, J. Pérez-Ramírez, J. Mater. Chem. 16 (2006) 2886.
[26] J. Pérez-Ramírez, G. Mul, F. Kapteijn, J.A. Moulijn, A.R. Overweg, A. Doménech, A.Ribera, I.W.C.E. Arends, J. Catal. 207 (2002) 113.
[27] J. Pérez-Ramírez, F. Kapteijn, J.C. Groen, A. Doménech, G. Mul, J.A. Moulijn, J. Catal. 214 (2003) 33.
[28] J. Pérez-Ramírez, J. Catal. 227 (2004) 512.
[29] A. Bahillo, J.M. Sánchez-Hervás, CIEMAT Madrid, personal communication, 2008.
[30] J. Pérez-Ramírez, F. Kapteijn, G. Mul, J.A. Moulijn, Chem. Commun. (2001) 693.
[31] J. Pérez-Ramírez, F. Kapteijn, G. Mul, J.A. Moulijn, J. Catal. 208 (2002) 211.
[32] J. Pérez-Ramírez, M. Santosh Kumar, A. Brückner, J. Catal. 223 (2004) 13.
[33] G.E. Marnellos, E.A. Efthimiadis, I.A. Vasalos, Appl. Catal. B 46 (2003) 523.
[34] J. Pérez-Ramírez, F. Kapteijn, J.A. Moulijn, Catal. Lett. 60 (1999) 133.
[35] F. Kapteijn, G. Mul, G. Marbán, J. Rodríguez-Mirasol, J.A. Moulijn, Stud. Surf. Sci. Catal. 101 (1996) 641.
[36] A.J.S. Mascarenhas, H.M.C. Andrade, React. Kinet. Catal. Lett. 64 (1998) 215.
[37] S. Hodjati, C. Petit, V. Pitchon, A. Kiennemann, Appl. Catal. B 30 (2001) 247.
[38] P.T. Fanson, M.R. Horton, N.W. Delgass, J. Lauterbach, Appl. Catal. B 46 (2003) 393.
[39] K.-I. Shimizu, T. Higashimata, M. Tsuzuki, A. Satsuma, J. Catal. 239 (2006) 117.
[40] J. Beckers, L.M. van der Zande, G. Rothenberg, ChemPhysChem 7 (2006) 747.
[41] A.M. Venezia, R. Murania, G. Pantaleo, G. Deganello, J. Catal. 251 (2007) 94.

UNIVERSITAT ROVIRA I VIRGILI
HEXAALUIMINATE-TYPE CATALYSTS FOR N2O ABATEMENT
Marta Santiago Redondo
ISBN:978-84-693-8864-8/DL:T.1943-2010

UNIVERSITAT ROVIRA I VIRGILI
HEXAALUIMINATE-TYPE CATALYSTS FOR N2O ABATEMENT
Marta Santiago Redondo
ISBN:978-84-693-8864-8/DL:T.1943-2010

Chapter 6

Mechanism and micro-kinetics of direct N_2O decomposition over $BaFeAl_{11}O_{19}$ hexaaluminate

Mechanistic and kinetic aspects of direct N_2O decomposition over $BaFeAl_{11}O_{19}$ hexaaluminate were investigated in the Temporal Analysis of Products (TAP) reactor and compared with those previously determined for Fe-MFI zeolites. The catalysts were chosen due to their de-N_2O operation in significantly different temperature regimes. Several micro-kinetic models were evaluated for describing the transient responses of N_2O, N_2, and O_2 obtained in N_2O pulse experiments at 823-973 K. Thorough statistical discrimination enabled us to conclude that the preferred models of N_2O decomposition over $BaFeAl_{11}O_{19}$ and Fe-MFI zeolites differ in the reaction pathways leading to O_2 and N_2. Gas-phase N_2 and O_2 are simultaneously formed over $BaFeAl_{11}O_{19}$ upon interaction of gas-phase N_2O with a bi-atomic surface oxygen (*-O_2) species. Contrarily, the formation of O_2 over Fe-MFI occurs via a sequence of three elementary heterogeneous steps and limits the overall rate of N_2O decomposition. Despite the easy O_2 formation, $BaFeAl_{11}O_{19}$ is less active for N_2O decomposition below 973 K than the Fe-MFI zeolites due to the low coverage by *-O_2. According to our quantitative micro-kinetic analysis, this species is formed when gas-phase N_2O reacts with a mono-atomic oxygen (*-O) species. This reaction pathway is strongly influenced by the degree of isolation of iron species. The higher the degree of iron isolation in the catalyst, the lower the de-N_2O activity.

This chapter is based on the following publication:
E.V. Kondratenko, V.A. Kondratenko, M. Santiago, J. Pérez-Ramírez, Appl. Catal. B 99 (2010) 66.

1. Introduction

In recent years, a number of bulk and supported mixed-metal oxides as well as metal-loaded zeolites have been implemented for catalytic N_2O removal from the off-gases of adipic and nitric acid production plants, the main sources of this harmful gas in the chemical industry [13]. Iron-containing zeolites (particularly Fe-ZSM-5) are probably the most extensively studied catalytic materials because they reveal outstanding activity and stability for N_2O removal in the presence of typical off-gas components (O_2, NO_x, and H_2O) [4-6]. These catalytic features stimulated many studies for elucidating the nature of iron species active in N_2O decomposition [7-13] as well as for deriving reaction mechanisms and kinetics [11,14-25].

Several reaction schemes have been suggested for direct N_2O decomposition over Fe-MFI zeolites [1,14,25]. They differ in the pathways leading to N_2 and O_2. N_2O decomposition is initiated by the interaction of gas-phase N_2O with an active iron site resulting in the gas-phase N_2 and adsorbed oxygen species (*-O). The formation of O_2 was originally explained either by (i) recombination of two *-O species [14] or by (ii) direct reaction of gas-phase N_2O with *-O [15]. Recent micro-kinetic schemes derived from Density Functional Theory (DFT) simulations [20-22] and transient studies in the Temporal Analysis of Products (TAP) reactor [23-25] revealed that the mechanism of O_2 formation comprises a more complex sequence of elementary reaction steps: (i) N_2O reacts with an active oxygen species (*-O) yielding an intermediate bi-atomic oxygen species (O-*-O), (ii) the latter species reorganizes into another bi-atomic form (*-O_2), (iii) *-O_2 desorbs as gas-phase O_2 regenerating the active site. TAP studies [23-25] proved that the reaction mechanism was neither influenced by the nature of the iron species in the zeolite (isolated *vs.* oligomeric), the composition of the MFI framework (ZSM-5 *vs.* silicalite), nor by the method of iron incorporation (hydrothermal synthesis followed by steam activation *vs.* liquid-ion exchange). Moreover, the TAP-derived micro-kinetic model was extrapolated to a wide range of partial N_2O pressures (0.0115 kPa) and temperatures (473-873 K). As a result, differences in the steady-state de-N_2O performance of zeolite samples with different iron speciation could be qualitatively predicted.

Fe-MFI zeolites find industrial application for N_2O decomposition in the tail gases of nitric acid plants [2], operating optimally in the temperature range of 673-773 K.

Process-gas N_2O decomposition in the ammonia burner is also industrially applied as a cost-effective, robust, and versatile technology for N_2O abatement in this source. In this case, suitable catalysts are located directly under Pt-Rh gauzes and typically operate above 1073 K. They must possess high chemical stability to withstand the demanding conditions inside the ammonia burner (high-temperature, wet oxidizing atmosphere). $LaCoO_3$ perovskite and CeO_2-supported Co_2AlO_4 have been successfully implemented in large scale [2], although other families of mixed oxides proved to be active and stable in laboratory tests [26-33]. However, very little studies have addressed the mechanism of N_2O decomposition over catalysts operating at high temperatures (>873 K). Exceptionally, Ivanov *et al*. [34] studied the direct N_2O decomposition using the Steady-State Isotopic Transient Kinetic Analysis (SSITKA) and highlighted the importance of oxygen mobility for the de-N_2O activity over La-Sr-Mn perovskite-type oxides.

To the best of our knowledge, no studies have established mechanistic analogies and differences in direct N_2O decomposition over catalysts operating in high (>873 K) and low-temperature (<723 K) regimes. Herein, we have carried out a detailed mechanistic and micro-kinetic analysis of N_2O decomposition over $BaFeAl_{11}O_{19}$ hexaaluminate using the TAP reactor and the mathematical approach applied earlier for the study of N_2O decomposition over iron-containing zeolites [23-25]. The aim of this analysis was to identify mechanistic aspects governing the distinct de-N_2O performance of $BaFeAl_{11}O_{19}$ and Fe-MFI catalysts. This particular hexaaluminate was chosen due to its remarkable process-gas de-N_2O performance under simulated conditions of nitric acid plants [28,29].

2. Experimental

2.1. Catalyst

$BaFeAl_{11}O_{19}$ was prepared by coprecipitation of the corresponding precursors using the in-line dispersion precipitation (ILDP) method [35] followed by high-temperature calcination. An aqueous solution of the metal nitrates (0.1 M Ba, 0.1 M Fe, and 1.1 M Al) and a 2 M aqueous solution of $(NH_4)_2CO_3$ were pumped into a 6 ml reactor attached to a high-shear homogenizer rotating at 13,500 rpm. The pH of the slurry was

measured and controlled by an in-line probe directly at the outlet of the precipitation chamber. Coprecipitation was carried out at constant pH 8 with an average residence time of 18 s. The slurry was aged at 333 K for 3 h, filtered, washed thoroughly, and dried at 353 K for 12 h. The resulting solid was calcined in static air at 1473 K for 10 h using a heating rate of 5 K min^{-1}. Characterization of the catalyst by ICP-OES, X-ray diffraction, and N_2 adsorption was presented elsewhere [29]. The molar metal ratios in the mixed oxide were very close to the nominal values. The sample showed hexaaluminate ($BaFeAl_{11}O_{19}$, JCPDS 26-135) as the only crystalline phase and possessed a total surface area (S_{BET}) of 12 $m^2 g^{-1}$.

2.2. Continuous flow catalytic tests at ambient pressure

Steady-state N_2O decomposition tests were carried out in a Micro Activity Reference setup (PID Eng&Tech) using a quartz micro-reactor (9 mm i.d.). The catalyst (100 mg, sieve fraction 125-300 μm) was loaded between two layers of quartz wool and rested over a porous frit. The sample was pre-treated in He at 673 K for 1 h and cooled down to the initial reaction temperature (473 K). Then, the feed mixture (1.5 mbar N_2O in He) was introduced into the reactor with a space velocity of 60,000 ml g^{-1} h^{-1}. The temperature was increased at intervals of 50 K up to 973 K, using a heating rate of 5 K min^{-1} and keeping an isothermal period of 30 min at each set point. In this period, constant conversion levels were obtained and can be considered as the steady state. Reactant and product gases were analyzed by on-line gas chromatography (Agilent 6890N).

2.3. Transient experiments in vacuum

Direct N_2O decomposition was investigated in the Temporal Analysis of Products (TAP-2) reactor, a transient pulse technique operating in vacuum with sub-millisecond time resolution [36,37]. The $BaFeAl_{11}O_{19}$ sample (20 mg, sieve fraction of 250-350 μm) was packed within the isothermal zone of the quartz micro-reactor (40 mm length and 6 mm i.d.) between two layers of quartz particles of the same sieve fraction. The catalyst was pre-treated in flowing O_2 (30 ml STP min^{-1}) at 1023 K and atmospheric pressure for 1 h, followed by exposure to vacuum (10^{-5} Pa), and cooling down to 823 K.

Thereafter, a mixture of N_2O:Ne = 1:1 was pulsed in the temperature range of 823-973 K with 50 K intervals, starting from 823 K. The ramping from one temperature to the next one was performed in vacuum. *Ca.* 30 min after each set point was reached, the catalyst was pre-treated using large N_2O pulses (*ca.* 10^{16} molecules) in order to recover surface oxygen species, which could have partially desorbed under vacuum conditions. Thereafter, low-sized N_2O pulses ($5 \cdot 10^{14}$-$1 \cdot 10^{15}$ molecules) were injected into the micro-reactor. These experiments were used for micro-kinetic analysis of N_2O decomposition. Under these conditions, Knudsen diffusion describes the gas transport inside the reactor and the transient responses are a function of gas-solid interactions, *i.e.* they are not influenced by molecular collisions in the gas phase.

A quadrupole mass spectrometer (HAL RC 301 Hiden Analytical) was used for quantitative analysis of reactants and reaction products. The transient responses at the reactor outlet were monitored at the following atomic mass units (AMUs): 44 (N_2O), 32 (O_2), 30 (N_2O, NO), 28 (N_2, N_2O), and 20 (Ne). In the experiments, 10 pulses for each AMU were averaged in order to improve the signal-to-noise ratio. The concentrations of feed components and reaction products were determined from the corresponding AMUs using standard fragmentation patterns and sensitivity factors according to [25].

2.4. Kinetic evaluation of transient experiments

The parameter estimation procedure used here was reported elsewhere [38,39]. Briefly, it is based on a numerical solution of partial differential equations (PDEs) describing diffusion, adsorption, desorption, and reaction in the TAP micro-reactor. PDEs were transformed into coupled ordinary differential equations (ODEs) by spatial approximation and then integrated numerically using the PDEONE routine [40]. Parameters (rate and diffusion coefficients) were determined using first a genetic algorithm to find good starting values [41] and then the Nelder-Mead simplex algorithm [42]. The TAP micro-reactor was described as a one-dimensional pseudo-homogeneous system divided into three zones, which are represented by the catalyst and the two layers of inert material, where the catalyst was sandwiched.

Table 1. Micro-kinetic models evaluated in this work.

Model	Elementary reaction steps	
1	$N_2O + * \rightarrow N_2 + *\text{-}O$	(1.1)
	$*\text{-}O + *\text{-}O \rightarrow O_2 + 2*$	(1.2)
2	$N_2O + * \rightarrow N_2 + *\text{-}O$	(2.1)
	$N_2O + *\text{-}O \rightarrow N_2 + O_2 + *$	(2.2)
3	$N_2O + * \rightarrow N_2 + *\text{-}O$	(3.1)
	$*\text{-}O + *\text{-}O \rightarrow *\text{-}O_2 + *$	(3.2)
	$*\text{-}O_2 \rightarrow O_2 + *$	(3.3)
4	$N_2O + * \rightarrow N_2 + *\text{-}O$	(4.1)
	$N_2O + *\text{-}O \rightarrow N_2 + *\text{-}O_2$	(4.2)
	$N_2O + *\text{-}O_2 \rightarrow N_2 + O\text{-}*\text{-}O_2$	(4.3)
	$O\text{-}*\text{-}O_2 \rightarrow O_2 + *\text{-}O$	(4.4)
	$*\text{-}O_2 \rightarrow O_2 + *$	(4.5)
5	$N_2O + * \rightarrow N_2 + *\text{-}O$	(5.1)
	$N_2O + *\text{-}O \rightarrow N_2 + *\text{-}O_2$	(5.2)
	$N_2O + *\text{-}O_2 \rightarrow N_2 + *\text{-}O + O_2$	(5.3)
	$*\text{-}O_2 \rightarrow O_2 + *$	(5.4)
	$O_2 + * \rightarrow *\text{-}O_2$	(5.5)
6	$N_2O + * \rightarrow N_2 + *\text{-}O$	(6.1)
	$N_2O + *\text{-}O \rightarrow N_2 + *\text{-}O_2$	(6.2)
	$*\text{-}O_2 \rightarrow O_2 + *$	(6.3)
	$*\text{-}O + *\text{-}O \rightarrow 2* + O_2$	(6.4)
7	$N_2O + * \rightarrow N_2 + *\text{-}O$	(7.1)
	$N_2O + *\text{-}O \rightarrow N_2 + *\text{-}O_2$	(7.2)
	$*\text{-}O_2 \rightarrow O_2 + *$	(7.3)
	$*\text{-}O + *\text{-}O \rightarrow *\text{-}O_2 + *$	(7.4)
	$*\text{-}O_2 + * \rightarrow *\text{-}O + *\text{-}O$	(7.5)
8	$N_2O + * \rightarrow N_2 + *\text{-}O$	(8.1)
	$N_2O + *\text{-}O \rightarrow N_2 + *\text{-}O_2$	(8.2)
	$N_2O + *\text{-}O_2 \rightarrow N_2 + *\text{-}O_3$	(8.3)
	$*\text{-}O_2 \rightarrow O_2 + *$	(8.4)
	$*\text{-}O_3 \rightarrow *\text{-}O + O_2$	(8.5)
9	$N_2O + * \rightarrow N_2 + *\text{-}O$	(9.1)
	$N_2O + *\text{-}O \rightarrow N_2 + O\text{-}*\text{-}O$	(9.2)
	$O\text{-}*\text{-}O \rightarrow *\text{-}O_2$	(9.3)
	$*\text{-}O_2 \rightarrow O_2 + *$	(9.4)

The transport of gaseous compounds was described by Knudsen diffusion along the reactor axis. Experimental transient responses of N_2O, O_2, and N_2 were simultaneously used for the fitting procedure. The N_2 response was corrected with respect to the contribution of the N_2O response according to the fragmentation patterns determined upon pulsing of N_2O:Ne = 1:1 over SiO_2 particles (inert bed). Each response was described by representative points as reported elsewhere [39]. The goodness of the fit was determined by an objective function defined as the sum of squares of the shortest deviations between the respective pairs of points of the experimental and simulated transient responses [39]. For the best kinetic model, we have performed both sensitivity and correlation analysis in order to validate the kinetic parameters. In the

$$k_{T_i} = k_{Tref} \bullet \exp\left(-\frac{E_a}{R} \bullet \left(\frac{1}{T_i} - \frac{1}{T_{ref}} \right) \right)$$

sensitivity analysis, each parameter was varied until the objective function decreased by 10%.

The micro-kinetic models of direct N_2O decomposition evaluated in this work are listed in Table 1. Based on the results of the model discrimination at a reference temperature (T_{ref}) of 923 K, the best model was selected for simultaneous fitting of the transient responses at other temperatures. To avoid the correlation between activation energies and pre-exponential factors [43,44], activation energies for all elementary reaction steps were derived according to the equation:

where T_{ref} and k_{Tref} are the reference temperature and the rate coefficient at this temperature, respectively.

UNIVERSITAT ROVIRA I VIRGILI
HEXAALUIMINATE-TYPE CATALYSTS FOR N2O ABATEMENT
Marta Santiago Redondo
ISBN:978-84-693-8864-8/DL:T.1943-2010

3. Results and discussion

3.1. N_2O decomposition under steady-state ambient pressure and vacuum transient conditions

Figure 1 compares the N_2O conversion under vacuum transient and ambient pressure steady-state conditions. A higher de-N_2O activity in vacuum can be tentatively explained by the partial reduction of the catalyst surface, increasing the number of oxygen vacancies, which are potential active sites for N_2O decomposition. There are several studies highlighting the importance of high-temperature catalyst treatment (in vacuum, inert atmosphere, steam, or hydrogen) for increasing the de-N_2O activity. Originally, Panov and co-workers [9] reported that such treatment of Fe-MFI zeolites results in the reduction of Fe^{3+} to Fe^{2+}, which forms the so-called α-sites. Berrier *et al.* [13] demonstrated that the concentration of active oxygen species formed upon N_2O

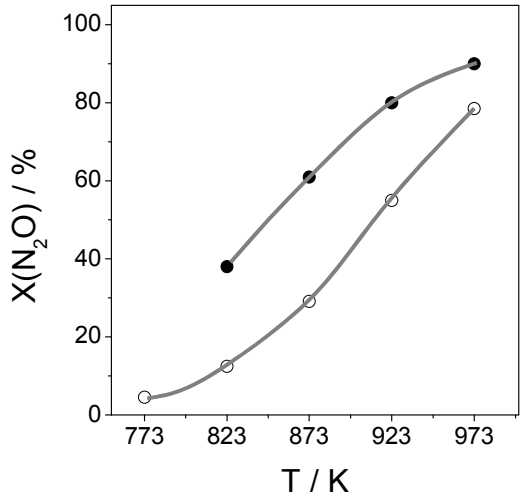

Figure 1. N_2O conversion *vs.* temperature over $BaFeAl_{11}O_{19}$ under (○) ambient pressure steady-state tests in a continuous flow reactor and (●) vacuum transient conditions in the TAP reactor.

decomposition over Fe-MFI zeolites increased when the temperature of catalyst pre-reduction in flowing H_2 raised from 673 to 873 K. Similar results were reported for Fe-FER and Fe-BEA, when the catalysts were treated in Ar at 723 and 923 K [45]. Centi *et*

al. [46] observed an increase in the de-N_2O activity of Rh and Ni-containing catalysts after their reduction in an H_2 flow at 773 K. They suggested that the reduction of metal oxides to metals resulted in an increase in the initial de-N_2O activity.

Our further discussion focuses on the analysis and kinetic evaluation of transient N_2O decomposition experiments by temporal analysis of products. Following our previous approach applied for metal-loaded zeolites [25], model-free mechanistic insights into N_2O decomposition over $BaFeAl_{11}O_{19}$ hexaaluminate were derived from the analysis of the order of appearance and the shapes of the height-normalized transient responses of N_2O, N_2, and O_2 (Figure 2). For example, the times of the maximal concentration (t_{max}) of N_2 (0.072 s) and O_2 (0.075 s) at 873 K are very close to each other but they are significantly higher than the t_{max} value of N_2O (0.045 s). The similarity of the t_{max} of N_2 and O_2 indicates that the reaction pathways leading to these products occur with similar rates. In contrast to the N_2 response, the O_2 response is characterized by a long tailing (slow decrease in the O_2 concentration with time). This tailing indicates that (i) the formed O_2 readsorbs over the catalyst and/or (ii) there are several elementary reaction pathways leading to gas-phase O_2.

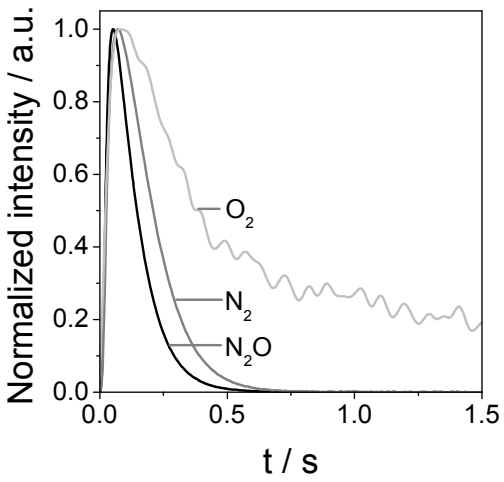

Figure 2. Normalized transient responses of N_2O, N_2, and O_2 upon N_2O pulsing over $BaFeAl_{11}O_{19}$ at 873 K (N_2O:Ne = 1:1, pulse size ~ 10^{15} molecules).

3.2. Micro-kinetic analysis

According to the theory of the TAP reactor [36,37], the shape and the order of appearance of the transient N_2O, N_2, and O_2 responses contain information about the mechanism and kinetics of N_2O decomposition. This information can be extracted from kinetic evaluation of these responses. In the present study, different micro-kinetic models listed in Table 1 were used and discriminated for simultaneous fitting of the reactant and products responses according to [38,39]. The models are based on previous experimental or DFT (density functional theory) results of N_2O decomposition over Fe-MFI zeolites. It is beyond the scope of our modeling approach to take the structure of the active sites and the charge of oxygen species formed from N_2O into consideration. Since no experimental insights into reversible N_2O adsorption could be derived from the present study, the first step of N_2O decomposition in all the applied models was described by the decomposition of gas-phase N_2O over a free surface site (*). This reaction yields gas-phase N_2 and mono-atomic *-O species. Subsequent reactions of this oxygen species, which could yield gas-phase O_2, were considered in the models. The formation of gas-phase O_2 in models 1 and 6 is described by direct recombination of two mono-atomic *-O species as suggested in [14,47]. O_2 formation via decomposition of a surface bi-atomic oxygen precursor originated by recombination of two mono-atomic *-O species is considered in models 3 and 7 [17,48,49]. Model 2 assumes a direct reaction of gas-phase N_2O with *-O leading to gas-phase O_2 [15]. This reaction pathway was modified in models 4, 5, and 8 by taking into account that surface bi-atomic or tri-atomic oxygen species are formed upon interaction of gas-phase N_2O with mono-atomic *O species or bi-atomic *-O_2 species, respectively, as suggested in [21,23,25]. Decomposition of surface *-O_2 species to gas-phase O_2 is considered in models 3, 5, 6-9.

For model discrimination, the fitting procedure was repeated at least three times with each model. Since a solution might be not found within the first fitting in an n-dimensional parameters space, the second and third fitting avoids wrong discarding of a model. The reaction scheme in model 5 provided the best description of all transient responses in the temperature range investigated (Figure 3). According to this model, a bi-atomic oxygen species is formed when N_2O decomposes over *-O. This species can be ascribed to a peroxo one and can be stabilized by the presence of barium in

UNIVERSITAT ROVIRA I VIRGILI
HEXAALUIMINATE-TYPE CATALYSTS FOR N2O ABATEMENT
Marta Santiago Redondo
ISBN:978-84-693-8864-8/DL:T.1943-2010

$BaFeAl_{11}O_{19}$. The formation of barium peroxide at high temperatures was proven experimentally in several studies [50-52]. The optimized values for kinetic parameters in model 5 are listed in Table 2.

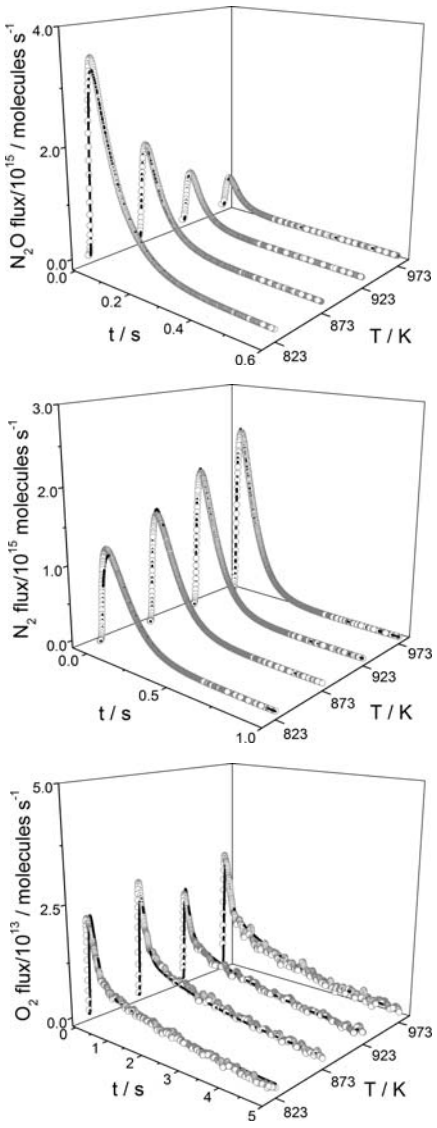

Figure 3. Experimental (symbols) and calculated (lines) transient responses of N_2O, N_2, and O_2 using model 5 in Table 1 for N_2O decomposition over $BaFeAl_{11}O_{19}$ at different temperatures.

Table 2. Best kinetic model and parameters of N_2O decomposition over $BaFeAl_{11}O_{19}$ derived from transient experiments in the TAP reactor*.

No	Elementary reaction steps	k^0 / s^{-1}	E_a / kJ mol^{-1}
1	$N_2O + * \rightarrow *\text{-}O + N_2$	1.3·106	137
2	$N_2O + *\text{-}O \rightarrow *\text{-}O_2 + N_2$	4.9·102	97
3	$N_2O + *\text{-}O_2 \rightarrow *\text{-}O + N_2 + O_2$	1.8·101	62
4	$*\text{-}O_2 \rightarrow O_2 + *$	2.0·100	10
5	$O_2 + * \rightarrow *\text{-}O_2$	1.6·104	173

*For steps 1-3, the pre-exponential factors are in Pa^{-1} s^{-1}.

It should be noted that k^0 values determined for reaction pathways 1 and 2 relate to the apparent kinetic constants ($k_i \times C_{total}$), since our modeling approach does not enable to determine independently the intrinsic reaction constants and the total number of surface sites. The low activation energy of O_2 formation via step 4 in Table 2 may be due to facilitated O_2 desorption in high vacuum. The kinetic parameters of model 5 were additionally validated by sensitivity and correlations analysis (section 2.4). The correlation coefficients between the individual parameters deviated significantly (at least by 10% for the kinetic constants for steps 2 and 3 in Table 2) from the boundary values of -1 and 1 characteristic for a straight correlation. The accuracy of the kinetic parameters for steps 1-4 was higher than 8% as derived from the sensitivity analysis. The error for the kinetic parameter for step 5 was higher than 100%. This is probably because the low dependence of N_2O decomposition on the partial O_2 pressure experimentally determined in [28,29] cannot be properly derived from low-pressure single N_2O pulse experiments in the present study. This previous experimental analysis reported only 40% decrease in the degree of N_2O conversion, when N_2O decomposition was investigated using a feed mixture with O_2/N_2O ratio = 7.

It is also important to stress that models 4, 7, and 8 contain the same number of parameters as model 5, but failed to correctly describe the N_2O, N_2, and O_2 transient responses. This fact supports that model 5 is suitable for N_2O decomposition from a mathematic point of view and physically also reflects the reaction mechanism over this catalyst. This model differs from that describing N_2O decomposition over Fe-MFI zeolites [23-25]. Section 3.4 discusses in detail these mechanistic differences with the aim to determine mechanistic origins of the distinctive de-N_2O activity of these catalysts.

In summary, the decomposition of N_2O over $BaFeAl_{11}O_{19}$ proceeds via interaction of gas-phase N_2O with free (*) Fe sites as well as with Fe sites occupied by mono (*-O) and biatomic (*-O_2) oxygen species originated from N_2O decomposition. All these iron sites were considered to be active for N_2O decomposition over Fe-MFI zeolites, too [20-25]. Gas-phase O_2 is formed via decomposition of the bi-atomic oxygen species (step 4 in Table 2) or their reaction with gas-phase N_2O (step 3 in Table 2). These reaction pathways were discussed for direct N_2O decomposition over Rh-ZSM-5 [25] and Fe-ZSM-5 [20-22], respectively. Since the activation energies of O_2 formation are lower than those of N_2 formation via steps 1 and 2 in Table 2 as well as O_2 and N_2 are simultaneously formed via step 3 in Table 2, it is put forward that the decomposition of N_2O over $BaFeAl_{11}O_{19}$ is not limited by O_2 desorption. This conclusion from micro-kinetic modeling is supported by experiments in Figure 2; O_2 and N_2 appear at the reactor outlet after very similar times upon N_2O pulsing.

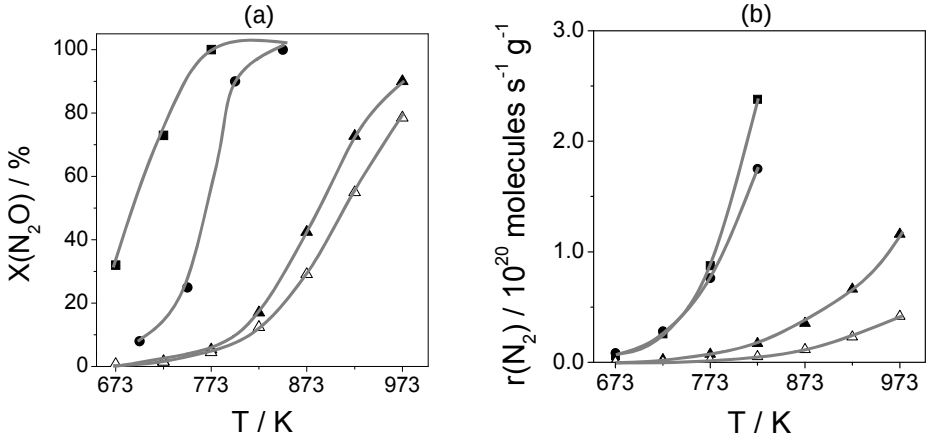

Figure 4. De-N_2O performance of (△) $BaFeAl_{11}O_{19}$, (▲) Fe-silicalite(st), (●) Fe-ZSM-5(st), and (■) Fe-ZSM-5(lie) *vs.* temperature: (a) N_2O conversion determined experimentally [10,28], and (b) rates of N_2 formation calculated with the kinetic parameters from Tables 2 and 3.

3.3. Model validation and analysis

As discussed above, model 5 correctly describes the experimental data of N_2O decomposition over $BaFeAl_{11}O_{19}$ under transient conditions. In order to validate this model, we calculated the rates of N_2O decomposition under steady-state conditions

using kinetic parameters derived from the fitting of TAP responses (Table 2) and compared these rates with those of N_2O decomposition over Fe-MFI zeolites. For the latter catalysts, the micro-kinetic model and the respective parameters were taken from our previous works [23,25]. These studies proved that the TAP-derived kinetics of N_2O decomposition predicted correctly the steady-state performance. Similar to the iron-containing zeolite catalysts, the rate of N_2O decomposition over $BaFeAl_{11}O_{19}$ increases linearly with the partial N_2O pressure (first-order dependence). In contrast to previous results of N_2O decomposition over the same hexaaluminate under flow conditions at ambient pressure [28,29], our micro-kinetics predicts too low negative effect of O_2 on the rate of N_2O decomposition. A possible reason for this discrepancy was discussed in the preceding section.

The rates of N_2O decomposition were calculated in the temperature range of 673-973 K and partial N_2O pressure of 150 Pa. As shown in Figure 4b, all the rates increase with temperature. It is also clearly seen that our calculations predict the lowest activity of $BaFeAl_{11}O_{19}$ and the different activity of the Fe-MFI zeolites. A similar activity order is also valid for experimentally determined N_2O conversion over all these catalysts under steady-state conditions at partial N_2O pressure of 150 Pa (Figure 4a).

In order to elucidate the contribution of empty sites (*) as well as *-O, and *-O_2 species to the overall rate of N_2O decomposition over $BaFeAl_{11}O_{19}$ under steady-state conditions, the surface coverage by these species at different temperatures and partial N_2O pressures were computed with the kinetic parameters in Table 2. Figure 5 illustrates the coverage by these species during steady-state N_2O decomposition at 873, 973, and 1073 K. The partial N_2O pressure was in the range of 1-1000 Pa representing the profile of N_2O concentration along the catalyst bed used for N_2O decomposition in the nitric acid plants. Mono-atomic oxygen (*-O) is the dominant species in the whole range of N_2O partial pressures. Its coverage slightly decreases with an increase in temperature. The coverage by *-O_2 continuously increases with temperature and N_2O partial pressure, while the coverage by free active sites (*) decreases. The steady-state simulation predicts that the *-O and *-O_2 are major active species participating in the formation of N_2 from N_2O. Concerning the formation of gas-phase O_2, it is suggested that it is predominantly formed via the interaction of gas-phase N_2O and *-O_2 (step 3 in Table 2). Decomposition of *-O_2 to gas-phase O_2 (step 4

UNIVERSITAT ROVIRA I VIRGILI
HEXAALUIMINATE-TYPE CATALYSTS FOR N2O ABATEMENT
Marta Santiago Redondo
ISBN:978-84-693-8864-8/DL:T.1943-2010

in Table 2) plays a role at low partial N_2O pressures and temperatures. This is due to the fact that the O_2 formation via step 3 is influenced by the partial N_2O pressure and has significantly higher activation energy than O_2 formation via step 4.

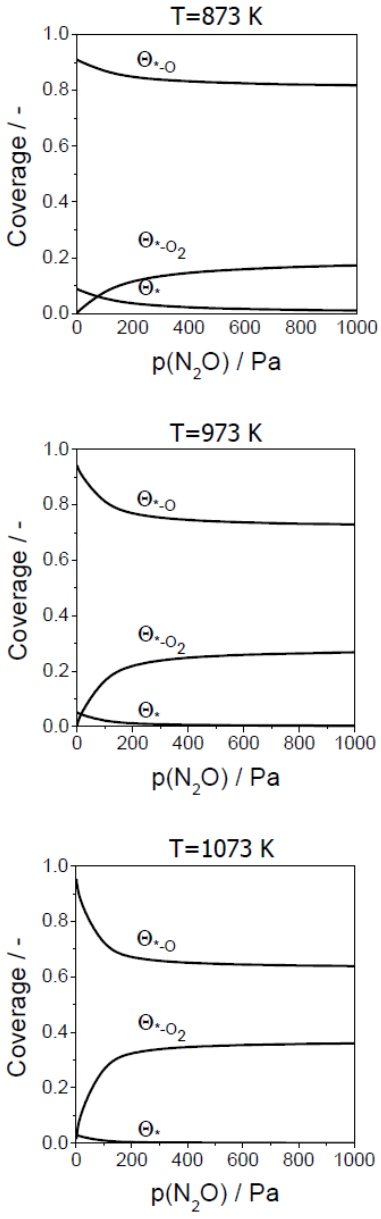

Figure 5. Calculated steady-state coverage by surface species upon N_2O decomposition over $BaFeAl_{11}O_{19}$ at different temperatures for inlet N_2O partial pressures in the range of 1-1000 Pa. Kinetic parameters for the calculation were taken from Table 2.

In order to derive insights into the nature of active species during N_2O decomposition under vacuum transient conditions, we calculated temporal and spatial coverages by surface oxygen species during N_2O pulse experiments in the TAP reactor. In agreement with the steady-state experiments, mono-atomic oxygen (*-O) is also the dominant species under transient conditions. At similar partial N_2O pressures, the coverage by *-O_2 is, however, higher in the TAP experiments than in ambient pressure steady-state conditions. Since these bi-atomic oxygen species disappear via reaction with gas-phase N_2O, this difference in the coverage can be due to a lower contribution of this reaction pathway to the overall N_2O decomposition at low partial N_2O partial pressures (peak pressure in the TAP experiments was below 5 Pa). This conclusion is supported by our calculations of the steady-state rates of N_2 formation over various active sites at different partial N_2O pressures. These rates over free (*) and mono-atomic oxygen species (*-O) at 873 K are higher than that over *-O_2 at pressures below 100 Pa. While the contribution of *-O_2 towards N_2O decomposition increases with temperature, that of free sites decreases.

3.4. Effect of FeO_x species and host matrix on the de-N_2O activity

Finally, we shall discuss the derived micro-kinetics for identifying mechanistic origins of the distinct de-N_2O activity of $BaFeAl_{11}O_{19}$ and Fe-MFI catalysts [23-25]. Along the manuscript, the zeolites are denoted as Fe-silicalite(st), Fe-ZSM-5(st), and Fe-ZSM-5(lie). They differ in the method of iron incorporation, *i.e.* liquid-ion exchange (lie), and hydrothermal synthesis followed by calcination and steam treatment (st). For all the catalysts investigated, the TAP-derived micro-kinetic schemes of N_2O decomposition predict that both free active sites (*) and sites occupied by mono-atomic oxygen species (*-O) participate in N_2O decomposition. In addition, *-O_2 species formed over $BaFeAl_{11}O_{19}$ via an interaction of *-O with N_2O (step 3 in Table 2) are also active sites for N_2O decomposition. Gas-phase N_2O directly decomposes over all the above sites.

The calculated activation energies (E_a) of N_2O decomposition over free active sites (*) on $BaFeAl_{11}O_{19}$, Fe-silicalite(st), and Fe-ZSM-5(lie) are 137, 120, and 130 kJ mol^{-1},

respectively (Table 2 and Table 3). Such close values of Ea indicate that the strength of the nitrogen-oxygen bond in the N_2O molecule mainly determines the energy cost

Table 3. Best kinetic model and parameters of N_2O decomposition over $BaFeAl_{11}O_{19}$ derived from transient experiments in the TAP reactor*.

No	Elementary reaction steps	Fe-silicalite(st)		Fe-ZSM-5(lie)		Fe-ZSM-5(st)	
		$k^0(s^{-1})$	E_a(kJ mol^{-1})	$k^0(s^{-1})$	E_a(kJ mol^{-1})	$k^0(s^{-1})$	E_a(kJ mol^{-1})
1	$N_2O + * \rightarrow *\text{-}O + N_2$	$3.4\cdot10^5$	120	$4.1\cdot10^6$	130	$6.3\cdot10^2$	69
2	$N_2O + *\text{-}O \rightarrow O\text{-}*\text{-}O + N_2$	$1.4\cdot10^2$	81	$2.9\cdot10^5$	112	$2.3\cdot10^4$	98
3	$O\text{-}*\text{-}O \rightarrow *\text{-}O_2$	$9.6\cdot10^{20}$	300	$2.5\cdot10^4$	61	$3.8\cdot10^{10}$	142
4	$*\text{-}O_2 \rightarrow O_2 + *$	$4.4\cdot10^8$	125	$8.9\cdot10^8$	58	$2.1\cdot10^4$	50

*For reaction pathways 1 and 2, the pre-exponential factors are in $Pa^{-1}\ s^{-1}$.

required for N_2 formation. However, in contrast to Fe-silicalite(st) possessing surface isolated iron species [53], the activation energy of N_2O decomposition (69 kJ mol^{-1} in Table 3) decreases over FeZSM-5(st), containing also oligonuclear FeO_x species. This may be a reason for the improving effect of high-temperature steaming on the de-N_2O activity of Fe-MFI zeolites particularly below 673 K [10].

The activation energy of N_2O decomposition over *-O is in the range of 81-112 kJ mol^{-1}. However, the pre-exponential factor (k^0), *i.e.* the collision frequency of N_2O with *-O species, is strongly influenced by the type of iron species in the catalyst. These factors for Fe silicalite(st), Fe-ZSM-5(st), and Fe-ZSM-5(lie) are 1.4 x 10^2 $Pa^{-1}s^{-1}$, 2.3 x 10^4 $Pa^{-1}s^{-1}$, and 2.9 x 10^5 $Pa^{-1}s^{-1}$, respectively (Table 3). The corresponding value for $BaFeAl_{11}O_{19}$ is 4.9 x 10^2 $Pa^{-1}s^{-1}$ and very close to that for Fe-silicalite(st). The intrinsic structure of iron species in Fe-silicalite and $BaFeAl_{11}O_{19}$ is remarkably different. Iron sites in the hexaaluminate are shielded in a crystalline framework, while isolated iron species in the zeolite are ionic species in extra-framework (ion-exchange) positions [53]. Despite these large structural differences, the degree of clustering of iron species in these both materials is very low, *i.e.* these species should not possess Fe-O-Fe bonds. It is important to mention that the pre-exponential factor of N_2O decomposition over *-O species increases with an increase in the degree of clustering of FeO_x species on the surface of Fe-ZSM-5(st), and Fe-ZSM-5(lie). In other words, we suggest that the degree of clustering of surface and bulk FeO_x species in the zeolites and hexaaluminate, respectively, influences the collision frequency of N_2O with *-O species.

An important mechanistic difference between $BaFeAl_{11}O_{19}$ and Fe-MFI relates to the pathways for O_2 formation. There are two parallel reaction pathways of O_2 formation over $BaFeAl_{11}O_{19}$: (i) N_2O interacts with a surface bi-atomic oxygen species (*-O_2) yielding gas-phase O_2 and N_2 and (ii) *-O_2 can decompose to gas-phase O_2. Our micro-kinetic analysis and experimental results in Figure 2 suggest the simultaneous formation of gas-phase O_2 and N_2 over $BaFeAl_{11}O_{19}$, *i.e.* option (i). Contrarily, the decomposition of N_2O over Fe-MFI materials is limited by the evolution of gas-phase O_2. It occurs via a complex sequence of three elementary reaction pathways: (i) N_2O reacts with an active oxygen species (*-O) yielding an adsorbed bi-atomic oxygen species (O-*-O), (ii) the formed bi-atomic oxygen species intermediate reorganizes into another bi-atomic one (*-O_2), and (iii) *-O_2 desorbs as O_2 generating free iron site. The micro-kinetics predicts that the degree of isolation of surface FeO_x species strongly influences the activation energy of the rearrangement of an adsorbed bi-atomic oxygen species to another one; the higher the degree of iron clustering, the easier is this rearrangement. This is probably a reason for higher de-N_2O activity of oligonuclear FeO_x species compared to isolated ones in Fe-MFI zeolites. However, the iron clustering should be optimised in order to avoid the formation of iron oxide particles, which lower the de-N_2O activity [10].

In summary, the lower de-N_2O activity of $BaFeAl_{11}O_{19}$ compared to Fe-MFI below 823 K can be explained as follows. According to our micro-kinetics, the overall rate of N_2O decomposition is limited by the interactions of gas-phase N_2O with iron sites possessing mono-and bi-atomic oxygen species (*-O, and *-O_2). The activity of these steps can be improved by increasing the degree of clustering of iron sites within the structure of the hexaaluminate that would imply having more iron in the hexaaluminate, *i.e.* by substituting more aluminium by iron in the structure. If this would be possible, Fe-hexaaluminates may approach the temperature of Fe-MFI materials in de-N_2O applications because in contrast to the latter catalysts the overall rate of N_2O decomposition over Fe-hexaaluminate is not limited by the formation of O_2.

4. Conclusions

The micro-kinetics of high-temperature direct N_2O decomposition over $BaFeAl_{11}O_{19}$ hexaaluminate was derived from quantitative evaluation of N_2O pulse experiments in the Temporal Analysis of Products (TAP) reactor. It was demonstrated that this approach can be successfully applied to any N_2O decomposition catalysts, covering the low and high-temperature regimes. The best kinetic model obtained via thorough statistical discrimination of several micro-kinetic schemes consists of five elementary steps. N_2O decomposes over free iron sites as well as over iron sites with mono-and bi-atomic oxygen species originated from N_2O. The latter reaction pathway produces simultaneously gas-phase O_2 and N_2. The model was validated by its extrapolating to steady-state ambient pressure conditions and by comparing the steady-sate de-N_2O activity of $BaFeAl_{11}O_{19}$ with that of Fe-MFI zeolites. This also enabled us to derive mechanistic origins of distinctive catalytic activity of Fe-MFI zeolites with differently clustered FeO_x species and $BaFeAl_{11}O_{19}$. Irrespective of the matrix for iron species, the degree of clustering of these sites favours the formation of gas-phase O_2; the higher the clustering, the easier is the formation. The nature of iron species fulfils a double role: (i) it influences the collision frequency of N_2O with iron sites in the $BaFeAl_{11}O_{19}$ hexaaluminate and in Fe-MFI zeolites and (ii) it decreases the activation energy of the rearrangement of an adsorbed bi-atomic oxygen species to another one in Fe-MFI.

5. Acknowledgements

Evgenii Kondratenko and Vita Kondratenko are gratefully acknowledged for their cooperation in this chapter.

References

[1] F. Kapteijn, J. Rodríguez-Mirasol, J.A. Moulijn, Appl. Catal. B 9 (1996) 25.
[2] J. Pérez-Ramírez, F. Kapteijn, K. Schöffel, J.A. Moulijn, Appl. Catal. B 44 (2003) 117.
[3] A. Shimizu, K. Tanaka, V. Fujimori, Chemosphere, 2 (2000) 425.
[4] J. Pérez-Ramírez, F. Kapteijn, G. Mul, J.A. Moulijn, Chem. Commun. (2001) 693.
[5] J. Pérez-Ramírez, F. Kapteijn, G. Mul, X. Xu, J.A. Moulijn, Catal. Today 76 (2002) 55.
[6] M. Santiago, M.A.G. Hevia, J. Pérez-Ramírez, Appl. Catal. B 90 (2009) 83.
[7] M. Kögel, R. Monnig, W. Schwieger, A. Tissler, T. Turek, J. Catal. 182 (1999) 470.
[8] G. Centi, L. Dall'Olio, S. Perathoner, Appl. Catal. A 79 (2000) 194.

[9] K.A. Dubkov, N.S. Ovanesyan, A.A. Shteinman, E.V. Starokon, G.I. Panov, J. Catal. 207 (2002) 341.
[10] J. Pérez-Ramírez, F. Kapteijn, J.C. Groen, A. Doménech, G. Mul and J.A. Moulijn, J. Catal. 214 (2003) 33.
[11] L. Kiwi-Minsker, D.A. Bulushev, A. Renken, J. Catal. 219 (2003) 273.
[12] G.D. Pirngruber, M. Luechinger, P.K. Roy, A. Cecchetto, P. Smirniotis, J. Catal. 224 (2004) 429.
[13] E. Berrier, O. Ovsitser, E.V. Kondratenko, M. Schwidder, W. Grünert, A. Brückner, J. Catal. 249 (2007) 67.
[14] F. Kapteijn, G. Marban, J. Rodríguez-Mirasol and J.A. Moulijn, J. Catal. 167 (1997) 256.
[15] C.M. Fu, V.N. Korchak, W.K. Hall, J. Catal. 68 (1981) 166.
[16] G.D. Pirngruber, J. Catal. 219 (2003) 456.
[17] B.R. Wood, J.A. Reimer, A.T. Bell, M.T. Janicke, K.C. Ott, J. Catal. 224 (2004) 148.
[18] E.V. Kondratenko, J. Pérez-Ramírez, Appl. Catal. A 267 (2004) 181.
[19] A. Ates, A. Reitzmann, J. Catal. 235 (2005) 164.
[20] A. Heyden, A.T. Bell, F.J. Keil, J. Catal. 233 (2005) 26.
[21] A. Heyden, F.J. Keil, B. Peters, A.T. Bell, J. Phys. Chem. B 109 (2005) 1857.
[22] N. Hansen, A. Heyden, A.T. Bell, F.J. Keil, J. Catal. 248 (2007) 213.
[23] E.V. Kondratenko, J. Pérez-Ramírez, J. Phys. Chem. B 110 (2006) 22586.
[24] E.V. Kondratenko, J. Pérez-Ramírez, Catal. Today 121 (2007) 197.
[25] E.V. Kondratenko, V.A. Kondratenko, M. Santiago, J. Pérez-Ramírez, J. Catal. 256 (2008) 248.
[26] P. Granger, P. Esteves, S. Kieger, L. Navascues, G. Leclercq, Appl. Catal. B 62 (2006) 236.
[27] S. Alini, F. Basile, S. Blasioli, C. Rinaldi, A. Vaccari, Appl. Catal. B 70 (2007) 323.
[28] J. Pérez-Ramírez, M. Santiago, Chem. Commun. (2007) 619.
[29] M. Santiago, J. Pérez-Ramírez, Environ. Sci. Technol. 41 (2007) 1704.
[30] M. Ruszak, M. Inger, S. Witkowski, M. Wilk, A. Kotarba, Z. Sojka, Catal. Lett. 128 (2008) 72.
[31] M. Santiago, J.C. Groen, J. Pérez-Ramírez, J. Catal. 257 (2008) 152.
[32] G. Giecko, T. Borowiecki, W. Gac, J. Kruk, Catal. Today 137 (2008) 403.
[33] M. Tian, A. Wang, X. Wang, Y. Zhu, T. Zhang, Appl. Catal. B 92 (2009) 437.
[34] D.V. Ivanov, E.M. Sadovskaya, L.G. Pinaeva, L.A. Isupova, J. Catal. 267 (2009) 5.
[35] M. Santiago, M.S. Yalfani, J. Pérez-Ramírez, J. Mater. Chem. 16 (2006) 2886.
[36] J.T. Gleaves, G.S. Yablonsky, P. Phanawadee, Y. Schuurman, Appl. Catal. A 160 (1997) 55.
[37] J. Pérez-Ramírez, E.V. Kondratenko, Catal. Today 121 (2007) 160.
[38] M. Rothaemel, M. Baerns, Ind. Eng. Chem. Res. 35 (1996) 1556.
[39] M. Soick, D. Wolf, M. Baerns, Chem. Eng. Sci. 55 (2000) 2875.
[40] R. F. Sinkovek, N.K. Madsen, ACM T. Math. Software 1 (1975) 232.
[41] D. Wolf, R. Moros, Chem. Eng. Sci. 52 (1997) 1189.
[42] W.H. Press, B.P. Flannery, S.A. Teukolsky, W.T. Vetterling, Numerical Recipes in FORTRAN,, 2 edn., Cambridge University Press, Cambridge, 1992.
[43] G.E.P. Box, N.R. Draper, Empirical model-building and response surfaces, Wiley & Sons, New York, 1987.

[44] D.M. Bates, D.G. Watts, Nonlinear regression analysis and its application, John Wiley & Sons, New York, 1988.

[45] K. Jíša, J. Nováková, M. Schwarze, A. Vondrová, S. Sklenák, Z. Sobalik, J. Catal. 15 (2009) 198.

[46] G. Centi, A. Galli, B. Montanari, S. Perathoner, A. Vaccari, Catal. Today 35 (1997) 113.

[47] J. Pérez-Ramírez, G. Mul, F. Kapteijn, J.A. Moulijn, J. Catal. 208 (2002) 211.

[48] A.L. Yakovlev, G.M. Zhidomirov, R.A. van Santen, Catal. Lett. 75 (2001) 45.

[49] J.A. Ryder, A.K. Chakraborty, A.T. Bell, J. Catal. 220 (2003) 84.

[50] H.L. Wan, X.P. Zhou, W.Z. Weng, R.Q. Long, Z.S. Chao, W.D. Zhang, M.S. Chen, J.Z. Luo, S.Q. Zhou, Catal. Today 51 (1999) 161.

[51] G. Mestl, H. Knözinger, J.H. Lunsford, Berich. Bunsen Gessel. 97 (1993) 319.

[52] J.H. Lunsford, X.Yang, K. Haller, J. Laane, G. Mestl, H. Knözinger, J. Phys. Chem. 97 (1993) 13810.

[53] J. Pérez-Ramírez, F. Kapteijn, A. Brückner, J. Catal. 218 (2003) 234.

UNIVERSITAT ROVIRA I VIRGILI
HEXAALUIMINATE-TYPE CATALYSTS FOR N2O ABATEMENT
Marta Santiago Redondo
ISBN:978-84-693-8864-8/DL:T.1943-2010

UNIVERSITAT ROVIRA I VIRGILI
HEXAALUIMINATE-TYPE CATALYSTS FOR N2O ABATEMENT
Marta Santiago Redondo
ISBN:978-84-693-8864-8/DL:T.1943-2010

Chapter 7

Summary and Outlook

The work, hexaaluminate-type catalysts for N_2O decomposition, realized in this thesis is summarized. The most important results are highlighted and future work is proposed.

N_2O mitigation is a topic of environmental relevance due to the adverse contribution of this harmful gas to global warming and ozone depletion. For this reason, the interest in development new technologies for N_2O decomposition has emerged during the last decade. Extensive studies have been conducted on catalytic systems and their mechanisms for nitrous oxide abatement, overall actives at low temperatures and in idealistic conditions.

Catalytic systems used in nitrous oxide abatement must provide a proper balance between two essential characteristics, *i.e.* activity and stability, since N_2O emitted in the industrial processes is always accompanied by different gaseous pollutants such as NO, O_2, H_2O and SO_2 which affects the functionality of the catalyst.

Metal-substituted hexaaluminates present remarkable performance for N_2O abatement in high-temperature process due its special structure avoiding the sintering and thermal shock. Besides, the substitution of aluminium by transition metals provides redox sites increasing catalytic activity. A number of metals can be easily incorporated in the structure converting the material to a very versatile catalyst.

In this thesis, several hexaaluminate-type catalysts have been studied in detail and evaluated for N_2O decomposition in simulated industrial sources. Additionally, different synthesis strategies have been successfully explored in order to enhance the catalytic performance. Finally, the mechanism via which N_2O decomposes into N_2 and O_2 over metal-substituted hexaaluminate was investigated and compared with iron-containing zeolites. Similarities and differences between the two systems operating at different temperatures have been highlighted.

Synthesis and studies in situ thermal activation of dawsonites-type compounds

In Chapter 2 Ammonium dawsonite ($NH_4AlCO_3(OH)_2$) and the corresponding metal-substituted systems with other transition metals such as Fe or Mn or La were successfully synthesized by in line precipitation method (ILDP) using the carbonate route. Thermal decomposition of the different precursors was studied by *in situ* techniques providing accurate and real information about the evolution of the species and avoiding possible contaminations or undesirables changes in the phases.

Dawsonite-type, independent of the composition of the material, collapses at 473 K in one-step leading to an amorphous alumina phase. The decomposition occurs within a narrow temperature range with the concomitant release of H_2O, NH_3 and CO_2. The final structure of the oxides achieved, after calcination, is uniquely dependent on the metal combination at the start-point of the synthesis. Pure ammonium-dawsonite and transition metal substituted dawsonite (Fe, Mn) are transformed to α-Al_2O_3 above 1423 K as single phase, while the incorporation of lanthanum during the synthesis leads to hexaaluminate phase (β-Al_2O_3). In all cases, the presence of transition metal cations (Fe, Mn) promotes the appearance of these oxide phases at 50-100 K lower temperatures. Monitoring the evolution during thermal activation of dawsonite-type compounds has been of crucial importance for the proper utilization of the resulting oxide in catalysis.

Metal-substituted hexaaluminates for N_2O decomposition

The screening of several metal-substituted lanthanum hexaaluminates and barium-hexaaluminates (Fe, Mn, Ni), realized in **Chapter 3** for N_20 decomposition, showed transition metal as the most relevant factor for catalytic activity. La and Ba-hexaaluminates substituted by transition metals such as Fe and Mn fulfil the rigorous requirements of activity, selectivity, and stability and can be effectively applied in high-temperature (process-gas) catalytic N_2O decomposition. The tests conducted by simulating conditions at the outlet of the noble metal gauzes in ammonia burners of nitric acid production plants showed that hexaaluminate catalysts can be considered as a promising alternative to the already commercialized systems. First, the chemical stability of hexaaluminates is superior to that of spinel and perovskite-based mixed oxides. Secondly, the cost of the hexaaluminate systems are highly competitive because of inexpensive active phases used (*e.g.*, Fe as compared with Co) within a stabilized alumina matrix, and the relatively simple coprecipitation method applied for catalyst preparation.

Enhancing catalytic activity

Chapter 4 addressed the improvement of catalytic activity of hexaaluminates-type catalysts by means of templating approaches. The introduction of carbon during the synthesis resulted in the improvement of catalytic activity for N_2O decomposition by 4-25 times, depending on the synthesis route and the amount of carbon incorporated. The morphology of the oxide obtained upon carbon removal determines the final properties of the hexaaluminate particles. The growth of small crystallites at the carbon surface in the composite together with the vigorous combustion of the template are the key to achieve smaller particles with enhanced surface area. The confined space synthesis mechanism also contributes to this process but in a lower degree due to the macroporous nature of the carbon used.

A complete characterization of the catalyst revealed that only the increase of the surface area was responsible for the better catalytic performance. A quasi linear relationship between the reaction rate and the improvement of the surface area was observed.

Hexaaluminates in Fluidized-bed combustion

In chapter 5, it was demonstrated that the extrapolation of catalytic systems operative in chemical plants to FBCs is not straightforward due to the distinct conditions. The presence of SO_2 combined with high concentrations of H_2O characteristic of combustion processes is critical to develop stable catalysts. The spinel, perovskite, and hexaaluminate catalysts evaluated in this study proved to be highly stable in the presence of high concentrations of O_2, NO, and H_2O for high temperature (1073-1173 K) processes, *i.e.* nitric acid burners. However, despite having remarkable chemical stability under harsh conditions, the presence of SO_2, inhibited drastically the catalysts. Additionally, it caused a segregation of phases due to the formation of sulphates in the case of $LaCoO_3$ and $BaFeAl_{11}O_{19}$.

Promising results arise from the application of steam-activated FeZSM-5 zeolite. This system is unique since its de-N_2O activity is promoted by components coined as inhibitors and poisons for most catalysts (mainly NO and SO_2). Stable performance was obtained during 30 h on stream test at 773 K. Since this temperature is too high for

eventual installation of the catalyst after the preheater (< 600 K), the location of the iron zeolite catalyst after the cyclone appears suitable attending to the available temperature (800-1100 K).

Mechanistic studies

In Chapter 6, we demonstrated that N_2O could decompose over free iron sites and iron sites with mono- and bi-atomic oxygen species originated from N_2O. The significant difference between $BaFeAl_{11}O_{19}$ and Fe-MFI related to the pathways of O_2 formation. While O_2 formation is the limiting step for Fe-MFI, two parallel reaction pathways of O_2 were determined over $BaFeAl_{11}O_{19}$: i) N_2O interacts with a surface bi-atomic oxygen species (*-O_2) yielding gas-phase O_2 and N_2 and ii) *-O_2 can decompose to gas-phase O_2. The lower N_2O decomposition observed over $BaFeAl_{11}O_{19}$ is attributed to the limited interactions of gas-phase N_2O with iron sites possessing monoatomic and biatomic oxygen. The increment of iron in the structure by substitution of aluminium could provide better catalytic activity.

After demonstrating the bright future of metal-substituted hexaaluminate in this thesis for N_2O decomposition at high temperature, the next challenge would be the extrapolation of the results of this catalytic system to real scale. The process of extrapolation would also include the design of catalyst shape for increased catalyst effectiveness and enhanced reactor performance.

UNIVERSITAT ROVIRA I VIRGILI
HEXAALUIMINATE-TYPE CATALYSTS FOR N2O ABATEMENT
Marta Santiago Redondo
ISBN:978-84-693-8864-8/DL:T.1943-2010

UNIVERSITAT ROVIRA I VIRGILI
HEXAALUIMINATE-TYPE CATALYSTS FOR N2O ABATEMENT
Marta Santiago Redondo
ISBN:978-84-693-8864-8/DL:T.1943-2010

List of Publications

Journals

M. Santiago, F. Stüber, A. Fortuny, A. Fabregat, J. Font, "Modified activated carbons for catalytic wet air oxidation of phenol", Carbon 43 (2005) 2134.

M. Santiago, M.S. Yalfani, J. Pérez-Ramírez, "In line dispersion-precipitation method for the synthesis of metal-substituted dawsonites. Genesis of oxide materials with superior properties", J. Mater. Chem. 16 (2006) 2886.

M.S. Yalfani, **M. Santiago**, J. Pérez-Ramírez, "Dawsonite-type clays to oxide catalysts. *In situ* studies during thermal activation", J. Mater. Chem. 17 (2007) 1222.

J. Pérez-Ramírez, **M. Santiago**, **"**Metal-substituted hexaaluminates for high-temperature N_2O abatement", Chem. Commun. (2007) 619.

M. Santiago, J. Pérez-Ramírez, "Decomposition of N_2O over hexaaluminate catalysts", Environ. Sci. Technol. 41 (2007) 1704.

E.V. Kondratenko, V.A. Kondratenko, **M. Santiago**, J. Pérez-Ramírez, "Mechanistic origin of the different activity of Rh-ZSM-5 and Fe-ZSM-5 in N_2O decomposition", J. Catal. 256 (2008) 248.

M. Santiago, J.C. Groen, J. Pérez-Ramírez, "Carbon-templated hexaaluminates with enhanced surface area and catalytic performance", J. Catal. 257 (2008) 152.

M. Santiago, M.A.G. Hevia, J. Pérez-Ramírez, "Evaluation of catalysts for N_2O abatement in fluidized-bed combustion", Appl. Catal. B 90 (2009) 83.

G. Stoica, **M. Santiago**, P.A. Jacobs, J. Pérez-Ramírez, P.P. Pescarmona, "Epoxidation catalysts derived from aluminium and gallium dawsonites", Appl. Catal. A 71 (2009) 43.

S. Abelló, S. Mitchell, **M. Santiago**, G. Stoica, J. Pérez-Ramírez, "Synthesis of impervious layered double hydroxides by continuous coprecipitation with short contact time", J. Mater. Chem. 20 (2010) 5878.

S. Abelló, M.A.G. Hevia, **M. Santiago**, J. Pérez-Ramírez, "DRIFTS study of the catalytic N_2O reduction by SO_2 on FeZSM-5", Catal. Commun. 11 (2010) 1058.

E. V. Kondratenko, V.A. Kondratenko, **M. Santiago**, J. Pérez-Ramírez, "Mechanism and micro-kinetics of direct N_2O decomposition over $BaFeAl_{11}O_{19}$ hexaaluminate and comparison with Fe-MFI zeolites", Appl. Catal. B 99 (2010) 66.

D. Verboekend, A. Bonilla, R. Caicedo-Realpe, **M. Santiago**, J. Pérez-Ramírez, "Properties and functionalities of hierarchical ferrierite zeolites obtained by sequential post-synthesis treatments", Chem. Mater. 22 (2010) 4679.

ISBN:978-84-693-8864-8/DL:T.1943-2010

Conferences

G. Stoica, M. Santiago, P.A. Jacobs, J. Pérez-Ramírez,P.P. Pescarmona
Poster: Epoxidation catalysts derived from aluminium and gallium dawsonites.
EuropaCatIX - Catalysis for a Sustainable World, Salamanca, Spain 2009.

M. Santiago, J.C. Groen, J. Pérez-Ramírez
Poster: Carbon-Templated Hexaaluminates with Enhanced Catalytic Properties.
5th International Conference on Environmental Catalysis, Belfast, UK 2008.

E.V. Kondratenko, V.A. Kondratenko, M. Santiago, J. Pérez-Ramírez
Oral: Mechanistic origin of the different activity of Rh-ZSM5 and Fe-ZSM-5 in N_2O decomposition.
5th International Conference on Environmental Catalysis, Belfast, UK 2008.

M.Santiago, M.S.Yalfani, J. Pérez-Ramírez
Oral: Synthesis of Hexaaluminates with better performance.
SECAT'07 - Congress of the Spanish Society of Catalysis, Bilbao, Spain 2007.

Patents

J. Pérez-Ramírez, S. Abelló Cros, M. Santiago Redondo, "Preparation of uniform nano-sized solid materials by continuous precipitation",WO 2007147881, 2007.

UNIVERSITAT ROVIRA I VIRGILI
HEXAALUIMINATE-TYPE CATALYSTS FOR N2O ABATEMENT
Marta Santiago Redondo
ISBN:978-84-693-8864-8/DL:T.1943-2010

About the Author

Marta Santiago was born in Barcelona on December 17th, 1977. She graduated from I.B. Manel de Cabanyes High School in Vilanova i la Geltrú. Subsequently, she started her undergraduate studies in the Department of Chemical Engineering at the University of Rovira i Virgili (URV), Tarragona, Spain and received her Bachelor's degree in February 2002. She received her Master's degree in Catalysis from the same university in February 2009. After graduation in February 2002, she worked as a support researcher for Prof. Dr. Azael Fabregat at the same university and collaborated in several projects for the industry. From June 2005 until February 2010, she was employed as laboratory manager in the group of Prof. Dr. Javier Pérez-Ramírez at ICIQ. Since 2006 she combined her laboratory responsibilities with her PhD project, whose main results are included in this book. She accepted a research position in the new laboratory of Prof. Dr. Javier Pérez-Ramírez at ETH Zürich, where she has been working since March 2010.